Doped Cobalt Oxide Catalysts for Aqueous, Electrochemical Oxygen Evolution and Alcohol Oxidation

by

Samuel E. Michaud

A dissertation submitted in partial fulfillment
of the requirements for the degree of
Doctor of Philosophy
(Chemistry)
in the University of Michigan
2022

Doctoral Committee:

Assistant Professor Charles C. L. McCrory, Chair
Professor Bart Bartlett
Assistant Professor Nirala Singh
Associate Professor Paul Zimmerman

Samuel E. Michaud

michauds@umich.edu

ORCID iD: 0000-0002-0807-2194

Acknowledgements

I would first like to acknowledge the help of my advisor Dr. Charles C. L. McCrory for all of his help and assistance over the last 5 years. Your comments and the discussions we have had over the last few years on both my work and the works of others has helped me develop the skills and knowledge to have informed discussions on most electrochemical concepts, but more broadly scientific concepts. Without your tutorship, I would not have developed into the scientist I am today. On a similar note, the help of my doctoral committee has been influential over the years. From the original meeting at my candidacy through all of the meetings along the way, your input and questions have helped to guide my research and understanding.

I would also like to acknowledge the help and assistance of the undergraduate and high school students who I have had the pleasure of working with and tutoring in the lab over the last five years. Al-Taimee "Al" Hassan and Rounaq Khan were great additions to the doped metal oxide projects for their respective summers in the lab as DRISE students and were immensely helpful in making a large variety of metal oxide materials. Mike, you were one of the best undergraduates I could have had to help me for the three years you were a member of the lab. Your ability to take on new projects and develop your own ideas was great to watch and having you to bounce ideas off was critical at a time where I was trying to find my own research direction. Michaela, your work was immensely helpful on the alcohol oxidation project. Your questions were key in helping me further my understanding of alcohol oxidation in general, but more specifically what I believe occurs in our specific system.

The rest of the lab members have been critical in both keeping me engaged in my research, as well as keeping me positive at times when things might have ben going poorly. Specifically, I would like to acknowledge Dr. John Lin for his assistance in both getting the OER project running in the lab, as well as his tutorship on electrochemistry and lab work in general. I would also like to specifically acknowledge the rest of my class in the McCrory lab Will Dean and Robert Bonsall for being there from the start and always having good discussions. Lastly I would like to acknowledge Weixuan Nie for always being open to discussion on current experiments in the lab. I like to think your questions on a daily basis was critical in helping my projects progress.

I would also like to acknowledge the friends who have supported me through the last few years. Brian, your continued friendship from our days at UMass and the trips to Chicago were always enjoyable and our discussions along they way greatly helped me over the years. Ted, living with you was great for the four years we lived together. Despite not seeing each other during the week we still had great talks on the weekends watching sports or on the golf course. On that note the friends who I golfed with and watched football with on the weekends were a key support group over the years. Justin, Jessi, Emily, and Matt, you were always great to talk to either about the event going on at the time, or about events in our daily or working lives.

I also need to acknowledge all of the support that I have received from Taylor over the years. Her help both in the lab and her support outside of the lab was at times the only thing that seemed to keep me going. Through the easy times and hard times I could always look to you for anything when needed. The support is something that I would not have exchanged for anything and I hope that the feelings were reciprocated.

And lastly I would like to acknowledge my family for all of the support from the beginning. I wouldn’t be the person I am today with out all of your help and support over the last 28 years. The support in all manners over the last 5 years in particular has kept me going through the difficult times that arose in my grad school career

Table of Contents

List of Figures

List of Tables

Abstract

As global energy production transitions to more renewable yet intermittent sources such as solar and wind, long term storage of this energy is a critical challenge that needs to be overcome. Hydrogen gas produced through electrochemical water splitting is one promising method for energy storage, however the viability generating large quantities of hydrogen gas is limited by the sluggish kinetics at the anode making improving the anodic activity vital in the advancement of renewable hydrogen production.

Cobalt based materials show promise as active catalysts for anodic reactions under alkaline conditions. Spinel Co_3O_4 is one such cobalt material that is both active and stable for elongated times for the oxygen evolution reaction (OER). The defined crystalline system of this catalyst makes it an ideal candidate for systematic material alteration, where bulk replacement of atoms in the cobalt oxide lattice with transition metals allows for activity trends to be developed across a range dopant level giving insight into how these metals alter anodic activity. By systematically performing these alterations we can further the understanding of how different dopant ions affect OER activity and additionally understand what makes an active OER catalyst.

In Chapter 1, I discuss the literature on transition metal based OER catalyst with a focus on the factors which affect catalytic activity in these systems. I then discuss how transition metal doping is used previously in the literature to improve upon the OER activity of cobalt oxide based materials. The remainder of the chapter discusses how by transitioning away from the OER at the anode to alcohol oxidation, the overall anodic reactivity can be increased.

In Chapter 2 I discuss the doping of various transition metals alters the activity for the OER, with a specific focus on the activity trends observed in iron doped $Co_{3-x}Fe_xO_4$ materials, highlighting a $Co_{2.75}Fe_{0.25}O_4$ catalyst which operates at 360±1 mV overpotential however further iron doping is shown to decrease OER activity with $CoFe_2O_4$ operating at 460±1 mV overpotential, suggesting a highly complex relationship between Fe content and electrochemical activity, which goes against our previously published hypothesis.

In Chapter 3 I discuss a CoV_2O_4 catalyst for the OER which shows remarkable OER activity, with a BET normalized activity of 368±73 $\mu A/cm^2$, 300 times higher than Co_3O_4. However, through postmortem material analysis the activity is found to not be due to vanadium ions but rather due to the formation of a vanadium free cobalt oxide material. This study highlights the critical importance of post-mortem material analysis in electrocatalytic measurements.

In Chapter 4 I discuss how a Co_2NiO_4 catalyst can be used to increase the anodic activity by oxidizing an alcohol substrate rather than water operating at 94±4 mA/cm^2 current density. Additionally, I report how through changing the alcohol and the applied potential at the electrode, the proportion of carboxylic acid and aldehyde products is changed, with carboxylic acid charge efficiency increasing with increased alcohol size, and decreasing with increased applied potential.

In Chapter 5 I highlight the major conclusions of my work, and the directions I believe the projects discussed in this Thesis should take.

This dissertation highlights how transition metal doping can increase anodic activity and highlights the critical importance of in-depth systematic studies for improving catalyst systems. The work also highlights key activity trends in anodic activity and selectivity in the OER and AOR systems

Chapter 1 Introduction

1.1 Preface

This chapter presents an overview of the literature on anodic reactions for the electrochemical production of hydrogen. Specifically, the chapter focuses on transition metal catalysts for the oxygen evolution reaction, highlighting the aspects within transition metal oxide oxygen evolution catalysts that limit their activity in the oxygen evolution reaction. Additionally, I discuss transition metal doping as a method for improving catalytic activity with a focus on cobalt oxide based materials looking at dopant ions alter OER activity. The chapter concludes by highlighting the recent work with transition metal oxide materials for alcohol oxidation, which is a viable alternative reaction to oxygen evolution, showing higher current densities at less positive potentials.

1.2 Electrochemical Oxygen Evolution Reaction (OER)

As the transition away from carbon-based fuel sources continues and reliance on intermittent forms of energy production such as solar or wind energy increases in the coming decade, the ability to store this energy for later use is of critical importance.[1-3] Storage of excess intermittent energy in the form of chemical bonds which can later be converted back into electrical energy as required is one of many viable solutions to this energy storage problem.[4, 5] The formation of hydrogen gas through the electrochemical reduction of protons through water splitting one highly researched method of energy storage[6-8] however, these systems have difficulty achieving

high current densities due to sluggish kinetics at the anode, limiting the viability for large-scale implementation of electrochemically generated hydrogen production. [7, 9]

The oxidation of water in the oxygen evolution reaction (OER), typically requires large overpotentials to achieve meaningful current densities due to the nature of the four electron reaction limiting the ability for electrocatalytic water splitting systems to achieve high current densities at moderate applied potentials, making discovery of improved OER catalysts key in the development of advanced electrocatalytic water splitting systems.[7, 9] Most active and stable systems for the OER require the use of alkaline conditions due to the instability of most metal oxide systems in low pH environments. Alternatively, under alkaline conditions there are a significant number of metal oxide systems that show long term stability, making alkaline water electrolysis systems viable systems to study for furthering the understanding of OER materials. As such most of the fundamental research over the last decade on OER materials has focused on OER catalysts which operate in alkaline conditions.

Recently a push towards development of transition metal based catalysts has developed as a means to move away from current state-of-the art materials which are typically constructed with precious metal such as iridium or ruthenium[10-14] which have far less elemental abundance than common transition metals and as such are more expensive.[15] Of these transition metal catalyst cobalt[16-19], iron,[20, 21] and nickel[22] based materials are among the most commonly studied materials with various other systems also showing promise as active and stable anodic materials.[23-25] Cobalt based materials have been particularly interesting due to the high intrinsic activity of cobalt oxide in various forms including layered double hydroxides (LDH)[26-28], amorphous electrodeposited phases[16, 29, 30], and crystalline phases,[31-33] showing how versatile cobalt based materials are for the OER.[31, 33] Additionally, work on these types of materials has shown that incorporating a range of

transition metals into the cobalt oxide system through metal doping the activity for the OER can be improved.[16, 18, 31, 34, 35] However, in most of the OER literature, the lack of comprehensive, systematic studies hinders the ability to correlate the changes observed in these material alterations with the fundamental principle responsible for changing the OER activity. By first understanding how different systems operate in the OER we can develop strategies to create new and improved catalysts for the OER.

1.3 Transition Metal Based OER Catalysts

Transition metal based electrocatalytic materials for the OER have been studied as an alternative to the modern state of the art catalyst OER catalysts which use expensive noble metals such as iridium and ruthenium.[7, 9, 32] The state of the art materials typically operate in the 380 mV overpotential range at 10 mA/cm^2, and show high stability under oxidative conditions, maintaining their catalytic activity over elongated periods of time while held at a constant applied potential.[10, 13, 32] Of the transition metal based materials studied as replacements the most common systems are based on Mn,[23-25, 36-38] Fe[20, 21], Ni[22, 39-42], or Co[16-19] with each system showing a range of activity and selectivity. Figure 1.1 shows the activity of benchmarked OER materials. The overpotential required to reach 10mA/cm^2 current density is reported both before and after 2hr stability tests to highlight stable materials. In this plot the metal oxide systems mentioned previously show good activity and stability, falling along the central line. More importantly, the figure also highlights activity gaps between the simple transition metal oxides and more state of the art materials which are complex oxide materials or noble metal based oxide materials.[7] By better understanding the underlying reasons for the activities and stabilities in these transition metal catalyst, this knowledge can be leveraged into the development of new, advanced OER catalytic materials.

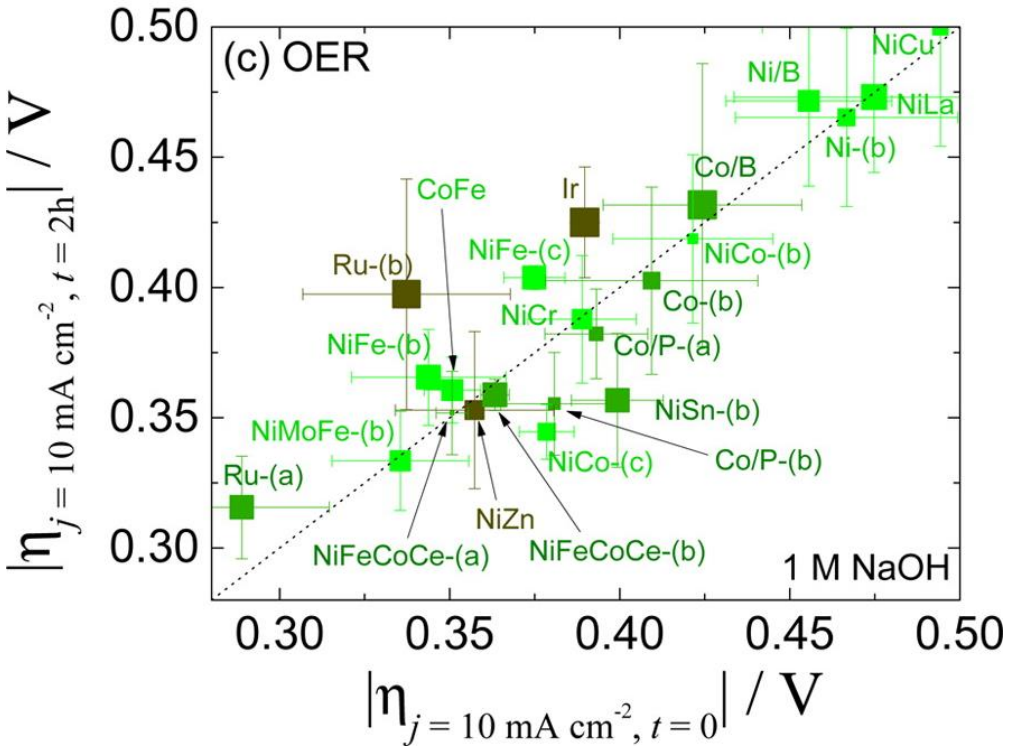

Figure 1.1 Graph of overpotential at time = 0 (x axis) and time = 2hr (y axis) for a range of electrodeposited metal oxide systems showing the activity gap between state of the art ruthenium catalysts and most other undoped oxide materials. Reprinted with permission from Charles C. L. McCrory, Suho Jung, Ivonne M. Ferrer, et al., *J. Am. Chem. Soc.* 2015. Copyright 2015 American Chemical Society.

Iron oxides have been reported as active catalyst for the OER under alkaline conditions and are of great interest due to their high photoabsorption, making these catalysts possible photoanodes for oxygen production in the photocatalytic water splitting reaction.[21, 43-45] Although these catalysts are not among the most active for the OER, achieving 10mA/cm^2 current densities at overpotentials larger than 400mV, fundamental understanding into how iron oxides operate and the aspects that affect the activity of these systems is critical in the understanding of transition metal OER catalysts. In 2013 Lyons and Doyle proposed a mechanism for the OER on Fe_2O_3 through both electrochemical impedance spectroscopy (EIS) studies and Tafel analysis.[21] Their report suggests a facile first oxidation of the Fe center which allows for the formation of surface hydroxide anions. This is followed by a kinetically sluggish oxidation to form an iron oxo species. This oxo species is then easily oxidized to form a superoxo and peroxo species before eliminating an oxygen molecule through nucleophilic substitution by hydroxide anion. The proposed mechanism uses one surface Fe site to perform the catalytic transformation. It should be noted that the mechanism proposed does suggest formation of a formal Fe(V) which has not been observed spectroscopically to date.[21] A recent study of Fe_2O_3 for OER showed an activity dependence on the exposed facet, suggesting that the (001) facet to be the most active of the three facets studied.[44] This is hypothesized to be due to more facile formation of Fe^{IV}=O on the (001) facet than other exposed facets.[44] Note that this report suggests the formation of a formal Fe (IV)=O and not a formal Fe(V)=O as suggested by Doyle, however the rate determining step in both studies is still the same.[21] Density functional theory (DFT) calculations for FeOx systems suggest similarly to the experimental studies, that the oxidation forming the surface Fe-O* is kinetically slow, with a calculated overpotential of 1.33V limiting the activity for the OER.[20] In 2015 Boettcher et.al. investigated electrodeposited metal oxide films and found through measuring conductivity under

applied potentials (Figure 1.2), that FeOOH films are highly insulating at potentials negative of 400mV overvoltage, and maintained a low conductivity even as the potential was increased 100mV more positive. This low conductivity is suggested to be a major reason for the low activity of iron oxide films.[29] Interestingly the OER activity of this system is shown to mimic closely the effective conductivity of the material as shown in Figure 1.2, suggesting a strong correlation between conductivity and OER activity within this system.[29] In 2013, Berlinguette et al. studied the Hematite system (Fe_2O_3) looking at the effects of crystallinity on OER activity, showing amorphous phased material drastically improves the OER activity relative to the crystalline phased materials.[41] This is similar to other studies where amorphous phased systems showed increased activity with this increased activity being attributed to increased exposed surface active sites in the amorphous materials.[33] Additionally, FeOx electrodes show limited stability under OER conditions, making them less ideal for large scale applications.[7, 9] Key observations made using iron oxide catalysts suggest that improvements in OER materials should focus on improving conductivity, as well as fundamentally understanding the mechanism at the electrode surface. The former allows for increase electron transport from the electrode material to the surface, while the latter facilitates an understanding of processes that occur at the electrode surface and how the material itself can alter the catalytic process. Both events are critical when considering methods to improve the activity of OER materials and are clearly represented in the FeOx OER literature.

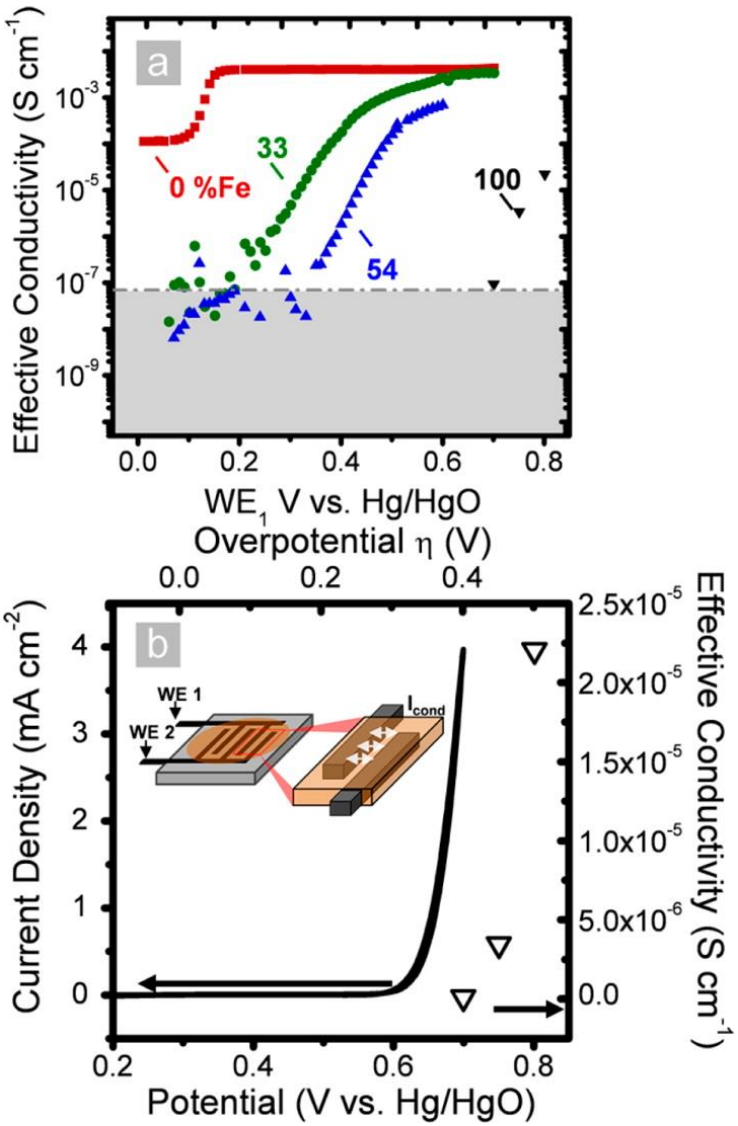

Figure 1.2 Shows the effective conductivity (a) of electrodeposited films as a function of applied potential, showing Fe inhibits electron conductivity in CoOOH films with 100% FeOOH films being electronically insulating. This effective conductivity is plotted vs the voltametric response (b) showing activity tracks the effective conductivity in FeOOH films. This figure is reprinted with permission from Michaela S. Burke, Matthew G. Kast, Lena Trotuchaud, Adam M. Smith, and Shannon W. Boettcher, *J. Am. Chem. Soc*. 2015. Copyright 2015 American Chemical Society. Further permission related to this figure should be directed to the American Chemical Society.

Nickel oxide systems are one of the most studied and active systems for the OER, showing increased activity and stability when compared to FeOx systems.[7, 29, 43, 46] Similar to iron oxide systems, nickel based systems have been shown to be plagued by poor intrinsic conductivities. Interestingly, the conductivities in nickel oxides are also dependent on the crystalline phase that the nickel oxide takes. Yan et al. showed in 2014 that the α-$Ni(OH)_2$ phase is more active for OER than the β-$Ni(OH)_2$ phase. This was found to be due to a rearrangement under applied potentials making where the α-$Ni(OH)_2$ transforms into a γ-Ni(OH) phase allowing for more facile electron transport, and is not due to increased conductivity within the α-Ni(OH) phase.[46] This restructuring has also been noted in various other reports of Ni based oxide materials under oxidative conditions.[47, 48] Recent accounts of nickel oxide electrodes have attempted to increase the effective conductivity of the system, by shifting the Ni^{2+}/Ni^{3+} redox couple to less positive potentials due to the conductivity increase observed in more oxidized states.[22, 49-51] For example, Song, et al. suggested that the formation of nickel vacancies in an α-$Ni(OH)_2$ results in an increased OER activity, finding that the increase in conductivity of the catalyst is the cause of the increased OER activity.[22] In a similar system, Chen and co-workers were able to create an α-$Ni(OH)_2$ system with close proximity Ag which also showed increased activity, this increase was also attributed to an increase in conductivity, however in this system the increased conductivity was attributed to an increase in high valent Ni^{3+}/Ni^{4+} due to the presence of silver atoms.[50] Our understanding of the NiOx system for the OER is critical in advancing our overall knowledge of catalysts for the OER. Similar to what is observed in the FeOx literature, factors such as crystallinity, but seemingly more important, crystal structure, are shown to alter the OER activity, while additional factors such as conductivity continue to limit the catalytic activity of single metal oxide materials.

Cobalt based OER materials have been studied since the 1960s, but saw a renaissance after Nocera and coworkers drastically expanded on the work done 40 years prior by discerning fundamental aspects of the catalytic system.[52-56] Since then, a large number of studies on cobalt-based oxide materials have been performed, highlighting the activity and stability of these systems.[56-58] However even the most active of these systems only operate at 300 mV overpotential at 10 mA/cm^2 . Similar to the other metal oxide materials discussed, cobalt based oxides suffer from electrical conductivity issues limiting overall catalytic activity.[59-61] Various methods to improve the catalytic activity of cobalt oxides have been studies, with the common strategy centering around the incorporation of a conductive substrate on which cobalt oxide particles are deposited on in an attempt to increase the overall system conductivity.[59] Additional strategies include nitrogen doping within both the substrate[62] and the active material itself,[63] which have also shown increased catalytic activity due to conductivity improvements.[60] Continued research into conductivity improvements offers the ability to increase overall electron transport within the system. That said, many other methods to increase activity are being studied. One of these methods centers around gaining a deeper understanding of how these materials interact with water at the electrode surface.

Determination of the active site for the OER on CoOx materials is critical in the fundamental understanding of how these systems perform in the OER. Most reports suggest that Co^{3+} sites are more active for OER than Co^{2+} sites, with evidence coming from both computational[64] and experimental sources.[65, 66] Both of these methods also suggest that there is a facet dependence on the catalytic activity on cobalt materials, further highlighting the difference between the Co^{2+} and Co^{3+} sites. A recent study calculating the valance state energies of a CoOx catalyst found through DFT calculations that the covalency of the Co-O surface bond suggests a

far more favorable formation of oxidized surface oxygen species in Co^{3+}, the trends predicted through DFT were supported with x-ray absorption spectroscopy (XAS) which suggested a bulk valance state change in the Co atoms from Co^{3+} to $Co^{3.4+}$ under OER conditions.[67] It should be noted that for the Co^{2+} active sites, the studies also suggested an increase in oxygen vacancies occurs, which also can impart geometric changes in the material, impacting surface area and possibly increased OER activity.[68, 69]

From a mechanistic standpoint, Frei and co-workers used time resolved spectroscopy to probe the photocatalytic mechanism for the OER on cobalt oxide materials, a pioneering study in understanding the mechanism for the OER on Co_3O_4. The proposed mechanism is shown in Figure 1.3 and suggests two possible pathways that exist for oxygen production on these surfaces. One is the kinetically faster, two site pathway and the sluggish single site mechanism. The dual Co center mechanism begins with two formal oxidations of the resting Co(III) to Co(IV) followed by the nucleophilic attack by a water molecule into one of the Co(IV) centers forming a O-O bond and a hydroperoxide species. The removal of an electron from the hydroperoxide then forms a bridged superoxide species. The finals step before the catalytic cycle is repeated is the 4^{th} electron equivalent is removed concurrent with the nucleophilic attack by a second water molecule, liberating the bridged superoxo species and regenerating the surface oxyhydroxide.[19] In 2015 Strasser and co workers also looked at Co_3O_4 from a mechanistic perspective and discovered that there likely is a reversible surface amorphization process that occurs partially due to the oxidation of Co^{2+} in the lattice to $Co^{3+/4+}$ under OER potentials.[70] This effect is likely due to the stability of Co^{3+} in T_d holes. As such when oxidized the ions must migrate to vacant O_h sites in the lattice creating an amorphous shell on the catalyst surface that is then returned back to the crystalline phase as the potential moves back to open circuit and the ions are allowed to rest in the Co^{3+} state.[70]

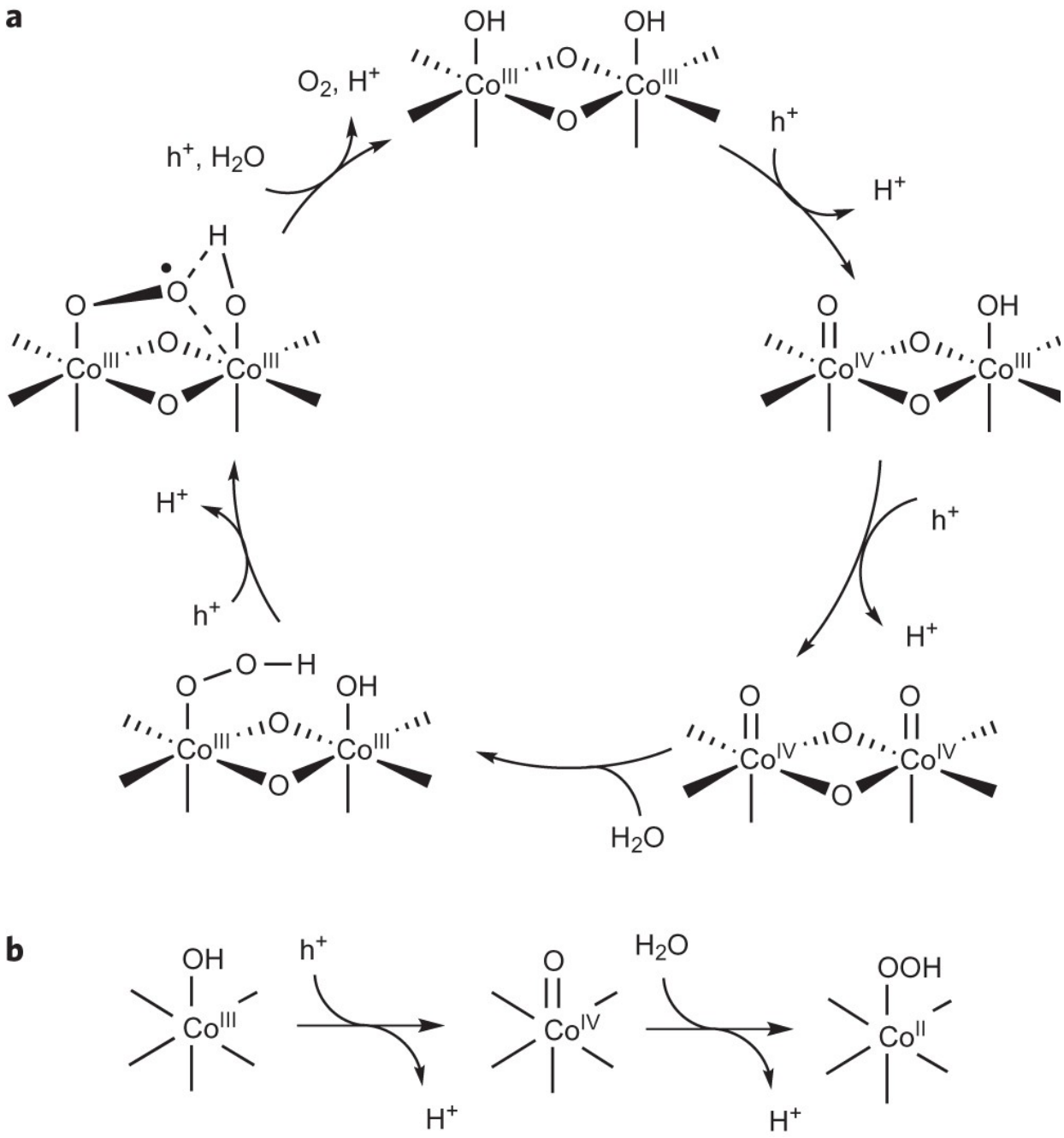

Figure 1.3 The proposed mechanism for water oxidation on Cobalt Oxide materials as observed by Frei and co workers through pump probe spectroscopy (a) shows the proposed two site mechanism where (b) shows the observed single site mechanistic pathway. This figure is reprinted with permission from Miao Zhang, et al., *Nature Chemistry* 2015. Copyright Nature Publishing Group 2014

From a mechanistic standpoint, the oxidation of water with cobalt based oxide materials should be able to be altered through transition metal dopants in a few different ways. The first is through shifting the oxidation potential of the $Co^{3+/4+}$ redox couple, similar to what is observed in the Ni system upon addition of Ag atoms. The other method is through altering the stability of the different mechanistic pathways, allowing for more favorable intermediate formation, and more facile elimination of the products. In addition to these mechanistic aspects, improving upon aspects that hinder activity in various other metal oxide systems will increase OER activity, such as conductivity. In the next section, I will further this discussion by looking at how transition metal doping has improved OER activities and studies suggesting pathways forward in development of novel Co based OER catalysts.

1.4 Transition Metal Doping in OER Catalysts

State of the art catalysts for the OER consist mainly of Ru or Ir based oxide materials which operate at low overpotentials, with high catalytic integrity during long term electrolysis.[7, 9, 12, 13, 32] These systems have been shown to have the activity improved upon metal doping where small quantities of metal dopant ions allow the system to achieve higher activities with increased stability. For example, the Kertil group discovered that by incorporating cobalt into a RuO_2 lattice forming a $Ru_{0.8}Co_{0.2}O_{2-\delta}$ lattice, there is an increase in activity, as well as a change in the rate limiting step for the catalytic production of oxygen.[12] More recently, the Hwang group in 2018 showed that transition metal doping altered the OER activity of IrO_2. Specifically the addition of Mn and Cr was shown to increase the OER activity by 30-35mV where Fe, Ni, and Co doping showed negligible, or even decreased, OER improvements, suggesting different metals can have drastically different effects on the OER activity for a catalytic species.[71] Although these studies have shown improvements in OER activity upon transition metal doping, the continued use of Ru

and Ir makes them less applicable to large scale applications if full transition metal based systems can be developed.

Transition metal doping of cobalt oxide materials has also been heavily investigated over the last decade, as doping has shown to be a viable method of improving upon the intrinsic activity of the parent cobalt oxide material.[72-74] Some of the most common dopant ions observed for CoOx species are nickel[6, 39, 75, 76] and iron ions,[16, 28, 77] however other metals have also been observed to increase OER activity in the literature.[27, 72, 78] An early study on doped amorphous cobalt, nickel, and iron, trimetallic systems by Berlinguette and coworkers showed multiple trends as nickel and iron dopant levels were increased.[41] The first trend was that, although FeOx itself was not able to catalyze the OER in the potential range tested, the presence of Fe atoms as dopant ions in bulk CoOx and NiOx greatly increased the OER activity.[41] The other key finding was that although active individually for the OER, $Co_{1-x}Ni_xOx$ samples without Fe were less active than the parent materials suggesting that simply combining electro active species together does not necessarily result in a more electroactive material. Rather, this suggests there is a complex relationship between intrinsic activity of the base material and the intrinsic activity of the dopant matieral.[41] Additionally, this report suggests that Fe is a critical dopant species for increased catalyst performance despite the relatively inactive for the OER observed in pure FeOx.

The role of Fe was further investigated by the Boettcher group. In their first studies on this system, looking specifically at Fe in CoOx amorphous films, they showed an increase in activity with increasing Fe content which suggests a strong correlation between dopant concentration and OER activity.[16] Importantly the interplay between the metals is noted by a transparent shift in the $Co^{3+/4+}$ redox couple in the system suggesting strong electronic interplay between the two metal species in the material.[16] They also showed that even low levels of Fe in solution can affect the

catalytic activity of CoOx samples for the OER, this result was confirmed in a later publication where the group specifically looked at the effects that solution phase Fe atoms in solution had on OER activity.[34] They were able to show a quantifiable increase in activity due to solution phase Fe that is not observed when purified electrolyte is used, suggesting that under electrochemical bias trace Fe ions interact with the electrode surface, forming an active CoFe species. The data also suggests that even trace Fe in solution can alter the turnover frequency (TOF) of CoOOH films, with rigorously cleaned electrolytes showing a TOF_{mass} (mass normalized TOF) of $0.007\ s^{-1}$ where using uncleaned electrolyte produced a TOF_{mass} of $0.026\ s^{-1}$. This is attributed to low levels of Fe adhering to the electrode surface even though no Fe was detected on the electrode in the latter sample via x-ray photoelectron spectroscopy (XPS).[16] This is similar to other systems where trace metal contamination either altered the electrode activity or changes the product selectivity during bulk electrolysis measurments.[79] These results show the promise of Fe doped CoOx materials as active OER catalysts.

Vanadium dopants have been suggested as a possible dopant ion in CoOx samples to increase OER activity. One study on vanadium dopants looked specifically at V doping into spinel Co_3O_4 and showed that V incorporation increased the activity of the Co_3O_4 drastically This effect was attributed to surface lattice distortion and increased charge transfer within the catalyst as suggested by the DFT calculations performed as a part of the study.[80] A study on a similar material showed an increase in OER activity with vanadium incorporation in CoOOH samples. The authors suggest this result is due to altered stability of surface intermediates as well as increased charge transfer due to the incorporated V ions in the system.[78] A third study created CoVOx nanoneedles on a nickel foam electrode and observed vanadium increased the activity of their nanoneedles. Similar to other studies this was attributed to increased charge transport due to an altered electronic

structure as V is added.[18] All three of these studies suggest that vanadium plays a large role in the activity of cobalt oxide materials and is a promising target when looking for metal dopants to increase OER activity. It should be noted that few of these studies show any type of post electrocatalytic material measurements which brings into question the material stability under the applied potentials, even though the electrochemical data suggests a stable active catalytic species.

Nickel dopants have been shown to increase the activity of Co based OER catalysts. The reason for this activity increase is typically attributed to an increase in electron transfer within the material due changes in the conductivity upon the addition of Ni atoms.[81-84] These conductivity effects have also been attributed to oxygen defects found in Ni doped systems[82] as well as the direct interactions of neighboring Co^{3+} and Ni^{2+} atoms.[84] Ni incorporation into Co_3O_4 has also been suggested to alter the valance bands of the material allowing for an increased interaction with surface adsorbed oxygen intermediates.[85] Specifically, the increase in Ni concentration in the lattice widens the band gap of the material, lessening the energy penalty with oxygen binding as the orbital overlap is increased.[85] This effect, coupled with the decreased charge transfer evident by the decreased calculated band gap , from 1.19 eV in Co_3O_4 to 0.39 eV in $NiCo_2O_4$ is the rationale behind this increased activity.

A key study on doped Co_3O_4 was reported by McCrory and coworkers, in which Cr was systematically doped into $Co_{3-x}Cr_xO_4$ over a large range of dopant levels.[31] In this system, interesting activity trends were observed as Cr levels increased in the crystalline system and can be seen in figure 1.4. Initially, as the dopant level increased there was an increase in activity up to 33% Cr doping level followed by a plateauing in activity between the 33% and 50% level. After 50% Cr doping the activity decreased as more Cr was incorporated into the lattice. This trend was more pronounced when the samples were normalized for the Brunauer-Emmett-Teller surface area

(BET), which is used to account for the electroactive surface area.[32] Mechanistically one could look at the trend presented and the OER mechanism proposed by Frei and coworkers shown in figure 1.3 and draw conclusions in how the dopant ion affects the OER activity. The first conclusion is that the electron deficient Cr ions in the lattice make the surface Co atoms more susceptible to nucleophilic attack by the solution phase hydroxyl species, thus increasing the overall reaction rate. This is observed in the first phase of the Cr dopant trend where OER activity is increasing. The second aspect is the size of Cr ions altering the lattice spacing which changes the stability of the bridged μ-hydroxo species. This effect would likely be observed throughout the trend as the altered lattice parameter may serve to, at first increase the stability of the bridged intermediate, and then as the lattice spacing continues to increase, destabilize, and shut down the bridged intermediate. It should be noted there also is a likely conductivity change under OER conditions as is seen in other similar systems. However, this measurement was not collected in this study rather conductivities were collected under no applied external potential due to the experimental difficulties associated with applying a potential concurrently to measuring conductivities in nanoparticle systems. The results of this study were key in formulating the hypothesis for the studies discussed in the second and third chapter herein.

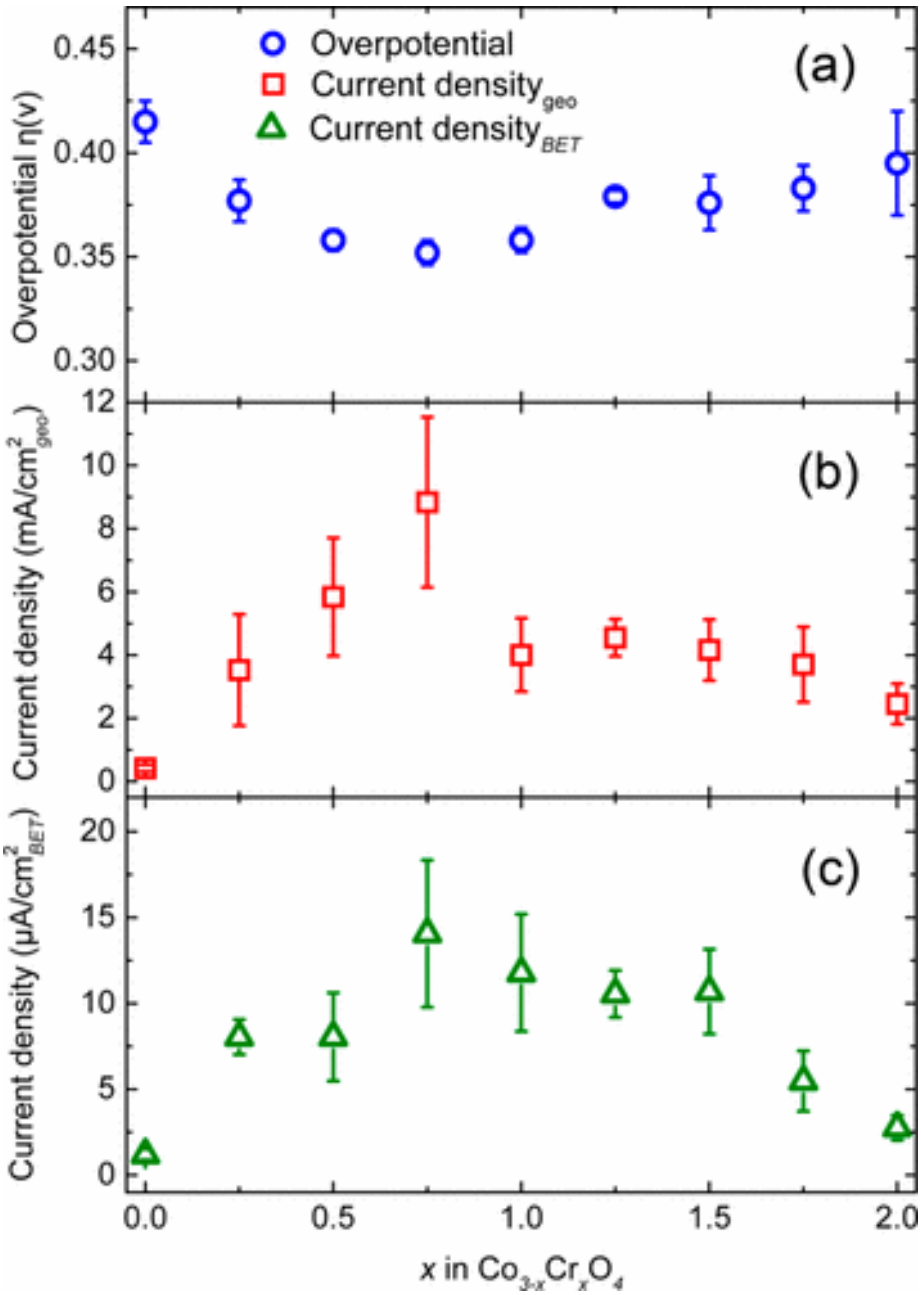

Figure 1.4 Activity trends observed in $Co_{3-x}Cr_xO_4$ catalysts as a function of Cr doping amount. The trends in overpotential (a), current density per geometric surface area (b), and current density per BET normalized surface are (c), suggest Cr ions have the ability to increase OER activity. This figure is reprinted with permission from Chia-Cheng Lin, Charles C. L. McCrory, *ACS Catal.* 2017. Copyright American Chemical Society 2017.

1.5 Alcohol Oxidation as an Alternative Anodic Reaction

More recently, a shift in perspective has seen alternative reactions being studied as a replacement for oxygen evolution at the anode. These systems allow the anode to achieve higher current densities at less positive potentials, increasing the relative efficiency of the system. [86-89] Of these reactions, the oxidation of organic alcohols through the alcohol oxidation reaction (AOR) has shown particular promise, not only due to the ability to drastically decrease the thermodynamic potential of the anodic, but also to increase the value of the electrolysis product produced making the total economic value of hydrogen production more profitable.[86, 89] Active catalysts for these transformation include a wide range of materials ranging from noble metal based systems[90, 91] to more simple metal oxide materials.[88, 92] Most of these systems also happen to show activity for the OER which suggests the possibility that trends and observations present in the OER literature can be translated into the AOR system.[93, 94]

Of these alcohols studied for this reaction short chain alcohols such as methanol and ethanol have developed considerable attention as both are more thermodynamically favorable to be oxidized compared to water under alkaline conditions.[95, 96] Using methanol as an example, the thermodynamic potential for the four electron oxidation to formic acid is 0.718V vs RHE, 500mV less positive compared to water oxidation, drastically decreasing the chemical potential required at the anode. This opens the possibility of creating complete systems that operate at much higher current densities using the same applied voltages at across the electrocatalytic system.[90, 97] Multiple studies have shown that Pt based materials oxidize methanol at 800mV vs RHE in alkaline conditions, roughly 600mV less positive than the most active OER catalysts.[98, 99] Typically these studies report a peak in the cyclic voltammogram that is attributed to the oxidation of methanol. However these studies typically do not report products and assume complete oxidation of the

substrate, with only a few studies performing bulk electrolysis measurements which show continued catalytic activity over prolonged periods to time.[99] Cobalt based materials have also shown activity for methanol oxidation, although the potentials for this reaction are more positive than that observed for Pt.[100-102] These systems also often assume complete oxidation of the alcohol substrate.

In an early study of alcohol oxidation using substrates that branch away from simple short chain alcohols, the Koper group looked into a range of alcohols with similar structures to the glycerol molecule using a gold electrode (Figure 1.5).[103] Their findings suggested that deprotonation, either to the alkoxide or abstracting the H_β governs the reaction rate for alcohol oxidation, shown through a linear dependence on the onset potential for AOR with respect to the alcohol's pKa. They also note a rapid oxidation of the aldehyde to a carboxylic acid similar to previous reports by the same group,[103, 104] however they still suggest the aldehyde is the major product formed directly at the electrode surface.[104] Later studies on glycerol oxidation using Pt surfaces performed by Angelucci et al.[105] also supported the idea that a deprotonation step is required early on in the reaction mechanism, by the presence of the $\nu(C{=}O)_{acyl}$ mode. Solution pH studies also suggest a deprotonation is required on Au surfaces. However, they noted that this step may not be as important on Pt surfaces as no shifts in activity is observed with changes in the pH.[106] Follow up studies on Pt surfaces through both of the research groups suggest that surface binding to specific Pt facets promotes different products being formed in the electrocatalytic oxidation of glycerol.[107] Work by Li et al. in 2012 showed, using gold catalysts supported on carbon nanotubes resulted in a potential dependence in the selectivity of glycerol oxidation, with more positive potentials increasing the conversion to glycolate with a large decrease in the produced oxalate, and tartronate products.[108] Other effects such as KOH concentration and

glycerol concentration played less of a role in determining product distribution than applied potential suggesting the electrode reaction is highly influential over reaction products rather than solution phase reactions.[108] These works highlight key mechanistic aspects of the AOR using more simple surfaces showing the influence of solution pH, reactant pKa, electrode material, surface structure, and applied potential, all which are critical in controlling the selective conversion to specific products in the oxidation of glycerol.

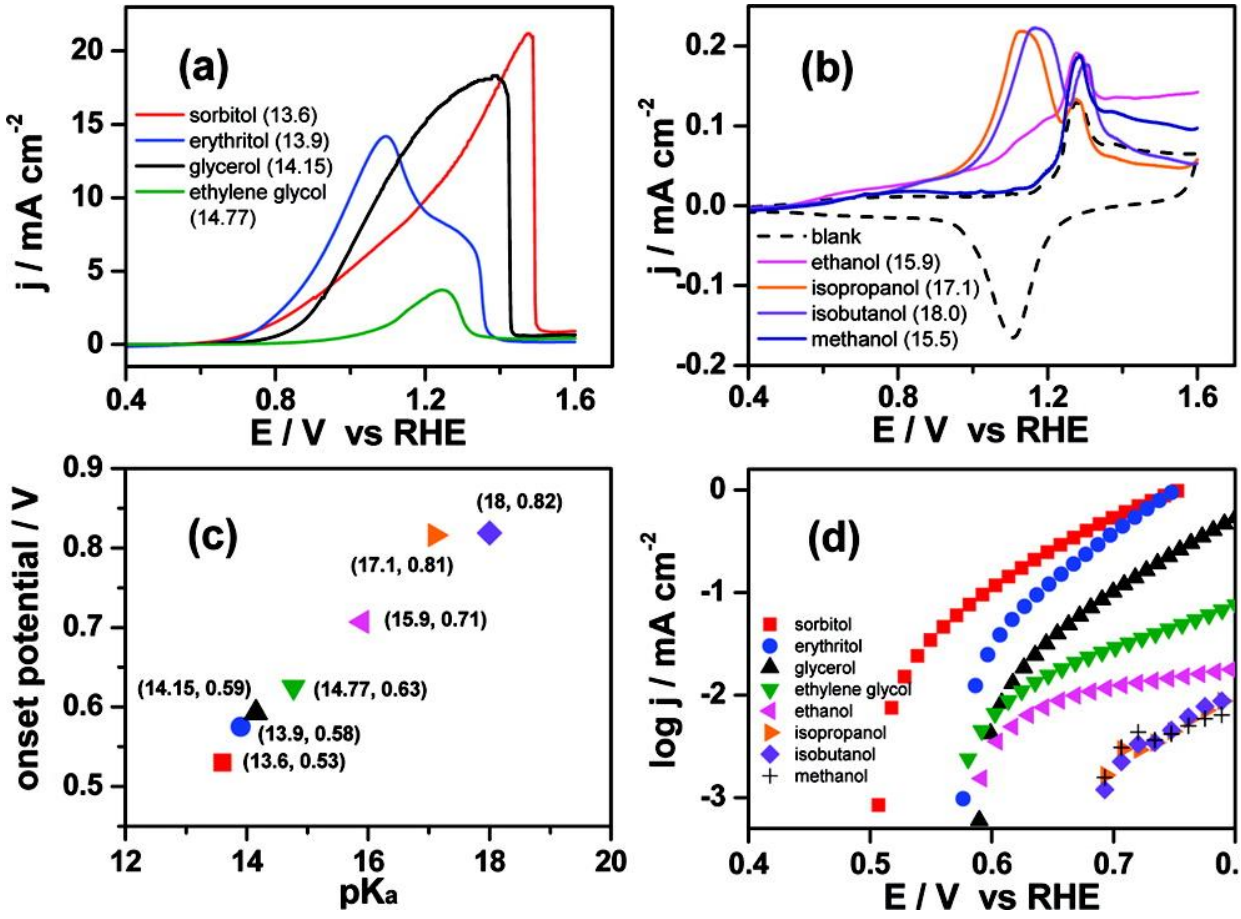

Figure 1.5 a and b: alcohol oxidation curves on Au surface with various alcohols taken in alkaline conditions. c. Onset potential vs pKa of the corresponding alcohol showing a linear relationship between onset potential and pKa and d. Tafel information for the alcohols tested in this study. This figure is reprinted with permission from Youngkook Kwon, Stanley C. S. Li, Paramaconi Rodriguez, et al., *J. Am. Chem. Soc.*, 2011. Copyright American Chemical Society 2011.

Similar to the oxygen evolution reaction, transition metal based catalyst are of interest for the alcohol oxidation reaction due to their low cost and relative abundance. Using a cobalt based oxide, Zheng, et al. performed alkaline electrolysis in a solution with 1M ethanol added and showed an increase in overall activity with respect to the background OER and also reported a high selectivity for ethyl acetate, the $4e^-$ oxidation product of ethanol at 1.445V vs RHE applied potential.[109] This work highlights both the activity that transition metal based catalysts can have for alcohol oxidation as well as the viability for these systems to use lower voltage energy sources to produce hydrogen from aqueous systems. Other studies looking at Co_3O_4 for alcohol oxidation showed activity for aromatic alcohols such as benzyl alcohol have a product selectivity greater than 92% for benzoic acid.[110] This selectivity was also observed to occur in other studies using a Co_3O_4 catalysts on nickel foam. Nickel foam was used to increase overall activity by increasing electrode surface area.[111] The Xu group looked at various C3 alcohols and measured the alcohol oxidation activity using a Co_3O_4 catalysts on graphite paper.[112] Their findings show activity increases with increasing alcohol functional groups and they also showed C-C bond cleavage in systems containing adjacent alcohol functional groups attributed to the adjacent alcohol making bond cleavage more facile although faradaic charges were not reported in this study.[112]

One of the more well studied replacement systems for OER is the oxidation of 5-Hydroxymethylfurfural (HMF) into its various products, ideally into the $6e^-$ product 2,5,-furandicarboxylic acid (FDCA) which has been proposed as an alternative precursor in the production of polymeric materials, replacing terephthalic acid. One of the earliest examples of this transformation was published in 1991 using a NiOx electrode with 84% faradaic efficiency for FDCA, and no trace of other products formed at pH 14.[113] On cobalt based materials there have been studies showing high charge efficiencies for FDCA.[40, 94, 114-116] One such study synthesized

various cobalt based metalloids showing both high activity and selectivity for the oxidation of HMF to FDCA using a cobalt boride electrode.[117] A different study using the Co-P system for HMF oxidation also reported a high product selectivity for FDCA in their system.[118] A mechanistic study performed years later on cobalt-based electrodes attempted to understand the role of the Co^{3+} and Co^{4+} redox couple observed in CV measurements on the product selectivity for HMF oxidation (Figure 1.6).[119] Through both computation and experimental results, the group suggests when the Co^{3+} ion is the dominate species, the oxidation of the hydroxyl group is sluggish, shifting the major product from FDCA to 5-hydroxymethyl-2-furancarboxylic acid (HMFCA) the $2e^-$ product, while when Co^{4+} is present the complete oxidation of the HMF substrate to is observed FDCA as the rate limiting step shifts from oxidation of the formyl group, to the oxidation of the Co^{3+} centers into Co^{4+}. This suggests that through modifications of the material and potential, one can tune product distributions in the alcohol oxidation reaction.

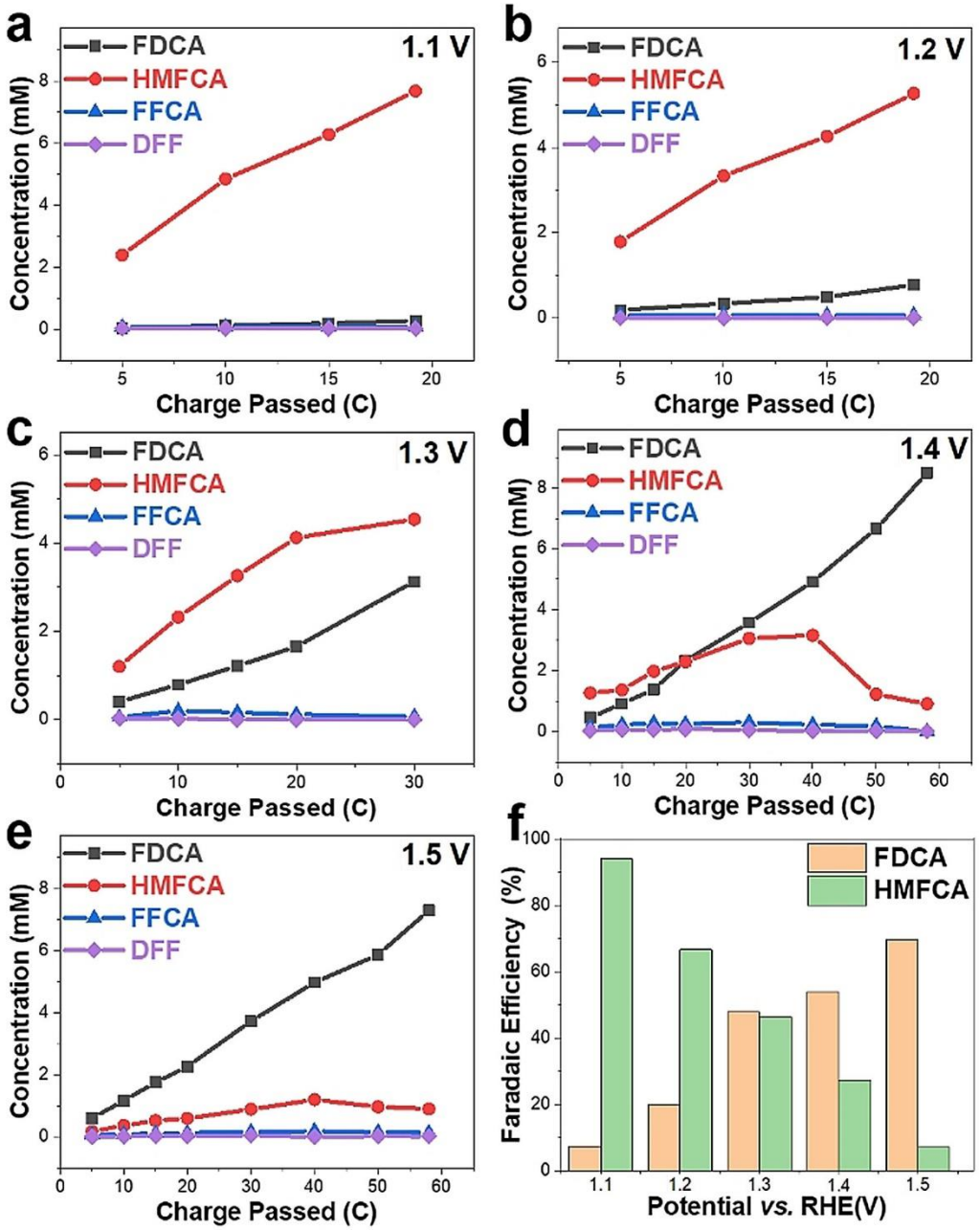

Figure 1.6 Electrolysis information from Co_3O_4 electrolysis of HMF at various potentials highlighting the switch in product formation about 1.3V vs RHE, which is close to the potential of the Co^{3+}/Co^{4+} redox couple. This figure is reprinted with permission from Xiaohui Deng, GeYang Xu, Yue-Jiao Zhang, et al., *Angewandte Chemie International Edition*, 2021. Copyright Wiley 2021.

To increase oxidative activities researchers have added dopant ions into the systems to improve AOR activity as is observed in the OER. Iron dopants were some of the earliest employed dopant ions, as these dopants were also observed to drastically increase OER activities. Wang et al. looked at Fe doping and how that alters the activity for the oxidation of benzyl alcohol. They found that at 33% Fe doping the system operated at 1.428V vs RHE operating voltage at 10 mA/cm^2_{geo} current density. The authors suggest this is due to defect oxygen sites present in this system lowering the energy for OH* dissociation.[120] Zhao et al. studied cobalt nickel oxide materials for benzyl alcohol oxidation, showing a low Ni doping level increased the material conductivity resulting in a more active catalytic material. The authors report a faradaic efficiency for the $4e^-$ oxidation to benzyl alcohol of 96% with no detected $2e^-$ product via GC sample injection.[92] In another study, Wang and coworkers, looked at FeOOH electrodes as catalyst for a combined ethanol oxidation, hydrogen evolution cell showing a large increase in the activity in the anode upon addition of ethanol. However, in the combined cell this increase in activity on the anode was counteracted by a decrease in cathode activity due to the decreased water concentration for hydrogen production due to the added ethanol.[87] The group also suggests the formation of Fe^{4+} species increased activity through their DFT calculations.

Interestingly, the combination of Co/Ni into electrocatalysts shows great promise as materials for electrochemical alcohol oxidation. Individually both cobalt[101] and nickel[121, 122] oxide materials are active for alcohol oxidation. However, there appears to be an increase in overall activity when the two materials are combined.[102, 123-125] Early work on these systems focused on methanol oxidation and showed systems with good electrode stability and activity.[102, 123, 124, 126] Unfortunately, neither of these reports show product formation and it is assumed that all products in the system are complete oxidation of the methanol substrate. Ethanol oxidation by $NiCo_2O_4$

substrates has also been previously observed.[125] The authors in this report do not report product speciation from the reaction. However, they do suggest that either the Ni(III) or Co(IV) species is responsible for the catalytic ethanol oxidation, similar to what is suggested for unaltered Co_3O_4.[119] Therefore it can be inferred that the presence or absence of Ni or Co into a Co_3O_4 or NiO lattice respectively, will shift the redox potential of the catalytic active ion, making the system more active. Additional studies on ethanol and ethylene glycol using Ni/CoOx spinel materials showed that the system is active for oxidation of diols as well, with the major product reported for these systems being the complete oxidation of the alcohol into the carboxylic acid product, either acetic acid for ethanol or oxalic acid for ethylene glycol.[127] This work found Ni increased the charge transport ability of the material through EIS which they claim helped increase the activity in these samples. They also note that materials with a higher Ni content showed lower activity which is attributes to the sluggish desorption of oxidative intermediates, blocking active sites for further turnover. Other reports suggest the Co atoms act to increase the conductivity of these systems, and describe the active sites of the material to the Ni surface atoms, and not cobalt atoms.[128] Recent work with these types of catalysts has looked into HMF oxidation where similar results to those observed for cobalt based materials is seen.[129, 130] Similar to other alcohols Ni incorporation into the cobalt spinel lattice also increases the activity for HMF oxidation, with the current density at 1.53V vs RHE increasing from 8.17 mA/cm^2 to 14.83 mA/cm^2 with the addition of Ni to the lattice (Figure 1.7).[129] The selectivity for FDCA in these systems remains over 90%. Using XANES (X-ray adsorption near edge spectroscopy) the authors in this report suggest that cobalt sites are the active sites for alcohol oxidation.[129]

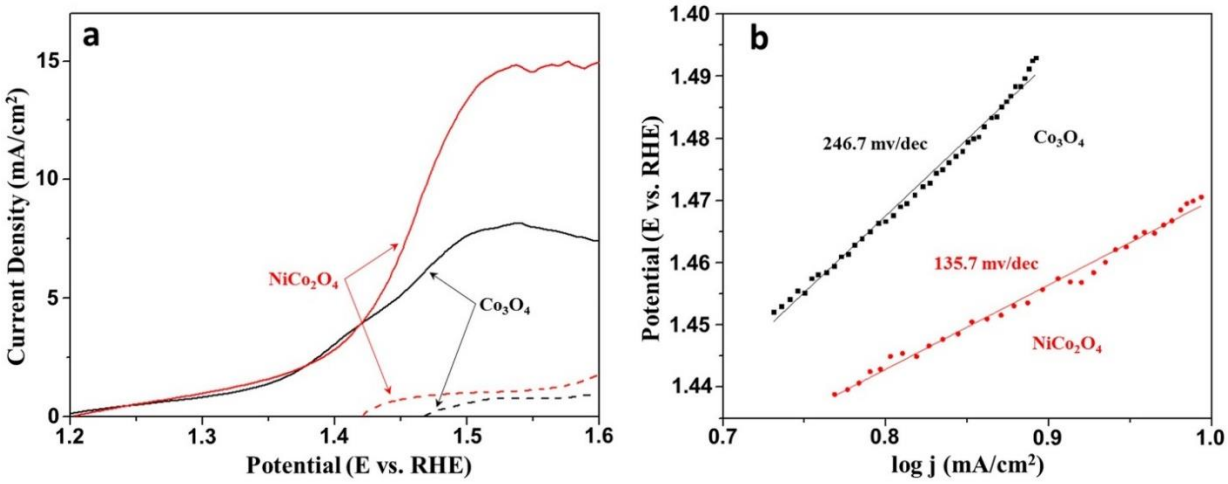

Figure 1.7 Alcohol oxidation Linear Sweep Voltammograms on Co_3O_4 (black) and $NiCo_2O_4$ (red) for HMF oxidation and the corresponding Tafel information showing the increased activity upon addition of Ni into the system. This figure is reprinted with permission from Myung Jong Kang, Heesun Park, Jonggeon Jegal, Sung Yeon Hwang, Young Soo Kang, Hyun Gil Cha, *Applied Catalysis B: Environmental*, 2019. Copyright Elsevier 2018.

Most reports on Ni incorporated cobalt materials for alcohol oxidation showing an increase in activity relative to the parent materials suggests a synergistic effect between Co and Ni sites in the lattice. This is similar to what is observed in the OER literature for similar systems.[131] In the alcohol oxidation system with these catalysts, it is debated wither this synergistic effect alters the active Co species,[127, 129] or the active Ni species,[128, 130, 132, 133] and the active site for alcohol oxidation is not well defined. XPS data taken before and after oxidation of HMF shows a transition in the Ni-O state to more of a Ni-OOH state,[130] which supports the active Ni^{3+} state theory. However it must be noted, ex situ measurements cannot fully determine what the changes to the system are while under applied electrochemical bias. A study looking at NiOx electrodes and how the incorporation of Fe and Co affect the activity for alcohol oxidation suggests that due to the shifts in the Ni^{2+}/Ni^{3+} redox couple with the addition of Fe and Co, and the corresponding shift in activity that correlated well with the shift in this couple, that Ni is the dominate catalytic active site.[132]

Mechanistically there is evidence that these transition metal systems produce carboxylic acid products selectivity past the $Co^{3+/4+}$ redox couple as discussed previously. This has been shown to be the case not only for the oxidation of HMF, but also for shorter chain alcohols like methanol. Spectroscopic evidence of methanol oxidation on a Ni based electrode shows the major product formed is formic acid in this system at pH 13.[134] Additional studies on similar surfaces show through electrochemical methods oxidation reaction in both methanol and ethanol oxidation is a 4 electron event, suggesting the formation of the carboxylic acid products.[135] These studies are also related to studies where it has been shown that these catalysts do not show increased electrode activity when formic acid is added to the system but does show increased response when formaldehyde is added to the solution suggesting favorable formation of the carboxylic acid

product over gas phase CO_2.[136] Formaldehyde oxidation is also observed at less positive potentials than methanol oxidation.[136] This suggests two different mechanisms exist for the oxidation of the alcohol group and the first intermediate aldehyde. The oxidation of the acid product is then kinetically sluggish allowing for the formation of the $4e^-$ product to be observed. These studies combined create the idea that through using alcohols as an oxidant one can produce carboxylic acids, but more importantly it suggests that the different mechanisms for alcohol oxidation and aldehyde oxidation would allow for product distributions to be changed through electrochemical modifications.

A simple mechanism for the oxidation of an organic alcohol can be seen in figure 1.8. This mechanism is the simplest case that accounts for all the information available in the literature. After the oxidation of the Co^{3+} to a Co^{4+}, an attack by an alcohol or alkoxide occurs. This is followed by a deprotonation and oxidation at the carbon center of the alcohol, prior to the elimination of the produced aldehyde by a solution phase hydroxide. This proposed mechanism is the simplest mechanism that can be proposed that takes into account the information present in the literature. This information being the requirement of the cobalt oxidation state change[119] from a Co^{3+} to a Co^{4+} as well as the pKa dependence of the alcohol noted by Koper.[103] Further work is required to gain more insight into the specific pathway that the oxidation of alcohols takes on cobalt oxide surfaces.

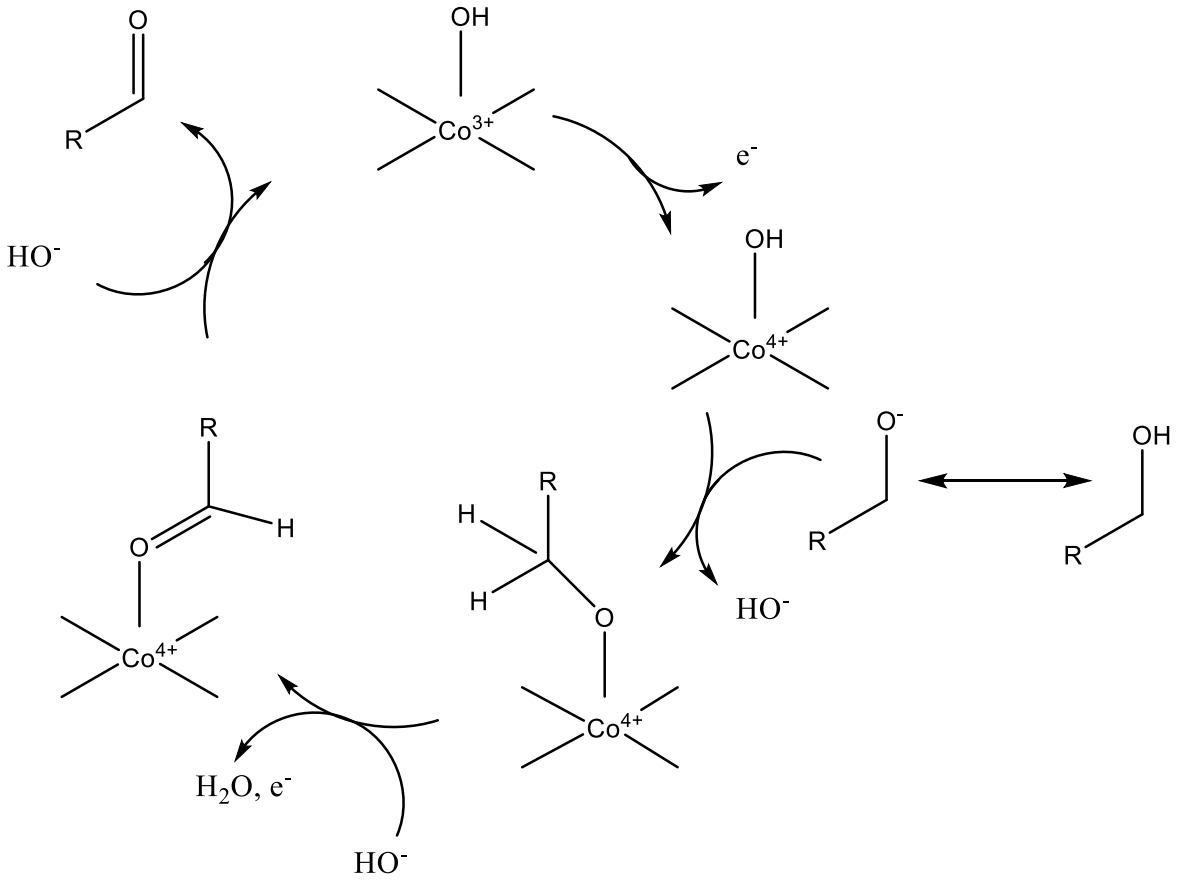

Figure 1.8 A proposed mechanism for the oxidation of an organic alcohol on a Cobalt Oxide surface. This process is the simplest mechanism that can be written with the information available in the literature.

The motivation for this dissertation began as a means to fill the gap in the OER literature between making active materials and understanding what specifically makes and active material. Through systematic modification of cobalt-based spinel catalysts with various transition metals I believed these trends in the OER activity would led to the understanding of what makes one dopant ion better than another, as well as give insight into how to develop new, state of the art, transition metal based OER catalysts, which combine the effects derived from the systematic studies. Over the course of performing this work, the project began to transition, developing into highlighting highly important aspects to performing studies on OER catalysts, while also changing the focus into how different substrates can be used as the oxidant in the hydrogen production system, offering the ability to lower the operating voltages of the system, while also producing a value-added product at the anode.

My work serves to further all areas of research discuss in this chapter and will be outlined in chapters 2-4. In chapter 2, I will discuss how various dopants alter the activity for OER and possible reasons why the trends that were expected based off the literature cited here, may not transfer to our system studied. In chapter 3, I will expand on the use of dopant ions for oxygen evolution, this time critically outlying reasons for analysis of the materials both before and after electrolysis using a specific case study material. In chapter 4, I will discuss my work furthering the field of electrochemical alcohol oxidation discussing the trends observed through a variety of substrates and electrochemical conditions.

1.6 References

1. J. Rugolo and M. J. Aziz, *Energy & Environmental Science*, 2012, **5**, 7151-7160.

2. A. A. Solomon, M. Child, U. Caldera and C. Breyer, *Energy Procedia*, 2017, **135**, 283-293.
3. N. S. Lewis and D. G. Nocera, *Proceedings of the National Academy of Sciences*, 2006, **103**, 15729.
4. M. Wieliczko and N. Stetson, *MRS Energy & Sustainability*, 2020, **7**, E41.
5. N. Nelson and A. Ben-Shem, *Nature Reviews Molecular Cell Biology*, 2004, **5**, 971-982.
6. J. R. McKone, S. C. Marinescu, B. S. Brunschwig, J. R. Winkler and H. B. Gray, *Chemical Science*, 2014, **5**, 865-878.
7. C. C. L. McCrory, S. Jung, I. M. Ferrer, S. M. Chatman, J. C. Peters and T. F. Jaramillo, *Journal of the American Chemical Society*, 2015, **137**, 4347-4357.
8. F.-Y. Yu, Z.-L. Lang, L.-Y. Yin, K. Feng, Y.-J. Xia, H.-Q. Tan, H.-T. Zhu, J. Zhong, Z.-H. Kang and Y.-G. Li, *Nature Communications*, 2020, **11**, 490.
9. C. C. L. McCrory, S. Jung, J. C. Peters and T. F. Jaramillo, *Journal of the American Chemical Society*, 2013, **135**, 16977-16987.
10. C. Spöri, P. Briois, H. N. Nong, T. Reier, A. Billard, S. Kühl, D. Teschner and P. Strasser, *ACS Catalysis*, 2019, **9**, 6653-6663.
11. Q. Wang, C.-Q. Xu, W. Liu, S.-F. Hung, H. Bin Yang, J. Gao, W. Cai, H. M. Chen, J. Li and B. Liu, *Nature Communications*, 2020, **11**, 4246.
12. J. Jirkovský, M. Makarova and P. Krtil, *Electrochemistry Communications*, 2006, **8**, 1417-1422.
13. T. Naito, T. Shinagawa, T. Nishimoto and K. Takanabe, *Inorganic Chemistry Frontiers*, 2021, **8**, 2900-2917.
14. T. Nishimoto, T. Shinagawa, T. Naito and K. Takanabe, *Journal of Catalysis*, 2020, **391**, 435-445.
15. K. Hans Wedepohl, *Geochimica et Cosmochimica Acta*, 1995, **59**, 1217-1232.
16. M. S. Burke, M. G. Kast, L. Trotochaud, A. M. Smith and S. W. Boettcher, *Journal of the American Chemical Society*, 2015, **137**, 3638-3648.
17. J. Wang, J. Liu, B. Zhang, F. Cheng, Y. Ruan, X. Ji, K. Xu, C. Chen, L. Miao and J. Jiang, *Nano Energy*, 2018, **53**, 144-151.
18. M. Yang, X. Fu, M. Shao, Z. Wang, L. Cao, S. Gu, M. Li, H. Cheng, Y. Li, H. Pan and Z. Lu, *ChemElectroChem*, 2019, **6**, 2050-2055.
19. M. Zhang, M. de Respinis and H. Frei, *Nature Chemistry*, 2014, **6**, 362.
20. M. Tang and Q. Ge, *Chinese Journal of Catalysis*, 2017, **38**, 1621-1628.
21. R. L. Doyle and M. E. G. Lyons, *Physical Chemistry Chemical Physics*, 2013, **15**, 5224-5237.
22. Q. He, Y. Wan, H. Jiang, Z. Pan, C. Wu, M. Wang, X. Wu, B. Ye, P. M. Ajayan and L. Song, *ACS Energy Letters*, 2018, **3**, 1373-1380.
23. F. Zhou, A. Izgorodin, R. K. Hocking, L. Spiccia and D. R. MacFarlane, *Advanced Energy Materials*, 2012, **2**, 1013-1021.
24. K. Mette, A. Bergmann, J.-P. Tessonnier, M. Hävecker, L. Yao, T. Ressler, R. Schlögl, P. Strasser and M. Behrens, *ChemCatChem*, 2012, **4**, 851-862.
25. Z. Abdi, R. Bagheri, M. Reza Mohammadi, Z. Song, M. Görlin, H. Dau and M. M. Najafpour, *Chemistry – A European Journal*, 2021, **27**, 1330-1336.
26. F. Dionigi, Z. Zeng, I. Sinev, T. Merzdorf, S. Deshpande, M. B. Lopez, S. Kunze, I. Zegkinoglou, H. Sarodnik, D. Fan, A. Bergmann, J. Drnec, J. F. d. Araujo, M. Gliech, D.

Teschner, J. Zhu, W.-X. Li, J. Greeley, B. R. Cuenya and P. Strasser, *Nature Communications*, 2020, **11**, 2522.
27. A. Badruzzaman, A. Yuda, A. Ashok and A. Kumar, *Inorganica Chimica Acta*, 2020, **511**, 119854.
28. F. Yang, K. Sliozberg, I. Sinev, H. Antoni, A. Bähr, K. Ollegott, W. Xia, J. Masa, W. Grünert, B. R. Cuenya, W. Schuhmann and M. Muhler, *ChemSusChem*, 2017, **10**, 156-165.
29. M. S. Burke, L. J. Enman, A. S. Batchellor, S. Zou and S. W. Boettcher, *Chemistry of Materials*, 2015, **27**, 7549-7558.
30. K. Cysewska, M. K. Rybarczyk, G. Cempura, J. Karczewski, M. Łapiński, P. Jasinski and S. Molin, *Materials (Basel)*, 2020, **13**, 2662.
31. C.-C. Lin and C. C. L. McCrory, *ACS Catalysis*, 2017, **7**, 443-451.
32. S. Jung, C. C. L. McCrory, I. M. Ferrer, J. C. Peters and T. F. Jaramillo, *Journal of Materials Chemistry A*, 2016, **4**, 3068-3076.
33. S. E. Michaud, M. T. Riehs, W.-J. Feng, C.-C. Lin and C. C. L. McCrory, *Chemical Communications*, 2021, **57**, 883-886.
34. T. Zhang, M. R. Nellist, L. J. Enman, J. Xiang and S. W. Boettcher, *ChemSusChem*, 2019, **12**, 2015-2021.
35. P. T. Babar, A. C. Lokhande, B. S. Pawar, M. G. Gang, E. Jo, C. Go, M. P. Suryawanshi, S. M. Pawar and J. H. Kim, *Applied Surface Science*, 2018, **427**, 253-259.
36. S. Heidari, S. E. Balaghi, A. S. Sologubenko and G. R. Patzke, *ACS Catalysis*, 2021, **11**, 2511-2523.
37. K. H. Cho, H. Seo, S. Park, Y. H. Lee, M. Y. Lee, N. H. Cho and K. T. Nam, *Advanced Functional Materials*, 2020, **30**, 1910424.
38. M. Fekete, R. K. Hocking, S. L. Y. Chang, C. Italiano, A. F. Patti, F. Arena and L. Spiccia, *Energy & Environmental Science*, 2013, **6**, 2222-2232.
39. C. Bocca, A. Barbucci, M. Delucchi and G. Cerisola, *International Journal of Hydrogen Energy*, 1999, **24**, 21-26.
40. B. J. Taitt, D.-H. Nam and K.-S. Choi, *ACS Catalysis*, 2019, **9**, 660-670.
41. R. D. L. Smith, M. S. Prévot, R. D. Fagan, S. Trudel and C. P. Berlinguette, *Journal of the American Chemical Society*, 2013, **135**, 11580-11586.
42. F. Dionigi, T. Reier, Z. Pawolek, M. Gliech and P. Strasser, *ChemSusChem*, 2016, **9**, 962-972.
43. R. D. L. Smith, M. S. Prévot, R. D. Fagan, Z. Zhang, P. A. Sedach, M. K. J. Siu, S. Trudel and C. P. Berlinguette, *Science*, 2013, **340**, 60.
44. T. Takashima, S. Hemmi, Q. Liu and H. Irie, *Catalysis Science & Technology*, 2020, **10**, 3748-3754.
45. J. Zou, G. Peleckis, C.-Y. Lee and G. G. Wallace, *Chemical Communications*, 2019, **55**, 8808-8811.
46. M. Gao, W. Sheng, Z. Zhuang, Q. Fang, S. Gu, J. Jiang and Y. Yan, *Journal of the American Chemical Society*, 2014, **136**, 7077-7084.
47. R. Agoston, M. Abu Sayeed, M. W. M. Jones, M. D. de Jonge and A. P. O'Mullane, *Analyst*, 2019, **144**, 7318-7325.
48. Y. Li, X. Du, J. Huang, C. Wu, Y. Sun, G. Zou, C. Yang and J. Xiong, *Small*, 2019, **15**, 1901980.

49. A. Munir, T. u. Haq, A. Qurashi, H. u. Rehman, A. Ul-Hamid and I. Hussain, *ACS Applied Energy Materials*, 2019, **2**, 363-371.
50. X. Zhao, X. Ding, Y. Xia, X. Jiao and D. Chen, *ACS Applied Nano Materials*, 2018, **1**, 1476-1483.
51. X. Guo, R.-M. Kong, X. Zhang, H. Du and F. Qu, *ACS Catalysis*, 2018, **8**, 651-655.
52. W. Kanan Matthew and G. Nocera Daniel, *Science*, 2008, **321**, 1072-1075.
53. S. E. S. El Wakkad and A. Hickling, *Transactions of the Faraday Society*, 1950, **46**, 820-824.
54. P. Benson, G. W. D. Briggs and W. F. K. Wynne-Jones, *Electrochimica Acta*, 1964, **9**, 275-280.
55. P. Benson, G. W. D. Briggs and W. F. K. Wynne-Jones, *Electrochimica Acta*, 1964, **9**, 281-288.
56. H. Dau, C. Limberg, T. Reier, M. Risch, S. Roggan and P. Strasser, *ChemCatChem*, 2010, **2**, 724-761.
57. J. Mei, T. Liao, G. A. Ayoko, J. Bell and Z. Sun, *Progress in Materials Science*, 2019, **103**, 596-677.
58. N.-T. Suen, S.-F. Hung, Q. Quan, N. Zhang, Y.-J. Xu and H. M. Chen, *Chemical Society Reviews*, 2017, **46**, 337-365.
59. T. Zhou, W. Xu, N. Zhang, Z. Du, C. Zhong, W. Yan, H. Ju, W. Chu, H. Jiang, C. Wu and Y. Xie, *Advanced Materials*, 2019, **31**, 1807468.
60. M. Yu, Z. Wang, C. Hou, Z. Wang, C. Liang, C. Zhao, Y. Tong, X. Lu and S. Yang, *Advanced Materials*, 2017, **29**, 1602868.
61. K. M. Shaju, L. Guerlou-Demourgues, G. Godillot, F. Weill and C. Delmas, *Journal of The Electrochemical Society*, 2012, **159**, A1934-A1940.
62. Q. He, Q. Li, S. Khene, X. Ren, F. E. López-Suárez, D. Lozano-Castelló, A. Bueno-López and G. Wu, *The Journal of Physical Chemistry C*, 2013, **117**, 8697-8707.
63. X. Li, J. Wei, Q. Li, S. Zheng, Y. Xu, P. Du, C. Chen, J. Zhao, H. Xue, Q. Xu and H. Pang, *Advanced Functional Materials*, 2018, **28**, 1800886.
64. M. Bajdich, M. García-Mota, A. Vojvodic, J. K. Nørskov and A. T. Bell, *Journal of the American Chemical Society*, 2013, **135**, 13521-13530.
65. G. S. Hutchings, Y. Zhang, J. Li, B. T. Yonemoto, X. Zhou, K. Zhu and F. Jiao, *Journal of the American Chemical Society*, 2015, **137**, 4223-4229.
66. Y. Zhang, F. Ding, C. Deng, S. Zhen, X. Li, Y. Xue, Y.-M. Yan and K. Sun, *Catalysis Communications*, 2015, **67**, 78-82.
67. J. Zhou, L. Zhang, Y.-C. Huang, C.-L. Dong, H.-J. Lin, C.-T. Chen, L. H. Tjeng and Z. Hu, *Nature Communications*, 2020, **11**, 1984.
68. Y. Chen, J. Hu, H. Diao, W. Luo and Y.-F. Song, *Chemistry – A European Journal*, 2017, **23**, 4010-4016.
69. L. Xu, Q. Jiang, Z. Xiao, X. Li, J. Huo, S. Wang and L. Dai, *Angewandte Chemie International Edition*, 2016, **55**, 5277-5281.
70. A. Bergmann, E. Martinez-Moreno, D. Teschner, P. Chernev, M. Gliech, J. F. de Araújo, T. Reier, H. Dau and P. Strasser, *Nature Communications*, 2015, **6**, 8625.
71. H. Lee, J. Y. Kim, S. Y. Lee, J. A. Hong, N. Kim, J. Baik and Y. J. Hwang, *Scientific Reports*, 2018, **8**, 16777.
72. A. Badreldin, A. E. Abusrafa and A. Abdel-Wahab, *ChemSusChem*, 2021, **14**, 10-32.

73. M. Yu, E. Budiyanto and H. Tüysüz, *Angewandte Chemie International Edition*, 2021, **n/a**.
74. D. K. Bediako, A. M. Ullman and D. G. Nocera, in *Solar Energy for Fuels*, eds. H. Tüysüz and C. K. Chan, Springer International Publishing, Cham, 2016, DOI: 10.1007/128_2015_649, pp. 173-213.
75. W. J. King and A. C. C. Tseung, *Electrochimica Acta*, 1974, **19**, 493-498.
76. W. J. King and A. C. C. Tseung, *Electrochimica Acta*, 1974, **19**, 485-491.
77. D. Guo, H. Kang, P. Wei, Y. Yang, Z. Hao, Q. Zhang and L. Liu, *CrystEngComm*, 2020, **22**, 4317-4323.
78. Y. Cui, Y. Xue, R. Zhang, J. Zhang, X. a. Li and X. Zhu, *Journal of Materials Chemistry A*, 2019, **7**, 21911-21917.
79. K. Y. Leung and C. C. L. McCrory, *ACS Applied Energy Materials*, 2019, **2**, 8283-8293.
80. R. Wei, X. Bu, W. Gao, R. A. B. Villaos, G. Macam, Z.-Q. Huang, C. Lan, F.-C. Chuang, Y. Qu and J. C. Ho, *ACS Applied Materials & Interfaces*, 2019, **11**, 33012-33021.
81. P.-S. Hung, W.-A. Chung, S.-C. Chou, K.-C. Tso, C.-K. Chang, G.-R. Wang, W.-Q. Guo, S.-C. Weng and P.-W. Wu, *Catalysis Science & Technology*, 2020, **10**, 7566-7580.
82. S. Yao, H. Wei, Y. Zhang, X. Zhang, Y. Wang, J. Liu, H. H. Tan, T. Xie and Y. Wu, *Catalysis Science & Technology*, 2021, **11**, 264-271.
83. Y. Xue, G. Ma, X. Wang, M. Jin, E. M. Akinoglu, D. Luo and L. Shui, *ACS Applied Materials & Interfaces*, 2021, **13**, 7334-7342.
84. J. Li, D. Chu, H. Dong, D. R. Baker and R. Jiang, *Journal of the American Chemical Society*, 2020, **142**, 50-54.
85. M. Cui, X. Ding, X. Huang, Z. Shen, T.-L. Lee, F. E. Oropeza, J. P. Hofmann, E. J. M. Hensen and K. H. L. Zhang, *Chemistry of Materials*, 2019, **31**, 7618-7625.
86. M. T. Bender, X. Yuan and K.-S. Choi, *Nature Communications*, 2020, **11**, 4594.
87. G.-F. Chen, Y. Luo, L.-X. Ding and H. Wang, *ACS Catalysis*, 2018, **8**, 526-530.
88. A. J. Motheo, G. Tremiliosi-Filho, E. R. Gonzalez, K. B. Kokoh, J. M. Léger and C. Lamy, *Journal of Applied Electrochemistry*, 2006, **36**, 1035-1041.
89. J. Na, B. Seo, J. Kim, C. W. Lee, H. Lee, Y. J. Hwang, B. K. Min, D. K. Lee, H.-S. Oh and U. Lee, *Nature Communications*, 2019, **10**, 5193.
90. G. Zhao, C. Fang, J. Hu and D. Zhang, *ChemPlusChem*, 2021, **86**, 574-586.
91. D. H. Nagaraju and V. Lakshminarayanan, *The Journal of Physical Chemistry C*, 2009, **113**, 14922-14926.
92. G. Liu, X. Zhang, C. Zhao, Q. Xiong, W. Gong, G. Wang, Y. Zhang, H. Zhang and H. Zhao, *New Journal of Chemistry*, 2018, **42**, 6381-6388.
93. Q. Zhang, X. Fu, Q. Kan and J. Guan, *Industrial & Engineering Chemistry Research*, 2019, **58**, 4774-4779.
94. Z. Zhou, C. Chen, M. Gao, B. Xia and J. Zhang, *Green Chemistry*, 2019, **21**, 6699-6706.
95. L. Du, Y. Sun and B. You, *Materials Reports: Energy*, 2021, **1**, 100004.
96. K. Li and Y. Sun, *Chemistry – A European Journal*, 2018, **24**, 18258-18270.
97. J. Zhang, S. Lu, Y. Xiang and S. P. Jiang, *ChemSusChem*, 2020, **13**, 2484-2502.
98. A. V. Tripković, K. D. Popović, J. D. Lović, V. M. Jovanović and A. Kowal, *Journal of Electroanalytical Chemistry*, 2004, **572**, 119-128.
99. J. L. Cohen, D. J. Volpe and H. D. Abruña, *Physical Chemistry Chemical Physics*, 2007, **9**, 49-77.

100. A. K. Das, S. Jena, S. Sahoo, R. Kuchi, D. Kim, T. A. Aljohani, G. C. Nayak and J.-R. Jeong, *Journal of Saudi Chemical Society*, 2020, **24**, 434-444.
101. J. B. Wu, Z. G. Li, X. H. Huang and Y. Lin, *Journal of Power Sources*, 2013, **224**, 1-5.
102. A. R. Jadhav, H. A. Bandal, A. A. Chaugule and H. Kim, *Electrochimica Acta*, 2017, **240**, 277-287.
103. Y. Kwon, S. C. S. Lai, P. Rodriguez and M. T. M. Koper, *Journal of the American Chemical Society*, 2011, **133**, 6914-6917.
104. Y. Kwon and M. T. M. Koper, *Analytical Chemistry*, 2010, **82**, 5420-5424.
105. R. M. L. M. Sandrini, J. R. Sempionatto, G. Tremiliosi-Filho, E. Herrero, J. M. Feliu, J. Souza-Garcia and C. A. Angelucci, *ChemElectroChem*, 2019, **6**, 4238-4245.
106. J. F. Gomes and G. Tremiliosi-Filho, *Electrocatalysis*, 2011, **2**, 96-105.
107. A. C. Garcia, M. J. Kolb, C. van Nierop y Sanchez, J. Vos, Y. Y. Birdja, Y. Kwon, G. Tremiliosi-Filho and M. T. M. Koper, *ACS Catalysis*, 2016, **6**, 4491-4500.
108. Z. Zhang, L. Xin, J. Qi, Z. Wang and W. Li, *Green Chemistry*, 2012, **14**, 2150-2152.
109. L. Dai, Q. Qin, X. Zhao, C. Xu, C. Hu, S. Mo, Y. O. Wang, S. Lin, Z. Tang and N. Zheng, *ACS Central Science*, 2016, **2**, 538-544.
110. Z. Yin, Y. Zheng, H. Wang, J. Li, Q. Zhu, Y. Wang, N. Ma, G. Hu, B. He, A. Knop-Gericke, R. Schlögl and D. Ma, *ACS Nano*, 2017, **11**, 12365-12377.
111. Y. Cao, D. Zhang, X. Kong, F. Zhang and X. Lei, *Journal of Materials Science*, 2021, **56**, 6689-6703.
112. S. Sun, L. Sun, S. Xi, Y. Du, M. U. Anu Prathap, Z. Wang, Q. Zhang, A. Fisher and Z. J. Xu, *Electrochimica Acta*, 2017, **228**, 183-194.
113. G. Grabowski, J. Lewkowski and R. Skowroński, *Electrochimica Acta*, 1991, **36**, 1995.
114. C. Wang, H.-J. Bongard, M. Yu and F. Schüth, *ChemSusChem*, 2021, **n/a**.
115. X. Huang, J. Song, M. Hua, Z. Xie, S. Liu, T. Wu, G. Yang and B. Han, *Green Chemistry*, 2020, **22**, 843-849.
116. R. Zhang, S. Jiang, Y. Rao, S. Chen, Q. Yue and Y. Kang, *Green Chemistry*, 2021, **23**, 2525-2530.
117. J. Weidner, S. Barwe, K. Sliozberg, S. Piontek, J. Masa, U.-P. Apfel and W. Schuhmann, *Beilstein Journal of Organic Chemistry*, 2018, **14**, 1436-1445.
118. N. Jiang, B. You, R. Boonstra, I. M. Terrero Rodriguez and Y. Sun, *ACS Energy Letters*, 2016, **1**, 386-390.
119. X. Deng, G.-Y. Xu, Y.-J. Zhang, L. Wang, J. Zhang, J.-F. Li, X.-Z. Fu and J.-L. Luo, *Angewandte Chemie International Edition*, 2021, **n/a**.
120. Y. Huang, R. Yang, G. Anandhababu, J. Xie, J. Lv, X. Zhao, X. Wang, M. Wu, Q. Li and Y. Wang, *ACS Energy Letters*, 2018, **3**, 1854-1860.
121. R. S. Amin, R. M. A. Hameed, K. M. El-Khatib, M. E. Youssef and A. A. Elzatahry, *Electrochimica Acta*, 2012, **59**, 499-508.
122. X. Tong, Y. Qin, X. Guo, O. Moutanabbir, X. Ao, E. Pippel, L. Zhang and M. Knez, *Small*, 2012, **8**, 3390-3395.
123. T.-H. Ko, K. Devarayan, M.-K. Seo, H.-Y. Kim and B.-S. Kim, *Scientific Reports*, 2016, **6**, 20313.
124. R. Ding, L. Qi, M. Jia and H. Wang, *Catalysis Science & Technology*, 2013, **3**, 3207-3215.
125. J. Zhan, M. Cai, C. Zhang and C. Wang, *Electrochimica Acta*, 2015, **154**, 70-76.

126. Z. Li, R. Yang, B. Li, M. Yu, D. Li, H. Wang and Q. Li, *Electrochimica Acta*, 2017, **252**, 180-191.
127. S. Sun, Y. Zhou, B.-L. Hu, Q. Zhang and Z. Xu, *Journal of The Electrochemical Society*, 2016, **163**, H99-H104.
128. G. Liu, C. Zhao, G. Wang, Y. Zhang and H. Zhang, *Journal of Colloid and Interface Science*, 2018, **532**, 37-46.
129. M. J. Kang, H. Park, J. Jegal, S. Y. Hwang, Y. S. Kang and H. G. Cha, *Applied Catalysis B: Environmental*, 2019, **242**, 85-91.
130. L. Gao, Y. Bao, S. Gan, Z. Sun, Z. Song, D. Han, F. Li and L. Niu, *ChemSusChem*, 2018, **11**, 2547-2553.
131. Q. Zhao, J. Yang, M. Liu, R. Wang, G. Zhang, H. Wang, H. Tang, C. Liu, Z. Mei, H. Chen and F. Pan, *ACS Catalysis*, 2018, **8**, 5621-5629.
132. D. Martín-Yerga, G. Henriksson and A. Cornell, *Electrocatalysis*, 2019, **10**, 489-498.
133. V. Hassanzadeh, M. A. Sheikh-Mohseni and B. Habibi, *Journal of Electroanalytical Chemistry*, 2019, **847**, 113200.
134. D. Chen and S. D. Minteer, *Journal of Power Sources*, 2015, **284**, 27-37.
135. J. B. Raoof, R. Ojani and S. R. Hosseini, *South African Journal of Chemistry*, 2013, **66**, 47-53.
136. D. Chen, G. G. W. Lee and S. D. Minteer, *ECS Electrochemistry Letters*, 2012, **2**, F9-F13.

Chapter 2 Systematic Activity Trends in $Co_{3-x}M_xO_4$ Based Catalysts: Effects of Al, Ga and Fe on Electrochemical Oxygen Evolution Activity

2.1 Preface

This chapter discusses the oxygen evolution reaction activity of various metal doped $Co_{3-x}M_xO_4$ materials highlighting the activity trends observed. Following an initial screening in which the activity of all materials was found to be lower than the parent Co_3O_4, an in-depth study was performed using Fe as a dopant ion due to the previous literature in the field suggesting Fe is critical in improving OER activity with cobalt oxide based materials. Iron was shown to increase OER activity, but only at low dopant level, while at higher levels of Fe incorporation the electrocatalytic activity drops considerably. This result highlights the importance of generating a wide range of catalytic materials in developing activity trends within a subset of materials. This work is part of a manuscript in preparation of which I am the primary author responsible for material synthesis, electrochemical measurements, material analysis, and manuscript preparation. Author two assisted with material synthesis and powder X-ray diffraction measurements. The co-corresponding author assisted with synthesis of gallium and aluminum doped samples. My advisor Dr. Charles C. L. McCrory assisted with manuscript preparation and data interpretation.

2.2 Abstract

Transition metal doping into cobalt based oxide materials has been shown to greatly increase the activity of these systems for the oxygen evolution reaction. Previous studies on these materials suggest that iron is a vital element in the OER activity in these systems by creating active

surface structures. We studied the electrocatalytic activity trends for a range of $Co_{3-x}M_xO_4$ materials with a specific focus on Fe doped materials due to the reported high activity of these systems. Despite the high activity observed for low level Fe doped samples as iron levels increase, the activity is shown to plummet likely due to high resistance of these materials and of inactive iron oxide phases. This study serves to highlight differences between activity trends in electrodeposited crystalline materials and suggests a complex relationship exists between dopant ion identity and OER activity trends.

2.3 Introduction

Renewable energy sources such as photovoltaics (PV) and wind turbines, offer a viable alternative to the use of fossil fuels for large scale energy generation. However the intermittency of these energy sources limits their practical use as base load power stations.[1-5] Production of hydrogen through electrochemical water splitting offers a promising solution to this intermittency problem as gaseous hydrogen can be produced during peak times and then consumed when energy production is low.[6-9] That said, the sluggish kinetics at the anode in the oxygen evolution reaction (OER) limits the practicality of hydrogen gas produced through water splitting as an energy storage mechanism. Because of this interest in developing effective, and stable catalysts that operate at low overpotentials is of great interest.[10-12] Benchmarking standards based off RuO_2 and IrO_2 have shown to be highly active and stable, however the use expensive precious metals, making these catalysts less ideal for wide scale use in industrial applications.[13-16]

Recently, efforts to develop inexpensive and stable OER catalysts has been on the forefront of electrocatalytic water splitting research.[17-19] Of the solid state catalysts focused on for the OER, cobalt based oxide materials have been of particular interest due to their relatively good activity and their stability in alkaline conditions.[20-24] Various methods to improving upon the intrinsic

activity of the cobalt oxide materials have been attempted with transition metal doping being particularly interesting as a method for catalytic improvement. Dopants ions for cobalt oxides include a wide variety of different metals including but not limited to Fe, Ni, Zn, Mn, Mg, Cu, and Li.[25-32] For instance, $Zn_xCo_{3-x}O_4$[33] and $NiCo_2O_4$[33, 34] both show large activity increases for the OER compared to the parent Co_3O_4. Of the metals dopants already observed, the impact of Fe doping is most pronounced, with Fe atoms being considered vital in increasing OER activity on cobalt-based materials due to increased turnover at surface Fe sites resulting in lower observed overpotentials in these systems.[35-37]

Previously our group reported on a series of Cr doped $Co_{3-x}Cr_xO_4$ catalysts, and showed that Cr doping did increase the OER activity for all doped samples, however the activity reached a maximum at x=0.75 which we hypothesized was due to a combination of both lattice spacing, changing the energy of a bridged oxiperoxi intermediate, as well as the electropositive Cr changing the electrophilicity of the surface Co sites, making them more susceptible to hydroxyl attack.[38] Herein we expand upon our work on Cr doped $Co_{3-x}M_xO_4$, by looking into other dopant species, chosen systematically to further elucidate fundamental information regarding metal doped Co_3O_4 systems. Specifically, we look at Fe, Ga, and Al dopants to test the effects of dopant ion size, and electronegativity on OER activity, and based off these findings, we performed a more focused study on Fe doped $Co_{3-x}Fe_xO_4$ materials due to the previously reported importance of iron in the OER with first row transition metal catalysts.

2.4 Experimental

2.4.1 Materials

Unless otherwise noted, all commercial chemicals were used as received without further purification. Cobalt (II) Acetate ($CoOAc•4H_2O$) was purchased from Alfa Aesar. Sodium

hydroxide (NaOH, BioUltra), iron nitrate ($Fe(NO_3)_3 \cdot 9H_2O$), gallium nitrate ($Ga(NO_3)_3 \cdot 9H_2O$) and 5 wt % Nafion 117 solution (in a mixture of lower aliphatic alcohols and water) were purchased from Sigma Aldrich. Aluminum nitrate ($Al(NO_3)_3 \cdot 9H_2O$) was purchased through Strem chemicals. Nafion 117 solid membranes were purchased from Fuel Cell Store. Nitric Acid (HNO_3, Trace Metal) was purchased from Thermo Fisher Scientific. Isopropyl alcohol (C_3H_8O, ACS) was purchased from EMD Millipore. Nitrogen (N_2) was boil-off gas from a liquid nitrogen source. Oxygen (O_2, industrial grade) was purchased from Cryogenic Gases. All water used in this study was ultrapure water (18.2 MΩ cm resistivity) purified using a Thermo Scientific Barnstead^{TM} Nanopure water purification system.

2.4.2 Mixed Metal Oxide Synthesis

$Co_{3-x}M_xO_4$ nanoparticles were synthesized according to a modified pechinni method involving the thermal decomposition of a cobalt-metal oxalate gel precursors. The gel precursors were prepared by coprecipitation of stoichiometric amounts of cobalt $Co(OAc)_2 \cdot 4H_2O$ (Alfa Aesar, 98%) and the respective metal nitrate salt were mixed with oxalic acid in 50mL EtOH. For example, in the synthesis of $CoGa_2O_4$, 1.245g (5mmol) of $Co(OAc)_2$ and 2.557g (10mmol) $Ga(NO_3)_3 \cdot 9H_2O$ (Sigma, 98%) were added to 40mL of EtOH. For Fe and Al doped samples, $Fe(NO_3)_3 \cdot 9H_2O$ (Sigma, 98%) and $Al(NO_3)_3 \cdot 9H_2O$ (Stream, 98%) salts were used respectively. After dissolution of the metal salts, 10mL of 1.8M oxalic acid in ethanol was added dropwise while the solution was stirred, and heated at 50 °C. After reacting at 50 °C for 2 hr, solution was cooled and the solvent was removed by vacuum. The remaining gel precursor was heated to 400°C for 2hrs in air in a quartz crucible, yielding product nanoparticles. The particles were then ground in a mortar and pestle and then collected and stored for analysis.

2.4.3 Characterization

The phase of the as-synthesized powder was confirmed by powder X-ray diffraction (PXRD). PXRD data was collected using a Rigaku Miniflex 600 X-ray diffractometer with a Cu Kα radiation source (40 kV/15 mA). Peak matching was performed using the Jade software with reference materials collected from the ICSD-FIZ Karlsruhe. The BET (Brunauer-Emmet-Teller) surface areas of the $Co_{3-x}Me_xO_4$ material was estimated from N_2 adsorption/desorption isotherms in powder forms using a Micromeritics ASAP 2020 surface area and porosimetry analyzer. Prior to surface area measurements, the $Co_{3-x}Me_xO_4$ samples heated at 150°C for 8-12h, then immediately weighed and transferred to the sample tube for the measurement to remove solvent from the material. The surface area was calculated with the Brunauer-Emmett-Teller (BET) method in the relative pressure range of 0.005 to 0.25 of adsorption data.

The metal composition of the as-synthesized materials were determined using inductively-coupled plasma—mass spectrometry (ICP-MS) and X-ray photoelectron spectroscopy (XPS). For ICP-MS measurements, 10 mg of the as-synthesized samples were added to 10 mL of concentrated HNO_3 and the mixture was left to sit at 60°C for 2 hr until the particles fully dissolved. This solution was diluted with a 1M HNO_3 solution then used to analyze the Co:M ratio of the solution using a Perkin-Elmer Nexion 2000 ICP-MS. Calibration standards for cobalt (Ricca Chemical, 1000 ppm in 10% HNO_3) and iron (Sigma Aldrich, 1000 ppm in 10% HNO_3), gallium (Sigma Aldrich, 1000 ppm in 10% HNO_3), and aluminum (Sigma Aldrich, 1000 ppm in 10% HNO_3)were prepared by diluting the as received standard with 1M trace metal grade HNO_3 to create calibration standards at the 1, 5, 10, 20, and 50 ppm level. All samples were run against a Bi internal standard to ensure instrument stability.

XPS measurements were conducted on the dropcast films on glassy carbon electrodes. The XPS spectra were acquired on a Kratos Axis Ultra XPS with a monochromatic Al x-ray source

operating at 8 mA and 14 kV. High-resolution spectra were collected with a pass energy of 20 eV and a step size of 0.1 eV. The XPS peak positions were calibrated according to the sp^2 C 1s for adventitious carbon at 284.8 eV. XPS data analysis was processed using CasaXPS version 2.3.17 (Casa Software Ltd). To quantify elemental ratios, peaks in the XPS high-resolution were fit to symmetric Voight line shapes comprised of 10% Gaussian and 90% Lorentzian functions with a Shirley background. Elemental ratios were calculated by quantifying the total peak areas in the Co $2p_{3/2}$ peak and Me $2p_{3/2}$ peak and then dividing by their respective relative sensitivity factors (as tabulated for the Kratos Ultra XPS instrument).

2.4.4 Working Electrode Preparation

Glassy-carbon disks (diameter 5 mm, t=4 mm, 0.196 cm^2 surface area (Sigradur G, HTW Hochtemperatur-Werkstoff) were used as working electrodes. The disks were lapped with silicon carbide abrasive papers (CarbiMet 2, 600/P1200, Buehler) under 2N of pressure, followed by sequential polishing with diamond abrasive slurries (MetaDi Surpreme, Buehler) in an order of 9, 6, 3, 1, and 0.1 um diameter particle-based slurries (30 sec polishing each) on synthetic nap based polishing pads (MD Floc, Struers). The lapping and polishing were performed using a LaboSystem (LaboPol-5 and LaboForce-1, Struers). Before polishing, the disks were sonicated in solutions of isopropyl alcohol, water, and acetone for 1 min each. Following polishing, the disks were sonicated in a dilute solution of trace metal grade 1M nitric acid for twenty min, followed by sonication in isopropanol, water, and acetone for 1 min each and then blow dried with N_2. The catalysts were drop-casted onto the glassy-carbon electrodes from catalysts inks by following a reported protocol.[38, 39] Catalyst inks were made by adding 80 mg of the catalysts, 3.8 mL of water, 1 mL of isopropyl alcohol, and 40 ul of 5% Nafion 117 to a vial in sequential order. The inks were sonicated after addition of each sequential component and then sonicated for 10 min directly prior to

dropcasting onto the electrodes. 5 µl of catalyst ink was dropcasted onto each electrode which was then placed into an oven set at 70°C for 5 min. This was repeated for a total volume of 10 ul (calculated as 165 µg of the catalyst) of catalyst ink applied to each electrode. Before electrochemical analyses, the electrodes were cooled to room temp by being left open to atmosphere.

2.4.5 Electrochemical Analysis

Electrochemical measurements were conducted with a Bio-Logic SP200 or SP300 potentiostat/galvanostat. Catalyst-modified glassy carbon working electrodes were mounted into a Pine Instrument Company E6-series ChangeDisk RDE assembly and affixed to an MSR rotator (AFMSRCE, Pine Instrument Company). The reference electrode was a double frit Hg/HgO (1 M NaOH) electrode (CH Instruments), externally referenced vs a prepared reversible hydrogen electrode (RHE). The auxiliary electrodes were graphitic carbon rods (99.999%, Strem Chemicals). Prior to each set of measurements, the electrolyte solution was continuously sparged with O_2 for at least 30 min, and the solution was continuously sparged with O_2 during rotating disk electrode voltammetry (RDEV), chronoamperometry (CA), and chronopotentiometry (CP) measurements. A standard H-cell was used for activity measurements and stability measurements, with approximately 50 mL of 1M NaOH being added to the working compartment, containing the working electrode and the reference electrode, and the other compartment contained 20 mL of 1 M NaOH and a carbon rod counter electrode. A Teflon one compartment cell was used to corroborate the activity of all iron doped catalyst to remove trace iron from altering the observed OER activity trends. Prior to electrochemical measurements, solutions were sparged with O_2 for 30 minutes to saturate the solution with oxygen. During electrochemical measurements the solution was also blanketed by O_2 to maintain solution saturation. Cyclic voltammograms were

collected at 1600 rpm rotation rate, from 1.2V to 1.7V vs RHE at a scan rate of 20 mV/s and swept two times. Following the cyclic voltammograms, chronopotentiometric and chronoamperometric steps were conducted on the electrodes to obtain the activity at specific potentials and current densities for Tafel analysis, each step was held for 30s and data was recorded as the end point of these steps. Note that each electrochemical measurement was conducted at least three times, and reported values are averages of these runs. Prior to each set of experiments, the uncompensated solution resistance (Ru) was measured with a high-frequency single point impedance measurement at 100 kHz with a 20 mV amplitude about the open-circuit potential (OCP), and RDEV measurements were corrected for iR drop at 85% through positive feedback using the Bio-Logic ECLab software. Our typical electrochemical setup resulted in Ru ≈ 10 Ω in 1 M NaOH.

EIS data was collected using a Bio-Logic SP200 potentiostat/galvanostat. Catalyst-modified glassy carbon working electrodes were mounted into a Pine Instrument Company E6-series ChangeDisk RDE assembly and affixed to an MSR rotator (AFMSRCE, Pine Instrument Company). The reference electrode was a double frit Hg/HgO (1 M NaOH) electrode (CH Instruments), externally referenced vs a prepared reversible hydrogen electrode (RHE). The auxiliary electrodes were graphitic carbon rods (99.999%, Strem Chemicals). Solutions were sparged with O_2 prior to electrochemical measurements and blanketed with O_2 during the impedance measurements. Impedance measurements were taken at 1.6V vs RHE applied voltage. Scanning was performed from 10 kHz to 100 mHz with ten data points being collected per decade. An amplitude of 5mV was used and data points were taken in duplicate at each frequency. Recorded values are the average of three independent electrodes for each catalyst tested.

2.5 Results

2.5.1 Mixed Metal Oxide Characterization and Electrochemical Results

Mixed metal oxide preparation. $Co_{3-x}M_xO_4$ (x = 1, 2; M = Al, Fe, Ga) nanocrystals were prepared via a modified Pechini method. Briefly, metal nitrate solutions and citric acid formed gel precursors followed by calcination at 400°C under air for 2 hr which yielded nanoparticulate products. Figures A.1-A.3 show the powder X-ray diffraction (PXRD) patterns of the $Co_{3-x}Al_xO_4$, $Co_{3-x}Fe_xO_4$ and $Co_{3-x}Ga_xO_4$ series. For the dopants with larger ionic radii, specifically Fe^{3+} and Ga^{3+}, the diffraction peaks shift significantly towards lower angle region, indicating a dopant induced lattice expansion compared to the pristine Co_3O_4. In $Co_{3-x}Ga_xO_4$, albeit no Co_2GaO_4 pattern has been reported, the experimental data of the Co_2GaO_4 nanocrystals shows crystal lattice between $Co_{2.55}Ga_{0.45}O_4$ and $CoGa_2O_4$ references applying the agreement with the Vegard's law. For the commensurate Co^{3+} and Al^{3+} ions, slight peak shifts in Co_2AlO_4/$CoAl_2O_4$ towards high angel suggest minor lattice dimension reduction, about -0.2% and -0.6% for Co_2AlO_4 and $CoAl_2O_4$, respectively. Metal content analysis confirms the atomic ratio between Co and M, and specific surface area determined from N_2 physisorption serves as the parameterization to the intrinsic OER activity. Most of the compositions possess a surface area ca. 80 m^2/g. Table A.1 summarizes the lattice parameters, metal contents, and specific surface area data of the catalysts.

Catalyst OER activity measurements were performed following a previously reported protocol.[40] Catalyst films were drop casted onto glassy carbon electrodes reaching a mass loading of 0.84 mg/cm^2_{geo}. Short term activities were monitored using sets of RDEVs, CA, and CP measurements, while long term stability data were acquired using elongated CP and CP with repetitive CV scans. Both short and long term activity measurements were conducted at an electrode rotation rate of 1600 rpm in O_2-saturated 1 M NaOH. Representative CV measurements can be found in figure A4 for Ga and Al doped $Co_{3-x}M_xO_4$. Figure 2.1 highlights the overpotentials at 10 mA/cm^2 current density for the materials synthesized ordered by increasing atomic number.

All activities outside of those reported previously with Cr doping were found be to lower than the Co_3O_4 parent material. For Co_2AlO_4 and $CoAl_2O_4$, both show higher overpotentials, 0.54 ± 0.03 V and 0.46 ± 0.01 V, respectively, than that of Co_3O_4; Co_2GaO_4 shows worse activity as η = 0.5 ±0.02 V while $CoGa_2O_4$ shows similar activity as η = 0.41 ± 0.01 V Most interesting of these results is the activity of the Fe doped $Co_{3-x}M_xO_4$ samples, as much of the previous OER literature suggests the Fe is vital in the activity of cobalt based oxide materials for the OER, thus our expectation was that Fe doping should increase the OER activity. However, we did not see this expected result rather we noticed a stark decrease in OER activity with Fe doping at both the X=1 and X=2 levels where η=0.44 ± 0.01 V and η=0.46 ± 0.01 V respectively, directly contradicting other reports of Fe doped cobalt oxide systems.[36, 41, 42] Table A.2 summarize the remaining activity metrics for the catalysts synthesized. Potentiostatic measurements used to generate current density metrics were taken at η = 0.35 to evaluate the activity of the catalysts as well. This point is chosen as η = 0.35 the theorized minimal overpotential set on planar metal oxide electrodes in PV coupled water splitting devices under one sun illumination (AM 1.5G). Besides the OER activity, slopes provide more information about OER catalytic mechanisms or rate determining steps. Tafel slopes, taken near the linear region around j = 10 mA/cm^2_{geo}, can serve as the indicator to compare whether different dopants affect the OER catalytic mechanisms. Due to the multi-electron transfer complex nature of OER, Tafel slopes are not sufficient for explicit mechanistic analysis. The measured Tafel slopes are between 50-70 mv/dec for the metals tested, which are closed to what have been reported on Co_3O_4 based OER materials, despite some minor variations came from different sample preparation methods, electrolyte systems used, and measurement conditions. Due to the observed decreased activity with all samples in all metrics chosen, we sought out to observe the full activity trend in the $Co_{3-x}Fe_xO_4$ system to find if there were ratios that would increase the OER

activity. Due to the previously reported importance of Fe, we sought to develop a full trend to better compare with our previous reported Cr doped system and to better understand the role that Fe might play in the $Co_{3-x}M_xO_4$ system.[38]

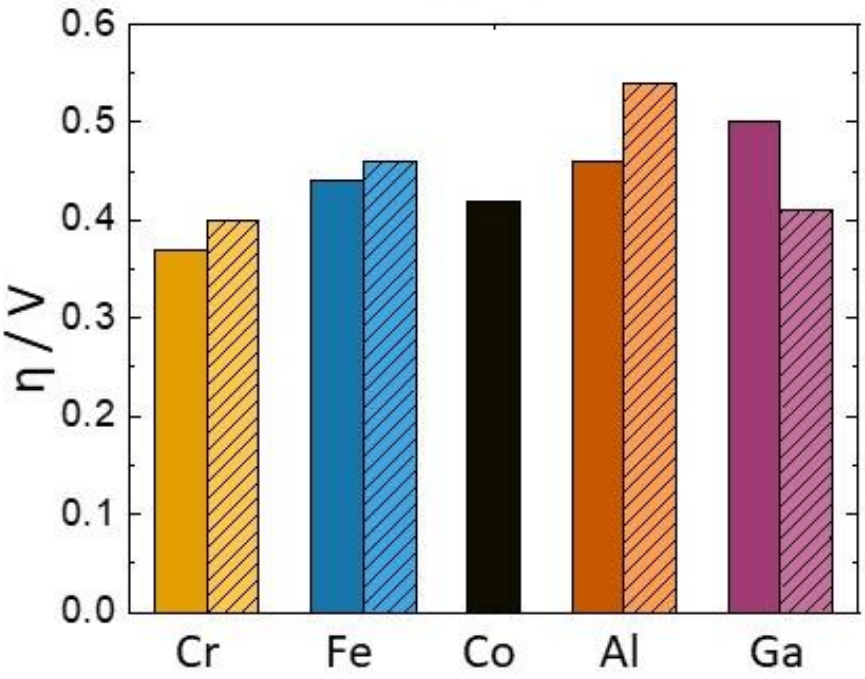

Figure 2.1 Overpotentials for various catalytic materials synthesized through the same method with different compositions highlighting the relative activity of the different compositions. Dopants are listed in order of increasing radius of the M^{3+} cation.

2.5.2 $Co_{3-x}Fe_xO_4$ Characterization and Electrochemical Results

A wider range of Fe doped materials with the formula $Co_{3-x}Fe_xO_4$ (x=0.25, 0.5, 0.75, 1, 1.25, 1.5, 1.75, 2) were synthesized through identical methods to those previously described.[38] Figure 2.2 shows the PXRD patterns of the synthesized nanoparticle products which shows the production of phase pure materials, evident by the absence of stray peaks in the diffraction patterns. Additionally, a clear and obvious shift in 2θ towards lower angle as the incorporation of Fe increases is observed, suggesting a lattice expansion is occurring which is to be expected with the replacement of Co^{3+} ions with larger Fe^{3+} ions. The lattice parameter of the nanocrystals was calculated from the (311) peak in the diffraction patterns and then plotted vs the expected lattice parameter based on Vegard's Law where Co_3O_4 and Fe_3O_4 were used as the end points. The data shows good agreement with the expected trend with some variation at higher Fe incorporation. XPS was performed to observe the environments of the iron and cobalt sites in the material and are shown in Figure A.6 and A.7, with Table A.3 summarizing the peak positions. The XPS suggests a mixed valance state in both Co and Fe atoms in the catalytic material as evident by broadened peaks and a lack of satellite peaks in the XPS spectrum.[43] To check the ratios of metal ion incorporation, ICP-MS was used to determine the Co:Fe ratio, which was then used to calculate out the bulk Co:Fe ratio. The ICP-MS Co:Fe ratio is plotted vs the expected Co:Fe ratio in Figure A.5 showing a strong correlation between synthetic ratios and bulk product ratios.

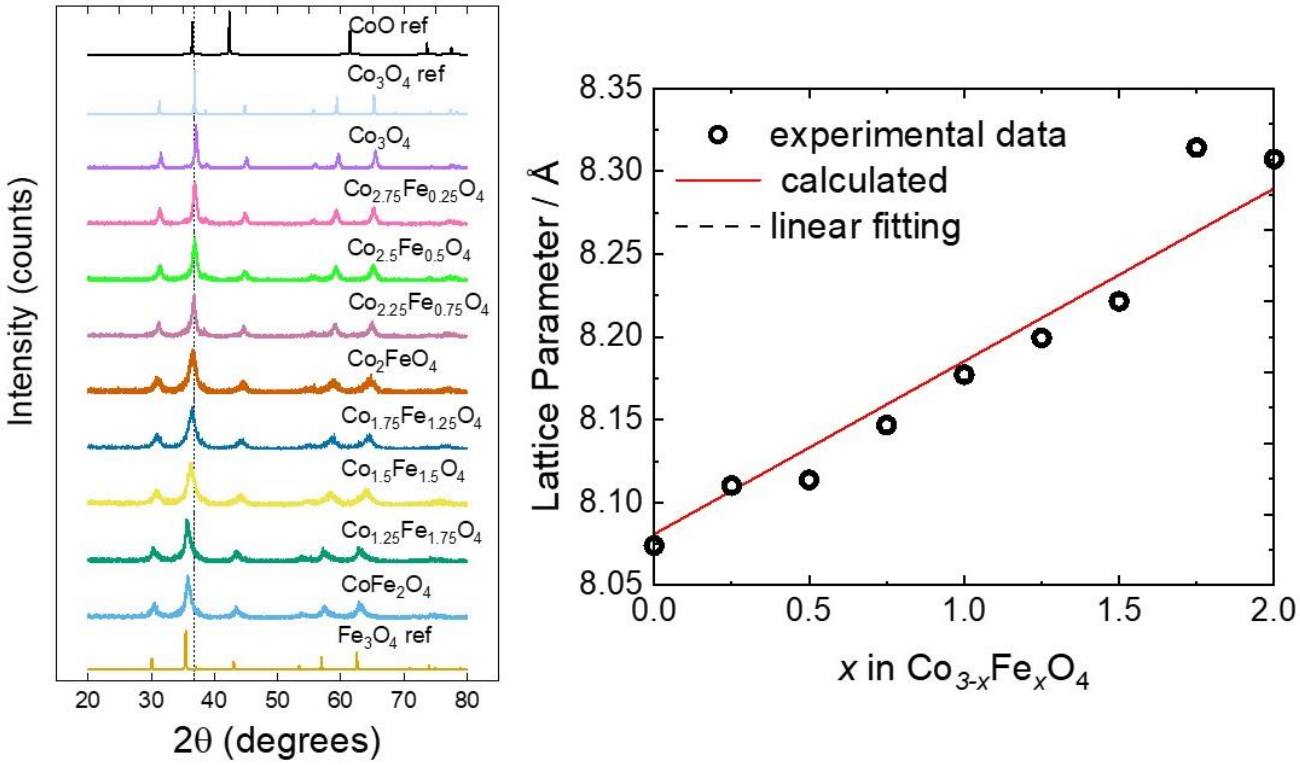

Figure 2.2 PXRD patterns of Fe doped $Co_{3-x}Fe_xO_4$ (left). A line over the (311) peak in Co_3O_4 is used as a guide to show the peak shift. Vigard's Law plot for the Synthesized samples as a function of synthetic Fe doping amount (right) showing good agreement between the expected value. The red trend line is fit to Co_3O_4 and Fe_3O_4 end points.

Activity for the oxygen evolution reaction (OER) was monitored using methods previously reported and are shown in Figure 2.3.[44, 45] A Teflon electrochemical cell was used for CV measurements to remove trace Fe from the system which has been shown to impact OER activity.[36] To confirm the absence of trace iron from the electrochemical cell, the cell was filled with 1M trace metal HNO_3 and allowed to sit for 24 hrs prior to electrochemical measurements. This acid was then directly injected into an ICP-MS to detect the undiluted iron levels within the cell that could be etched in a 24hr period. Iron levels in the cell were found to be below the LOQ for the instrument (1 ppb) suggesting trace iron is not present in quantifiable concentrations in this electrochemical cell. Representative CVs for these materials are reported in figure A.8. Figure 2.3 reports the worked up activity trends for all Fe doped materials in terms of three separate metrics, overpotential (η), as well as current density normalized for both geometric surface area and BET surface area. We normalize for BET surface area to give a better representation of our activity per electroactive surface area. We use BET surface area measurements for this normalization rather than electrochemical methods typically used to calculate the electroactive surface area, due to the well documented issues with methods such as double layer charging.[24, 46, 47] Initially there is an increase in activity upon Fe incorporation, consistent with previous reports of Fe doped cobalt oxide materials. Interestingly after X= 0.5 the activity starts to decrease as Fe content in increased in the lattice to the point where at $x \geq 1$ there is almost no activity at η=350 mV. This result was not predicted prior to measurements being taken, as literature suggests Fe doping even at the 66% level in different cobalt-based materials is shown to increase the activity for the OER.[36] Additionally there are reports for $CoFe_2O_4$ (X=2) systems which show improved OER activity.[48] However some comparable reports to our system show similar decrease in OER activity.[49, 50] Tafel

analysis was also performed and Tafel plots are shown in figure A.9 and the Tafel slopes are reported in Table A.2. All Tafel slopes are consistent with Tafel information for Co_3O_4 suggesting a similar mechanism for these materials. The exception is $Co_{2.75}Fe_{0.25}O_4$ which shoes a much steeper Tafel slope suggesting that there might be a mechanistic difference in the OER activity between this catalyst and all others tested in this study. This also suggests that the increased activity of this material at low overpotentials does not scale as the potential is shifted more positive.

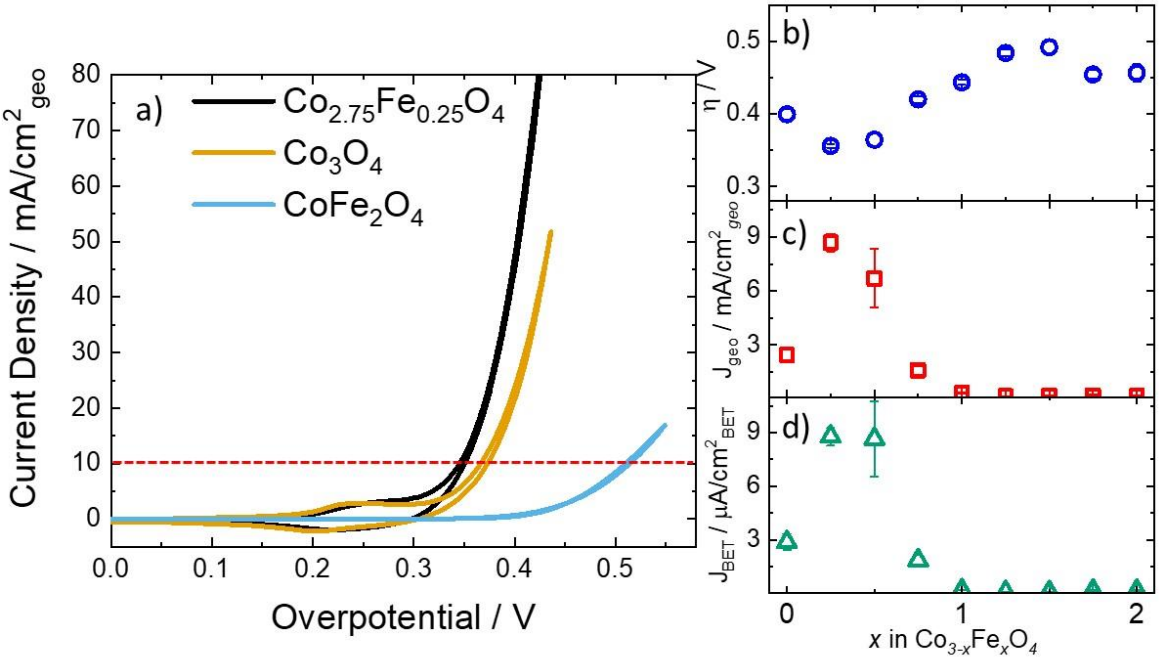

Figure 2.3 Comparative plots of OER activities as a function of iron content. a) Shows representative cyclic voltammograms for select iron doped $Co_{3-x}Fe_xO_4$ catalysts. b) shows the relative overpotentials at 10mA/cm^2 current density for all Fe doped catalyst. The overpotential was recorded after the electrode was held at 10mAcm^2 for 1 minute. c) shows the geometric activity of the catalysts at η=350mV d) shows the current density at η=350mV normalized for the real surface area as determined by BET gas adsorption. Current densities were recorded after the electrode was held for 1 minute at η=350mV.

Stability tests were performed via cycling and long-term electrolysis for $Co_{2.75}Fe_{0.25}O_4$, the most active of our samples to observe how the activity changed under these conditions. Figure 2.4 shows the average activity as the catalyst is held at 10mA/cm^2_{geo} current density for 24 hours, and also after cycling for 10,000 cycles (roughly 24 hrs). In the constant potential measurements, a stable current is held for the first 10 hours of the experiment however on average the activity then starts to decrease over time, this however we assign to catastrophic film failure which we previously reported in Cr doped Co_3O_4[38] and can be observed in the current traces in figure A.11. Upon cycling there is there is some slight decay in the activity of the catalyst over the duration of the experiment, most of this decay is in the first two hours of cycling (10000 cycles), which is assessed to leaching of small amounts of Fe from the catalyst surface due to the solubility of FeO_x in alkaline media. This effect is lessened when Fe is incorporated into a structure with other metals, mainly Ni [41] and Co [35], however leaching still occurs. We then performed post electrocatalytic XPS and XRD on the $Co_{2.75}Fe_{0.25}O_4$ material. The post XPS showed little change in the peak shapes from the pre electrocatalytic measurements to the pose electrocatalytic measurements, suggesting environmental stability of Fe and Co sites in the system, additionally there was little change in the composition of the materials as the Co:M ratio was found to be consistent both before and after electrocatalysis via ICS-MS the small change in composition may be attribute to Fe leaching, however solution phase Fe was not able to be quantified due to limitations with the ICP-MS instrument with our electrolyte solution. The post electrocatalytic XRD also showed no large structural changes occur over the duration of electrocatalytic measurements evident by the retention of crystallinity, and no shift in the XRD peaks in the diffraction patterns for both $Co_{2.75}Fe_{0.25}O_4$ and Co_2FeO_4.

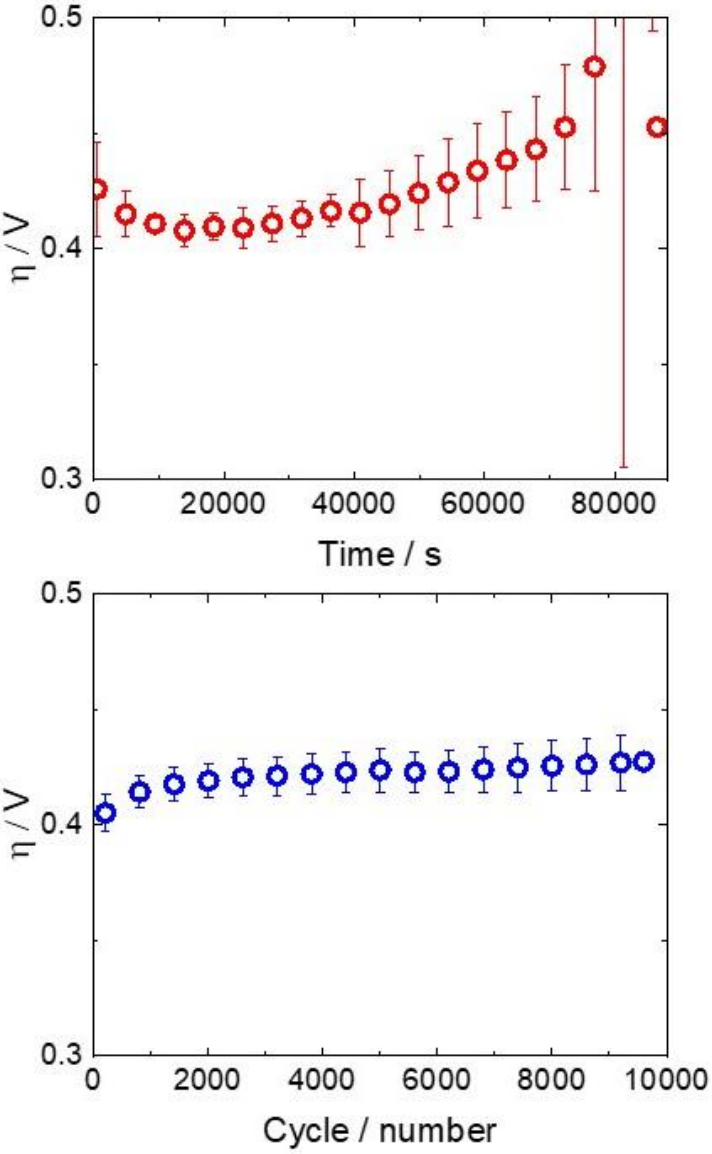

Figure 2.4 Shows the Activity of $Co_{2.75}Fe_{0.25}O_4$ catalysts upon controlled current and cycling measurements. Controlled current measurements were held at 10mA/cm^2 current density for the duration of the experiment. Cycling was performed between η=0V and η=500mV at 10mA/cm^2 current density. The X axis of cycles for cycling measurements aligns with the time axis in the controlled current measurements.

Electrochemical impedance spectroscopy (EIS) was used to estimate the charge transfer resistance of the catalyst materials. A circuit model similar to one published elsewhere for cobalt iron oxides was used to account for the double hemispherical shape of the Nyquist plot. This is attributed to the presence of two series RC circuits. The first is a typical resistive element due to the electrochemical double layer where the second is a result of the insulating properties of iron oxide within the core, limiting charge transport through the catalyst.[51, 52] All samples were analyzed with the same circuit model for consistency. Figure A.10 shows a plot of the charge transfer resistance within the catalyst as a function of the iron doping content. We observe an increase in this resistive element in the circuit with increasing iron content suggesting the increased presence of iron limits electron transport within the system. This result is similar to that seen elsewhere in the literature for iron doped samples.[50]

2.6 Discussion

The rationale behind the activity for cobalt based oxide materials has been a widely discussed topic in the OER literature.[53-58] Multiple studies suggest that the adsorption of various surface intermediates is the largest factor impacting the OER activity, with the CoOOH intermediate being the most critical of these intermediates.[36, 59, 60] This same CoOOH intermediate has been shown through various experimental studies using in situ FTIR (Fourier-transform infrared spectroscopy) and XAS (X-ray absorption spectroscopy) to be active sites for OER in these systems.[22, 61] Fe incorporation into a $NiCoPO_4$ catalyst for OER is suggested to increase the rate of formation of the CoOOH intermediate by making the Co centers more polarizable, as the Fe atoms remove electron density from the cobalt sites. This electronegativity argument was previously used by our group as a possible reason for the activity increase observed when using Cr as a dopant ion.[38, 62] Examples of a second mechanism for OER is proposed where rather than

the formation of a CoOOH at a single atoms site, a duel Co atom mechanism is proposed is suggested to be a faster mechanism than the alternative single site mechanism.[22, 57] In a previous study, we suggested that with Cr incorporation and subsequent lattice expansion, the stabilization of this two site mechanism assists in increasing the activity of the OER. At higher Cr dopant levels however, this same lattice expansion then serves to limit OER activity by destabilizing the bridged intermediate system. These two effects, the electronegativity and the metal site distance, were the main explanations that we used to interpret the results observed with Cr doping.[38] With this insight we anticipated the Fe doped system reported here would show increased activity at almost all dopant levels relative to Co_3O_4, due to the slight increase in electronegativity of the Co sites, coupled with only a slight change in the lattice parameter. However, neither of these hypotheses can fully explain the data obtained in this report, especially the precipitous decrease in activity observed in this Fe doped system past the x=0.5 dopant level. This leads us to hypothesize that the mechanistic interpretation used for the Cr doped system, does not directly transfer to the Fe doped system. Rather that there are other effects at play that dominate in $Co_{3-x}Fe_xO_4$ catalysts.

Multiple studies suggest the replacement of Co with Fe and subsequent increase in surface Fe atoms which have been suggested to be more active for OER, both in computational reports, as well as experimental reports.[36, 60, 63] This effect increase is large enough to impact the OER activity with trace levels of Fe in solution for both Co and Ni based oxide materials. Within these low level Fe doped samples, it is hypothesized that the Fe sites are order of magnitudes more active than either Co or Ni sites due to ensure this is right .[35, 36, 41, 64, 65] Other studies suggest that the incorporation of Fe atoms on electrodeposited CoFeOx surfaces increases the activity in two ways, the first is increasing the disproportionation of the bridged oxygen atoms in a di-cobalt center mechanism at less positive applied potentials. At more positive potentials Fe-Co bridged systems

are the active surface species, where the two site mechanistic pathway proposed for Co_3O_4 is still maintained.[22, 66] However, for our system to follow the hypothesis previously presented in the literature there should be an increase in OER activity observed well beyond the X=0.5 dopant level as observed here. This suggests the previously reported conclusions generated from non-crystalline systems may not directly carry over when a more defined crystal lattice is present, as is the case in this study. A similar effect is seen in previously reported $CoFe_2O_4$ system on N-doped graphene, where the more crystalline system, as defined by peak intensity in XRD, show the lowest activity for all $CoFe_2O_4$ systems tested, while the more amorphous systems showed higher activity. This also suggests there may be deviations from the amorphous trends observed elsewhere in the literature.[48]

The addition of Fe into multiple different systems has numerous electronic implications that have shown to possibly lead to increased OER activity.[35, 62, 67-71] A similar trend to the one observed here was recently published by Tüysüz and co-workers on Co/Fe oxide nanowires where the reverse trend was observed.[50] They showed an increase in activity at low Fe dopant levels and at higher levels of Fe doping the activity decreases drastically. Their findings showed an increase in charge transport at low Fe levels, evident by a decreased charge transfer resistance (R_{ct}) as calculated by EIS measurements. At higher Fe levels, an increase in R_{ct} as well as the presence of a second resistive element is observed. These effects are attributed to increased resistivity of the materials, and the presence of an insulating inner iron oxide layer limits the ability for catalytic turnover in their system. We observe a similar increase in R_{ct} for all our materials, with even the low dopant level $Co_{2.75}Fe_{0.25}O_4$ having a slightly higher charge transfer resistance than Co_3O_4 (Figure A.10). There is a large increase in the R_{ct} from the X=0.75 to X=1 dopant levels, consistent with the large decrease in catalytic current at 1.58V vs RHE for these systems. Although EIS for

these types of porous systems is nonideal for quantitative analysis of charge transfer resistance due to the complex surface structures present, the qualitative trends observed in the calculated R_{ct} likely suggests an increase in resistance impacts the catalytic ability of these systems.

An alternative viewpoint for the Fe doped system is that the system operates as a Co doped Fe_3O_4 system rather than a Fe doped Co_3O_4. When the Fe incorporation, and iron oxides are known to be both less active, and less stable catalyst for OER.[24, 37, 72-74] This type of behavior has been shown in the NiFeOx literature, where Bell and coworkers showed that at larger Fe levels, there were large facets of FeOx which were inactive for oxygen evolution, limiting the overall observed activity in these catalyst.[60] Other studies on FeOOH films, showed that for larger and thicker films, there was less activity for OER, which was attributed to the poor conductivity of FeOOH films at overpotentials negative of 400mV.[72] Our EIS results, summarized in Figure A.10, supports an decrease in conductivity, that likely could be the result of increased FeOOx layers under applied potentials, and with more iron included, the increased thickness of these facets may be responsible for the increased charge transfer resistance and thus the decreased OER activity.

The results collected in this study, mixed with previous literature leads us to believe that for the Fe doped spinel Co_3O_4 system, Fe is able to increase the activity at low levels as the system is conductive enough to allow for catalytic OER to occur through a similar mechanism to that hypothesized prior to the study where the electronegativity of the dopant allows for more facile CoOOH formation. However as the iron concentration within the system increases, the conductivity decreases which limits the ability for catalytic turnover. This effect is likely coupled with an increase in the number of exposed iron oxide rich facet which severely limit the ability for catalytic turnover within these systems. This interpretation suggests that to generate specific

activity trends with respect to iron incorporation, methods to increase the material conductivity must be taken in addition to systematic Fe doping so that conductivity issues can be mitigated.

2.7 Conclusion

In conclusion we report the effects of bulk Fe incorporation into the $Co_{3-x}Fe_xO_4$ system for the oxygen evolution reaction. At low dopant levels (x=0.25, 0.5), the activity for the OER shows a large shift towards lower η relative to the Co_3O_4 control. This is consistent with previous literature reports where they showed that low level Fe in solution results in a decrease in η for the OER. However, as Fe starts to make up a larger percentage of the lattice, the overpotential is shown to shift to more positive potentials and the activity at a given potential is much lower than that observed in the control material. We suggest this is due to two regimes forming, the first is the Fe poor system where material conductivity remains high allowing for increased catalytic turnover. The second region is Fe rich, creating regimes of electrically insulating, and catalytically inactive iron oxide, limiting the overall catalytic activity. These results suggest moving forward studies attempt to use methods of directly increasing the conductivity of the catalytic material and not just the catalytic substrate to generate transferable data sets for metal doping. Additionally, the results suggest activity trends do not transfer between amorphous materials into the crystalline phase.

2.8 References

1. M. L. Tuballa and M. L. Abundo, *Renewable and Sustainable Energy Reviews*, 2016, **59**, 710-725.
2. M. Graetzel, *Accounts of Chemical Research*, 1981, **14**, 376-384.
3. N. S. Lewis and D. G. Nocera, *Proceedings of the National Academy of Sciences*, 2006, **103**, 15729.
4. M. G. Walter, E. L. Warren, J. R. McKone, S. W. Boettcher, Q. Mi, E. A. Santori and N. S. Lewis, *Chemical Reviews*, 2010, **110**, 6446-6473.
5. A. J. Bard and M. A. Fox, *Accounts of Chemical Research*, 1995, **28**, 141-145.
6. T. R. Cook, D. K. Dogutan, S. Y. Reece, Y. Surendranath, T. S. Teets and D. G. Nocera, *Chemical Reviews*, 2010, **110**, 6474-6502.

7. N. S. Lewis, *Science*, 2007, **315**, 798.
8. G. W. Crabtree and M. S. Dresselhaus, *MRS Bulletin*, 2008, **33**, 421-428.
9. H. B. Gray, *Nature Chemistry*, 2009, **1**, 7-7.
10. R. Frydendal, E. A. Paoli, B. P. Knudsen, B. Wickman, P. Malacrida, I. E. L. Stephens and I. Chorkendorff, *ChemElectroChem*, 2014, **1**, 2075-2081.
11. J. A. Seabold and K.-S. Choi, *Journal of the American Chemical Society*, 2012, **134**, 2186-2192.
12. T. W. Kim and K.-S. Choi, *Science*, 2014, **343**, 990.
13. Z. Feng, W. T. Hong, D. D. Fong, Y.-L. Lee, Y. Yacoby, D. Morgan and Y. Shao-Horn, *Accounts of Chemical Research*, 2016, **49**, 966-973.
14. C. C. L. McCrory, S. Jung, J. C. Peters and T. F. Jaramillo, *Journal of the American Chemical Society*, 2013, **135**, 16977-16987.
15. C. C. L. McCrory, S. Jung, I. M. Ferrer, S. M. Chatman, J. C. Peters and T. F. Jaramillo, *Journal of the American Chemical Society*, 2015, **137**, 4347-4357.
16. S. Trasatti, *Electrochimica Acta*, 1984, **29**, 1503-1512.
17. D. Liu, P. Zhou, H. Bai, H. Ai, X. Du, M. Chen, D. Liu, W. F. Ip, K. H. Lo, C. T. Kwok, S. Chen, S. Wang, G. Xing, X. Wang and H. Pan, *Small*, 2021, **17**, 2101605.
18. J. Yang, M. J. Jang, X. Zeng, Y. S. Park, J. Lee, S. M. Choi and Y. Yin, *Electrochemistry Communications*, 2021, **131**, 107118.
19. Y.-C. Zhang, C. Han, J. Gao, L. Pan, J. Wu, X.-D. Zhu and J.-J. Zou, *ACS Catalysis*, 2021, **11**, 12485-12509.
20. J. D. Blakemore, H. B. Gray, J. R. Winkler and A. M. Müller, *ACS Catalysis*, 2013, **3**, 2497-2500.
21. F. Jiao and H. Frei, *Angewandte Chemie International Edition*, 2009, **48**, 1841-1844.
22. M. Zhang, M. de Respinis and H. Frei, *Nature Chemistry*, 2014, **6**, 362.
23. H. Tüysüz, Y. J. Hwang, S. B. Khan, A. M. Asiri and P. Yang, *Nano Research*, 2013, **6**, 47-54.
24. S. Jung, C. C. L. McCrory, I. M. Ferrer, J. C. Peters and T. F. Jaramillo, *Journal of Materials Chemistry A*, 2016, **4**, 3068-3076.
25. B. Chi, H. Lin and J. Li, *International Journal of Hydrogen Energy*, 2008, **33**, 4763-4768.
26. D. Pletcher, X. Li, S. W. T. Price, A. E. Russell, T. Sönmez and S. J. Thompson, *Electrochimica Acta*, 2016, **188**, 286-293.
27. T. W. Kim, M. A. Woo, M. Regis and K.-S. Choi, *The Journal of Physical Chemistry Letters*, 2014, **5**, 2370-2374.
28. J. Rosen, G. S. Hutchings and F. Jiao, *J. Catal.*, 2014, **310**, 2-9.
29. T. Y. Ma, S. Dai, M. Jaroniec and S. Z. Qiao, *Chemistry – A European Journal*, 2014, **20**, 12669-12676.
30. X. Wu and K. Scott, *Journal of Materials Chemistry*, 2011, **21**, 12344-12351.
31. T. Maiyalagan, K. A. Jarvis, S. Therese, P. J. Ferreira and A. Manthiram, *Nature Communications*, 2014, **5**, 3949.
32. C. Bocca, G. Cerisola, E. Magnone and A. Barbucci, *International Journal of Hydrogen Energy*, 1999, **24**, 699-707.
33. X. Liu, Z. Chang, L. Luo, T. Xu, X. Lei, J. Liu and X. Sun, *Chemistry of Materials*, 2014, **26**, 1889-1895.

34. R. N. Singh, M. Hamdani, J. F. Koenig, G. Poillerat, J. L. Gautier and P. Chartier, *Journal of Applied Electrochemistry*, 1990, **20**, 442-446.
35. T. Zhang, M. R. Nellist, L. J. Enman, J. Xiang and S. W. Boettcher, *ChemSusChem*, 2019, **12**, 2015-2021.
36. M. S. Burke, M. G. Kast, L. Trotochaud, A. M. Smith and S. W. Boettcher, *Journal of the American Chemical Society*, 2015, **137**, 3638-3648.
37. M. S. Burke, L. J. Enman, A. S. Batchellor, S. Zou and S. W. Boettcher, *Chemistry of Materials*, 2015, **27**, 7549-7558.
38. C.-C. Lin and C. C. L. McCrory, *ACS Catalysis*, 2017, **7**, 443-451.
39. S. E. Michaud, M. T. Riehs, W.-J. Feng, C.-C. Lin and C. C. L. McCrory, *Chemical Communications*, 2021, **57**, 883-886.
40. C. C. Lin and C. C. L. McCrory, *Acs Catal*, 2017, **7**, 443-451.
41. L. Trotochaud, S. L. Young, J. K. Ranney and S. W. Boettcher, *Journal of the American Chemical Society*, 2014, **136**, 6744-6753.
42. Y. Huang, R. Yang, G. Anandhababu, J. Xie, J. Lv, X. Zhao, X. Wang, M. Wu, Q. Li and Y. Wang, *ACS Energy Letters*, 2018, **3**, 1854-1860.
43. J. A. Moyer, C. A. F. Vaz, E. Negusse, D. A. Arena and V. E. Henrich, *Physical Review B*, 2011, **83**, 035121.
44. O. Khaselev and J. A. Turner, *Science*, 1998, **280**, 425.
45. J. A. Turner, *Science*, 1999, **285**, 687.
46. K. Klingan, F. Ringleb, I. Zaharieva, J. Heidkamp, P. Chernev, D. Gonzalez-Flores, M. Risch, A. Fischer and H. Dau, *ChemSusChem*, 2014, **7**, 1301-1310.
47. R. L. Doyle, I. J. Godwin, M. P. Brandon and M. E. G. Lyons, *Physical Chemistry Chemical Physics*, 2013, **15**, 13737-13783.
48. S. Li, J. Wang, J. Wang, C. Chen, Z. Guo, N. Cai, Y. Xue and F. Yu, *Colloids and Surfaces A: Physicochemical and Engineering Aspects*, 2021, **626**, 126898.
49. J. Xu, Y. Yang, W. Zhou, X. Ma, J. Xu, Y. Cao and H. Chai, *Journal of Solid State Chemistry*, 2021, **299**, 122106.
50. E. Budiyanto, M. Yu, M. Chen, S. DeBeer, O. Rüdiger and H. Tüysüz, *ACS Applied Energy Materials*, 2020, **3**, 8583-8594.
51. R. L. Doyle and M. E. G. Lyons, *Journal of The Electrochemical Society*, 2013, **160**, H142-H154.
52. M. E. G. Lyons and M. P. Brandon, *Journal of Electroanalytical Chemistry*, 2009, **631**, 62-70.
53. K. Song, E. Cho and Y.-M. Kang, *ACS Catalysis*, 2015, **5**, 5116-5122.
54. Y. Zhang, F. Ding, C. Deng, S. Zhen, X. Li, Y. Xue, Y.-M. Yan and K. Sun, *Catalysis Communications*, 2015, **67**, 78-82.
55. P. Tan, Z. Wu, B. Chen, H. Xu, W. Cai and M. Ni, *Electrochimica Acta*, 2019, **310**, 86-95.
56. J. R. Swierk and T. D. Tilley, *Journal of The Electrochemical Society*, 2017, **165**, H3028-H3033.
57. H.-Y. Wang, S.-F. Hung, Y.-Y. Hsu, L. Zhang, J. Miao, T.-S. Chan, Q. Xiong and B. Liu, *The Journal of Physical Chemistry Letters*, 2016, **7**, 4847-4853.
58. H. M. A. Amin and H. Baltruschat, *Physical Chemistry Chemical Physics*, 2017, **19**, 25527-25536.

59. M. W. Louie and A. T. Bell, *Journal of the American Chemical Society*, 2013, **135**, 12329-12337.
60. D. Friebel, M. W. Louie, M. Bajdich, K. E. Sanwald, Y. Cai, A. M. Wise, M.-J. Cheng, D. Sokaras, T.-C. Weng, R. Alonso-Mori, R. C. Davis, J. R. Bargar, J. K. Nørskov, A. Nilsson and A. T. Bell, *Journal of the American Chemical Society*, 2015, **137**, 1305-1313.
61. H.-Y. Wang, S.-F. Hung, H.-Y. Chen, T.-S. Chan, H. M. Chen and B. Liu, *Journal of the American Chemical Society*, 2016, **138**, 36-39.
62. K. Zhan, C. Feng, X. Feng, D. Zhao, S. Yue, Y. Li, Q. Jiao, H. Li and Y. Zhao, *ACS Sustainable Chemistry & Engineering*, 2020, DOI: 10.1021/acssuschemeng.9b07781.
63. B. M. Hunter, J. R. Winkler and H. B. Gray, *Molecules*, 2018, **23**, 903.
64. R. Wang, C. Wang, S. Yin, Y. Peng, J. Chen, Y. Deng and J. Li, *Catalysis Today*, 2020, DOI: https://doi.org/10.1016/j.cattod.2020.04.013.
65. J. Chang, L. Chen, S. Zang, Y. Wang, D. Wu, F. Xu, K. Jiang and Z. Gao, *Journal of Colloid and Interface Science*, 2020, **569**, 50-56.
66. R. D. L. Smith, C. Pasquini, S. Loos, P. Chernev, K. Klingan, P. Kubella, M. R. Mohammadi, D. Gonzalez-Flores and H. Dau, *Nature Communications*, 2017, **8**, 2022.
67. X.-Z. Liu, T. Tang, W.-J. Jiang, Q.-H. Zhang, L. Gu and J.-S. Hu, *Chemical Communications*, 2020, DOI: 10.1039/D0CC01024C.
68. S.-H. Ye, Z.-X. Shi, J.-X. Feng, Y.-X. Tong and G.-R. Li, *Angewandte Chemie International Edition*, 2018, **57**, 2672-2676.
69. E. Laouini, M. Hamdani, M. I. S. Pereira, J. Douch, M. H. Mendonça, Y. Berghoute and R. N. Singh, *International Journal of Hydrogen Energy*, 2008, **33**, 4936-4944.
70. C. Xiao, X. Lu and C. Zhao, *Chemical Communications*, 2014, **50**, 10122-10125.
71. Z. Zou, T. Wang, X. Zhao, W.-J. Jiang, H. Pan, D. Gao and C. Xu, *ACS Catalysis*, 2019, **9**, 7356-7364.
72. M. S. Burke, S. Zou, L. J. Enman, J. E. Kellon, C. A. Gabor, E. Pledger and S. W. Boettcher, *The Journal of Physical Chemistry Letters*, 2015, **6**, 3737-3742.
73. L. Fan, B. Zhang, B. J. J. Timmer, N. V. R. A. Dharanipragada, X. Sheng, C.-W. Tai, F. Zhang, T. Liu, Q. Meng, A. K. Inge and L. Sun, *Nano Energy*, 2020, **72**, 104656.
74. M. E. G. Lyons and M. P. Brandon, *Journal of Electroanalytical Chemistry*, 2010, **641**, 119-130.

Chapter 3 A CoV_2O_4 Precatalyst for the Oxygen Evolution Reaction: Highlighting the Importance of Postmortem Electrocatalyst Characterization

3.1 Preface

In this chapter I discuss a CoV_2O_4 catalyst for the OER which shows good OER activity. However, when this activity is normalized for BET surface area, the activity is found to drastically increase relative to the parent Co_3O_4 system. Upon further analysis, this activity is found not to be due to incorporation of vanadium ions as the catalyst decomposes under OER conditions to form an amorphous vanadium free material, which shows good OER activity and stability after initial vanadium leaching. This work serves as a case study into the critical importance of post-mortem material analysis in electrocatalysis when attempting to rationalize OER activity changes. This chapter of my dissertation is derived from the manuscript originally published in the journal *Chemical Communications* 2021, **57**, 883-886. I am the first author of this manuscript responsible for writing the manuscript, electrochemical measurements, material analysis, and material synthesis. Author two was responsible for powder X-ray diffraction measurements. Author three was responsible for pre electrolysis XPS measurements. Co-corresponding author was responsible for initial material synthesis. My advisor Dr. Charles. C. L. McCrory was responsible for assisting with manuscript preparation and for data interpretation. Reproduced from Michaud, S. E., Riehs, M. T., Feng, W., Lin, C. C., McCrory, C. C. L., *Chem Comm*, 2021, **57**, 883-886. with permission from the Royal Society of Chemistry.

3.2 Abstract

Vanadium-doped cobalt oxide materials have emerged as a promising class of catalysts for the oxygen evolution reaction. Previous studies suggest vanadium doping in crystalline Co spinel materials tunes the electronic structure and stabilizes surface intermediates. We report a CoV_2O_4 material that shows good activity for the oxygen evolution reaction. However, postmortem characterization of the catalyst material shows dissolution of vanadium resulting in an amorphous CoOx material suggesting that this vanadium-free material, and not CoV_2O_4, is the active catalyst. This study highlights the importance of postmortem characterization prior to mechanistic and computational analysis for this class of materials.

3.3 Introduction

The sluggish kinetics of the oxygen evolution reaction (OER) hinders the development of practical water-splitting technologies, and has driven the search for efficient OER electrocatalysts comprised of earth-abundant materials that operate with high current densities at low overpotential with long-term operational stability.[1-4] V-doped Co oxide materials have recently emerged as a promising class of alkaline OER catalysts. Previous studies of V-doped Co oxide materials showed increased activity for the OER at low overpotentials,[5-14] and typically suggest that this increased activity is a result of changes to the catalyst's electronic structure and/or in increased stabilization of adsorbed OER intermediates.[5-8]

In this study, we report a CoV_2O_4 material that shows exceptional specific activity per BET surface area for the OER based on as-synthesized characterization data. However, materials characterization conducted after OER electrolysis shows the CoV_2O_4 precatalyst transforms into a V-free amorphous Co-based material during the OER. This suggests that V ions are not present in the active catalyst material, rather, CoV_2O_4 serves as a template for the generation of an active

amorphous CoO_x species. Our study highlights the need for careful postmortem characterization of electrocatalytic materials to ensure continued catalyst integrity prior to conducting detailed mechanistic interpretations

3.4 Experimental

3.4.1 Materials

Unless otherwise noted, all commercial chemicals were used as received without further purification. Cobalt (II) Oxide (CoO, 99+%) was purchased from Acros Organics. Vanadium (III) Oxide (V_2O_3, 97%) was purchased from Alfa Aesar. Sodium hydroxide (NaOH, BioUltra), ferrocenecarboxylic acid ($C_{11}H_{10}FeO_2$, 97%), sodium phosphate monobasic dihydrate ($NaH_2PO_4 \cdot 2H_2O$, ACS grade) and 5 wt % Nafion 117 solution (in a mixture of lower aliphatic alcohols and water) were purchased from Sigma Aldrich. Nafion 117 solid membranes were purchased from Fuel Cell Store. Nitric Acid (HNO_3, Trace Metal) was purchased from Thermo Fisher Scientific. Isopropyl alcohol (C_3H_8O, ACS) was purchased from EMD Millipore. Nitrogen (N_2) was boil-off gas from a liquid nitrogen source. Oxygen (O_2, industrial grade) was purchased from Cryogenic Gases. All water used in this study was ultrapure water (18.2 MΩ cm resistivity) purified using a Thermo Scientific Barnstead™ Nanopure water purification system.

3.4.2 Synthesis and deposition of CoV_2O_4

CoV_2O_4 was prepared by solid state synthesis from CoO and V_2O_3 metal precursors. A 1:1 molar ratio of CoO (1 mmol, 0.075 g) and V_2O_3 (1 mmol, 0.150 g) were ground and mixed with an agate mortar and pestle, and then compressed into a pellet with a hydraulic press die at an applied pressure of 12,000 psi. The resulting pellet was heated under Ar first to 500 °C with a heat ramp of 5 °C/min, and then to 800 °C with a heat ramp of 5 °C/min. The pellet was then held at

800 °C for 20 h under Ar. The resulting material was then ground in an agate mortar and pestle to obtain a powder form.

5 mm diameter glassy carbon disks (4 mm thick, 0.196 cm^2 surface area, Sigradur G, HTW Hochtemperatur-Werkstoffe GmbH) or 1.6 cm × 3.2 cm glassy carbon plates (0.1 mm thick, 5.1 cm^2 surface area, HTW Hochtemperatur-Werkstoffe GmbH) were used as working electrodes. The glassy carbon disks were lapped with silicon carbide abrasive papers (CarbiMet 2, 600/P1200, Buehler), followed by sequential polishing with diamond abrasive slurries (MetaDi Supreme, Buehler) in an order of 9 µm, 6 µm 3 µm 1 µm and 0.1 µm diameter particle slurries (1 min polishing each) on synthetic nap based polishing pads (MD Floc, Struers). Between each lapping and polishing step, the disks were sonicated for ~30 s in isopropyl alcohol. The lapping and polishing were performed using a Struers LaboPol-5 polisher with a LaboForce-1 specimen mover. The disks were held in the LaboForce-1 specimen mover with 5 psi of applied pressure per disk, and during lapping and polishing the platen speed was held at 200 rpm and the head speed at 8 rpm in the opposite rotation direction from the platen. The glassy carbon plates were polished by hand using the same polishing order as the disks: first grinding by hand on the silicon carbide abrasive paper followed by sequential polishing by hand with diamond abrasive slurries sequentially from 9 µm to 0.1 µm on the synthetic nap polishing pad. Between each lapping and polishing step, the plates were sonicated for ~30 s in isopropyl alcohol. After the final polishing step, the glassy carbon disks were sonicated in an 1M nitric acid solution for 10 min, followed by sequential 3 min sonication in acetone and then ultrapure water, and finally dried in an N_2 stream.

CoV_2O_4 was deposited onto the polished glassy carbon surfaces via dropcasting of a catalyst ink suspension. Catalyst ink suspensions were prepared by adding 80mg of the CoV_2O_4 powder into a solution of 3.8 mL H_2O, 1 mL isopropyl alcohol, and 40 µL 5 wt % Nafion 117

solution. The resulting suspension was sonicated for 30 minutes immediately prior to dropcasting. For the glassy carbon disk working electrodes, 2 x 5 µL of the catalyst ink suspension was dropcast directly onto the disk surface using a calibrated micropipette. Electrodes were allowed ten minutes to dry in an gravity oven at 60°C between additions. For the glassy carbon plate working electrode, 2 x 25 µL of the catalyst ink suspension was dropcast directly onto the disk surface using a calibrated micropipetter coating approximately 1 cm^2 of the plate. Electrodes were allowed ten minutes to dry in a gravity oven at 60 °C between additions. Electrodes were dried in a gravity oven at 60°C for 10 minutes prior to use. The mass loading of as-synthesized catalyst on the surface was the same for every electrode prepared at 0.84 mg/cm^2. V_2O_3 was deposited in an identical manner to that described above for comparative measurements of pre-activation and OER measurements

3.4.3 Material characterization of CoV_2O_4 powders and films

The phase of the as-synthesized CoV_2O_4 powder was confirmed by powder X-ray diffraction (PXRD). PXRD data was collected using a Rigaku Miniflex 600 X-ray diffractometer with a Cu Kα radiation source (40 kV/15 mA). Peak matching was performed using the Jade software with reference materials collected from the ICSD-FIZ Karlsruhe. The BET (Brunauer-Emmet-Teller) surface areas of the CoV_2O_4 material was estimated from N_2 adsorption/desorption isotherms in powder forms using a Micromeritics ASAP 2020 surface area and porosimetry analyzer. Prior to surface area measurements, the CoV_2O_4 samples heated at 150°C for 8-12 h, then immediately weighed and transferred to the sample tube for the measurement. The surface area was calculated with the Brunauer-Emmett-Teller (BET) method in the relative pressure range of 0.005 to 0.25 of adsorption data.

Transmission Electrode Microscopy (TEM) measurements of the as-synthesized CoV_2O_4 were conducted by first suspending a small amount (>1 mg) of the as-synthesized CoV_2O_4 in ~5mL isopropanol. The samples was added to a Cu TEM grid with 10 additions of ~50 µL drops of the suspension dropcast from a glass pipette. The grid was dried for 5 minutes at room temperature between each addition. The catalyst-modified TEM grid was then inserted into a JEOL 3100R05 Double Cs Corrected TEM/STEM equipped with Gatan Ultrascan 1000 CCD TV camera for image processing and a JEOL SDD X-ray detector for elemental detection. Samples were taken with an acceleration voltage of 200 kV. Images were processed using Gatan Microscopy Suite. Particle sizes were estimated through measuring the surface area of 30 unique particles. All particles were assumed to be cubic.

The metal composition of the as-synthesized CoV_2O_4 material was determined using inductively-coupled plasma—mass spectrometry (ICP-MS) and X-ray photoelectron spectroscopy (XPS). For ICP-MS measurements, 10 mg of the as-synthesized CoV_2O_4 samples were added to 10 mL of concentrated HNO_3 and the mixture was left to sit at 60°C for ~2 hr until the particle fully dissolved. This solution was diluted then used to analyze the Co and V content in the solution using a Perkin-Elmer Nexion 2000 ICP-MS. Calibration standards for cobalt (Ricca Chemical, 1000 ppm in 10% HNO_3) and vanadium (Sigma Aldrich, 1000 ppm in 10% HNO_3) were prepared by diluting the as received standard with 1M trace metal grade HNO_3 to create calibration standards at the 1, 5, 10, 20, and 50 ppm level. All samples were run against a Bi internal standard.

XPS measurements were conducted on the dropcast films on glassy carbon electrodes. The XPS spectra were acquired on a Kratos Axis Ultra XPS with a monochromatic Al x-ray source operating at 8 mA and 14 kV. High-resolution spectra were collected with a pass energy of 20 eV and a step size of 0.1 eV. The XPS peak positions were calibrated according to the sp^2 C 1s for

adventitious carbon at 284.8 eV. XPS data analysis was processed using CasaXPS version 2.3.17 (Casa Software Ltd). To quantify elemental ratios, peaks in the XPS high-resolution were fit to symmetric Voight line shapes comprised of 10% Gaussian and 90% Lorentzian functions with a Shirley background. Elemental ratios were calculated by quantifying the total peak areas in the Co $2p_{3/2}$ peak and V $2p_{3/2}$ peak and then dividing by their respective relative sensitivity factors (as tabulated for the Kratos Ultra XPS instrument).

3.4.4 Electrochemical measurements

Electrochemical measurements were conducted with a Bio-Logic SP200 or SP300 potentiostat/galvanostat. Catalyst-modified glassy carbon working electrodes were mounted into a Pine Instrument Company E6-series ChangeDisk RDE assembly and affixed to an MSR rotator (AFMSRCE, Pine Instrument Company). The reference electrode was a commercial Ag/AgCl/KCl(sat.) electrode (CH instruments) externally referenced to ferrocenecarboxylic acid in 0.2 M phosphate buffer at pH 7 (0.329 V vs $Ag/AgCl_{sat.}$) prior to each set of experiments. The auxiliary electrodes were graphitic carbon rods (99.999%, Strem Chemicals). Measurements were conducted in custom two-compartment H-cells where the working and reference electrodes were submerged in the first chamber in ~120 mL of 1 M NaOH, and the second chamber held the auxiliary electrode in ~18 mL of 1 M NaOH solution. Prior to each set of measurements, the electrolyte solution was sparged with O_2 for at least 30 min, and the solution was continuously blanketed with O_2 during rotating disk electrode voltammetry (RDEV), controlled-current electrolysis (CCE) stability measurements, and potential cycling measurements. Note that each electrochemical measurement was conducted at least three times, and reported values are averages of these runs with standard deviations as reported errors. Prior to each set of experiments, the

uncompensated solution resistance (Ru) was measured with a high-frequency single point impedance measurement at 100 kHz with a 20 mV amplitude about the open-circuit potential (OCP), and RDEV measurements were corrected for iR drop at 85% through positive feedback using the Bio-Logic ECLab software. Our typical electrochemical setup resulted in Ru ≈ 10 Ω in 1 M NaOH.

For the CCE stability measurements, CCE experiments were conducted at 10 mA/cm^2_{geo} current density for 28 h at 1600 rpm rotation rate. Throughout the measurement, the solution was continuously sparged with O_2 that was pre-saturated with H_2O by first bubbling through a gas-washing bottle filled with H_2O. The pre-saturation of the sparge gas with H_2O helped prevent evaporation of the electrolyte solution during the measurement. For the cycling stability measurements, cyclic RDEV experiments were conducted at a constant 1600 rpm rotation rate between the potential range between η = 0 V to 0.4 V at 0.1 V s^{-1}. After every 50 cycles, a slow scan rate measurement between η = 0 V to 0.4 V at 0.01 V s^{-1} followed by a 30 second static measurement at j_{geo}=10mA/cm^2. The potential from each of these static measurements were used to determine activity metrics.

In order to collect enough CoV_2O_4 sample for post-OER analysis using PXRD, it was necessary to perform stability measurements on larger surface area glassy carbon plates. Measurements were conducted in custom two-compartment H-cells where the working and reference electrodes were submerged in the first chamber in ~120 mL of 1 M NaOH, and the second chamber held the auxiliary electrode in ~18 mL of 1 M NaOH solution. The catalyst-modified glassy carbon plates were held in the working electrode chamber such that ~ 1 cm^2 of the electrode was submerged in the electrolyte. The samples were then held at a constant potential of η = 0.35 V for 28 h in a controlled-potential electrolysis (CPE) experiment.

3.4.5 Oxygen product determination

O_2 evolved during OER measurements was quantified using a Unisense Microsensor Monometer equipped with an Ox-500 oxygen probe. The probe was quantified using a three point calibration curve with N_2-sparged (0 % O_2), air-saturated (20.8 % O_2) and O_2-sparged (100 % O_2) solutions (Figure A.20). The dissolved O_2 concentration in solution at 20 °C was determined from a linear interpolation of solubility data reported at 15 and 25 °C: $[O_2]_{saturated}$ = 0.83 mM in 1 M NaOH.[15, 16] O_2 measurements were conducted in a sealed two-compartment H-cell. The first compartment was gastight and contained the glassy carbon disk working electrode, the Ag/AgCl/KCl(sat.) reference electrode, and the Ox-500 oxygen probe in a total compartment volume of 28 mL. The second compartment contained the carbon rod auxiliary electrode. The two compartment were separated by Nafion 117 membrane. Both compartments were filled with 1 M NaOH solutions, and the first compartment was filled such that there was no appreciable headspace. The solution was air-saturated prior to use, and the concentration of dissolved O_2 was monitored for 10 min at open circuit potential (OCP), followed by a controlled current electrolysis where the current density was held at 10 mA/cm^2 for 20 min passing a total charge of 2.35 C. The concentration of the dissolved O_2 was monitored in real time, and the total amount of O_2 produced was determined by determining the difference between the measured O_2 minus the background O_2 (at OCP). The Faradaic efficiency was calculated by dividing the amount of O_2 produced by the theoretical value calculated from the total charge passed.

3.4.6 Post-OER Material Characterization

Post-OER XPS analysis was conducted directly on catalyst-modified glassy carbon disks after CCE or cycling stability measurements. After the stability measurements, the electrodes were

rinsed in ultrapure water and dried in air. The dried disks were analyzed directly using XPS as described above.

Post-OER TEM-EDX measurements were measured on catalyst particles removed from glassy carbon disk electrodes. After stability measurements, the disk electrode was sonicated in isopropanol for 2 hrs to dissolve the Nafion binder and remove the catalyst. The resulting suspension of catalyst particles in isopropanol was centrifuged at 7000 rpm for 15 min at room temperature. The supernatant was decanted, and the powder was collected and dried by heating in air at 60°C. The dried powder was suspended in isopropanol and loaded onto a Cu TEM grid and analyzed using TEM-EDX as described above.

Post-OER PXRD measurements were conducted on catalyst material from the 28-h CPE measurements on catalyst-modified glassy carbon plate electrodes. After electrolysis, the catalyst-modified glassy carbon plates were sonicated in isopropanol for ~ 2 h to dissolve the Nafion binder and resulted in a suspension of catalyst particles in isopropanol. The resulting suspension of catalyst particles in isopropanol was centrifuged at 7000 rpm for 15 min at room temperature. The supernatant was decanted, and the powder was collected and dried by heating in air at 60°C. To obtain enough catalyst sample for PXRD measurements, the catalyst samples from 10 independent glassy carbon plates post-electrolysis were combined into a single PXRD sample.

Post ICP-MS measurements were conducted on catalyst material from the 28-h CPE measurements on catalyst-modified glassy carbon plate electrodes. After electrolysis, the catalyst-modified glassy carbon plates were sonicated in isopropanol for ~ 2 h to dissolve the Nafion binder and resulted in a suspension of catalyst particles in isopropanol. The resulting suspension of catalyst particles in isopropanol was centrifuged at 7000 rpm for 15 min at room temperature. The supernatant was decanted, and the powder was collected and dried by heating in air at 60°C.

Approximately 1 mg of catalyst was removed and dissolved in 10 mL HNO_3 by heating at 60°C. The solution was diluted with 1M HNO_3 and analyzed using ICP-MS as described above.

3.5 Results

3.5.1 CoV_2O_4 synthesis and characterization

CoV_2O_4 was prepared by solid state synthesis from CoO and V_2O_3 metal precursors. A 1:1 molar ratio of CoO (1 mmol, 0.075 g) and V_2O_3 (1 mmol, 0.150 g) were ground and mixed with an agate mortar and pestle, and then compressed into a pellet with a hydraulic press die at 12,000 psi applied pressure. The resulting pellet was heated under Ar to 500 °C with a heat ramp of 5 °C/min, to and then to 800 °C with a heat ramp of 5 °C/min. The pellet was held at 800 °C for 20 h under Ar Selected characterization parameters of the as-synthesized materials are summarized in Table A.6. The powder X-ray diffraction (PXRD) pattern of the as-synthesized CoV_2O_4 matches that of the CoV_2O_4 reference with minor contributions from V_2O_3 impurities as shown in Figure 3.1a. Note that V_2O_3 is not OER active (see Figure A.17), so we do not expect trace V_2O_3 impurities to affect our OER measurements. The sharp diffraction peaks suggest a highly-crystalline specimen with a large domain size which might be the product of particle agglomeration due to the high temperatures and long times in the solid-state synthesis preparation. The large grain size is supported both by transmission electron microscopy (TEM) analysis which show particles > 100 nm in size (Figure 3.1b) and the catalyst's small surface area of only 0.80 m^2/g as determined by BET gas adsorption analysis—two orders of magnitude smaller than that of Co_3O_4 (Table A.6). Elemental mapping experiments with TEM-energy dispersive X-ray analysis (TEM-EDX) show relatively uniform distribution of Co, V, and O in the as-synthesized material (Figures 3.1b).

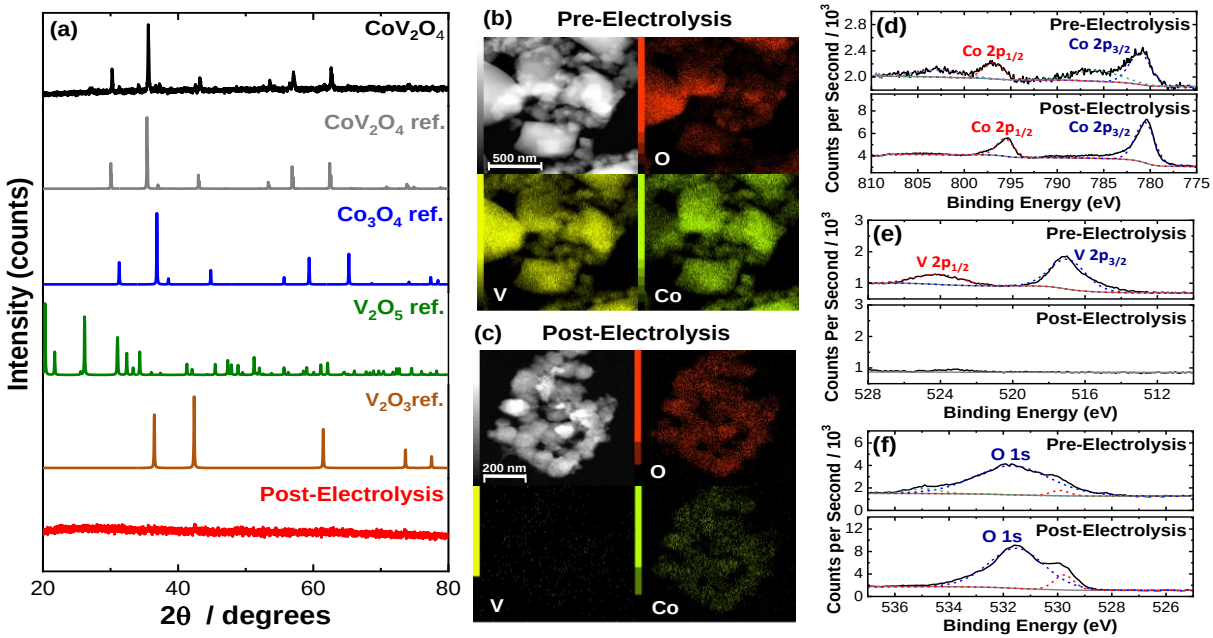

Figure 3.1(a) PXRD patterns for as-synthesized CoV_2O_4 along with reference patterns for comparison. The PXRD for CoV_2O_4 after 28-h CCE under OER conditions is also included. (b) Representative TEM images and TEM-EDX maps of as-synthesized CoV_2O_4. (c) Representative TEM images and TEM-EDX maps of CoV_2O_4 after 28-h CCE under OER conditions. (d-f) High resolution XPS spectra of CoV_2O_4 both as-synthesized and after 28-h CCE in the (d) Co 2p region, (e) V 2p region, and (f) O 1s region.

The as-synthesized CoV_2O_4 material was further characterized with X-ray photoelectron spectroscopy (XPS). XPS core scans of the as-synthesized CoV_2O_4 material in the Co 2p, V 2p, and O 1s regions are shown in Figures 3.1d-3.1f, and in the C 1s region in Figure A.18. For the Co 2p spectra of the as- synthesized material (Figure 3.1d), two peaks centered at 780.8 eV and 796.6 eV are assigned to Co $2p_{3/2}$ and Co $2p_{1/2}$ respectively, and the two shoulder peaks at 785.3 eV and 802.5 eV suggest the Co is in a CoO-like (Co^{2+}) environment.[17] For the V 2p spectra (Figure 3.1e), there is a peak at 516.5 eV assigned to V $2p_{3/2}$, which is resembles that of reported V_2O_3 samples and suggests V is in a 3+ oxidation state.[18, 19] There is a complicated O 1s peak at ~531.5 eV (Figure 3.1f) consistent with a mixed species of O on the surface (metal oxide/hydroxide/adsorbed water), but due to the convoluted nature of the peak cannot be used in V or Co oxidation state estimations.[20] The Co/V ratio based on XPS analysis was 0.58. This XPS characterization is consistent with other synthesized CoV_2O_4 materials.[5, 21]

3.5.2 Electrochemical characterization

OER activity measurements were performed using previously reported protocols.[22, 23] Catalyst inks were prepared by mixing the as-synthesized catalyst particles and Nafion in a water-isopropanol solution, and the resulting inks were dropcast onto polished glassy carbon electrode surfaces (0.196 cm^2) resulting in films with mass loadings of 0.84 mg/cm^2. The putative CoV_2O_4 catalyst shows promising activity for the OER, operating with increased activity per geometric area compared to the parent Co_3O_4 as shown in the cyclic rotating disk electrode voltammograms (RDEVs) at 1600 rpm in Figure 3.2a. When normalized for BET surface area, the activity is shown to dramatically increase compared to Co_3O_4 as shown in Figure 3.2b with the V doped catalyst being almost 300 times more active than cobalt oxide. Activity descriptors for the putative CoV_2O_4

catalyst compared to other representative OER catalysts are shown in Table A.7 showing our catalyst performs well with other similar catalytic materials. The long-term performance stability of the putative CoV_2O_4 system was confirmed by rapid potential cycling measurements and long-term controlled-current electrolysis experiments (CCE) which showed minimal change in activity over 10,000 cycles and 28 h controlled current measurements (Figure 3.2c). An in situ O_2 probe was used to quantify the oxygen production during the course of a 20-minute electrolysis. The faradaic efficiency for O_2 production was found to be 90 ± 5% confirming the OER is the largest charge contributor during this timeframe. (Figure A.20).

The activity measurements for the putative CoV_2O_4 catalyst suggest it shows remarkable stability and activity, particularly specific activity per BET surface area, for the OER. Sequential cycles of RDEVs at 1600 rpm of the putative CoV_2O_4 catalyst in 1 M NaOH are shown in Figure 3.2d. In the first cycle, there is a large oxidative feature negative of the OER electrocatalytic onset, and this oxidative feature decreases with subsequent scans before approaching a steady-state peak current after six cycles. RDEVs conducted under identical conditions for V_2O_3 show a similar oxidative feature in the first cycle that disappears in subsequent cycles (Figure A.21) Previous studies on V_2O_3 for catalysis under similar conditions report the V_2O_3 is unstable under oxidative alkaline conditions.[24] Our RDEV studies suggest that the large oxidative feature observed for CoV_2O_4 in is likely due to oxidative dissolution of V, and the steady-state redox feature after six cycles is assigned to the $Co^{2+/3+}$ redox couple of the resulting CoOx material.[25] The stability of the catalytic performance of the putative CoV_2O_4 suggests that dissolution of V has a minimal effect on the OER activity.

3.5.3 Postmortem electrode characterization

To confirm the postulated V dissolution during our experiments, we conducted a series of postmortem characterization studies on the putative CoV_2O_4 catalyst. TEM-EDX conducted on a sample after the CCE measurements show a dramatic loss of V consistent with oxidative V dissolution during electrocatalytic studies. Similarly, ICP-MS measurements taken after the CCE stability measurements show almost complete disappearance of V. XPS measurements taken after the CCE measurements show a dramatic decrease of the V 2p peaks consistent with a loss of V from the material (Figure 3.1c), and in the Co 2p region the disappearance of the shoulder peaks and the decreased FWHM of the two Co 2p peaks suggest a shift towards a Co_3O_4 like surrounding (Figure 3.1d).[26] The reduced shoulder peak of O 1s (531.5 eV), which is attributed to oxide defect sites or hydroxyl groups,[27] in the post-CCE XPS suggests the loss of defect sites and surface oxyhydroxyl (MOOH) groups while the loss at 535 eV represents the loss of H_2O species. The changes in the Co 2p and O 1s shoulder peaks suggest surface rearrangement after V dissolution which may be responsible for the increased OER activity. Note that the XPS measured on the post-cycling samples were analogous to those for the post-CCE materials (Figure A.24). PXRD measurements of the post-CCE catalyst material show an absence of defined peaks, consistent with an amorphous material (Figure 3.1). Crystallinity as determined by TEM-SAD is also shown to drastically decrease from a well-ordered crystal lattice before electrolysis, to a disordered phase after electrolysis evident by the rings in the SAD (Figure A.22). The ring structure observed was found to not correlate specifically to a single cobalt based material, suggesting formation of a mixed phased system, likely consisting of various cobalt based oxides.

3.6 Discussion

The electrochemical and post-CCE characterization data suggest that the active OER catalyst is not CoV_2O_4, but instead an amorphous, vanadium free, CoO_x material. We postulate

that the CoV_2O_4 material undergoes a structural rearrangement under electrocatalytic conditions forming a soluble VO_x phase, possibly V_2O_5, consistent with the Pourbaix diagram for V.[28-30] Upon dissolution of VO_x, the CoV_2O_4 lattice collapses resulting in an amorphous CoO_x material that is presumed to be the active species for the OER. This process is qualitatively similar to electrochemical dealloying previously used to make porous battery materials and electrocatalysts.[31-35] We postulate that the increased observed activity for our catalyst compared to Co_3O_4 may be due in part to an increased surface area after V-dissolution, but we were not able to experimentally determine this due to our inability to harvest sufficient amounts of material post-OER for BET gas adsorption measurements. Electrochemical surface area measurements from estimated double-layer capacitance was not used here due to the well-documented fallibility of that approach in determining the surface area of metal oxide OER catalysts.[23, 36-39] We did estimate an average particle size based on TEM images (Figure 3.1c and d) and we did observe a decrease in the average particle size post-CCE which is qualitatively consistent with our postulated increase in surface area assuming no material loss. However, the measured decrease in average particle size does not account for any changes in porosity or mass-loss from V dissolution that would also influence the overall surface area, and so it is reported here only as a qualitative metric.

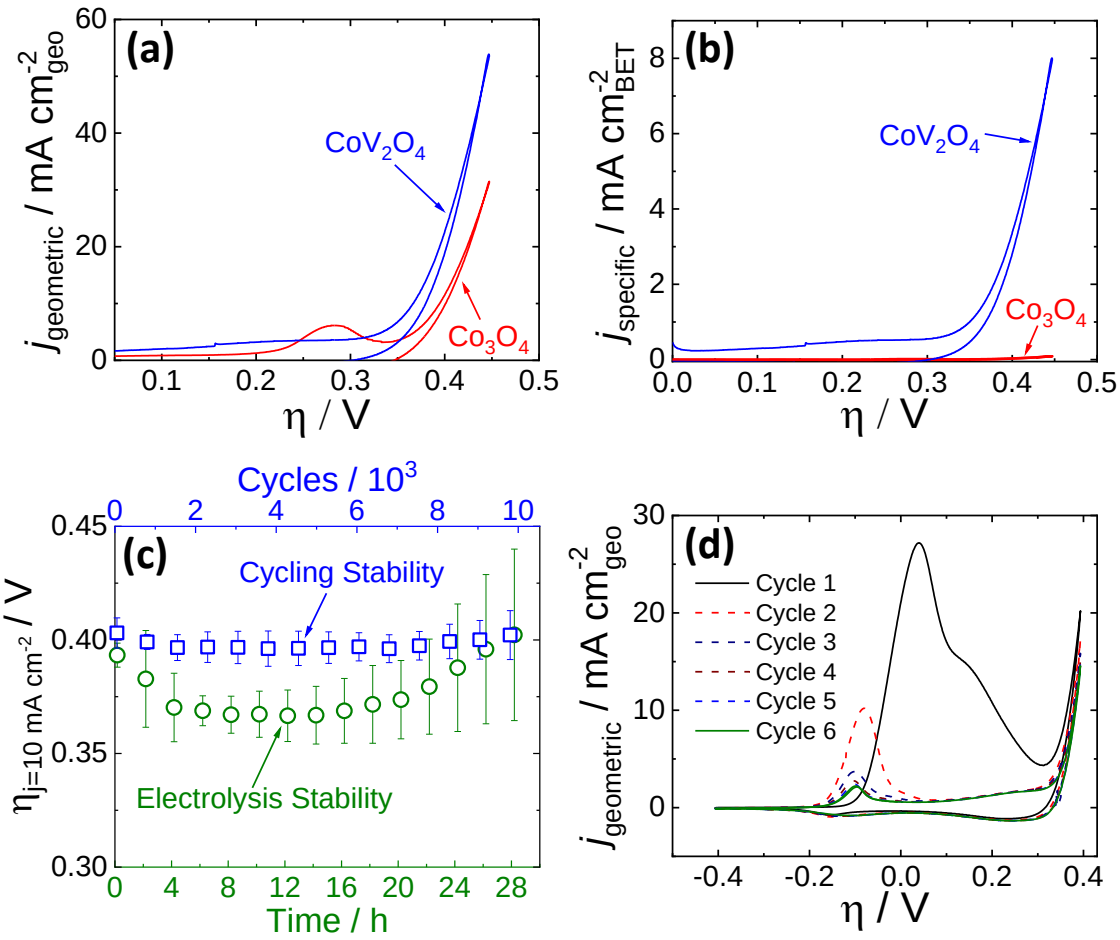

Figure 3.2. Cyclic RDEVs of the as-synthesized CoV_2O_4 catalyst compared to previously reported Co_3O_4 in O_2-saturated 1 M NaOH showing (a) the current density per geometric area and (b) the specific current density per the BET surface area of the as-synthesized materials at a scan rate of 0.01 V/s and 1600 rpm rotation rate. The RDEVs shown are the 2nd cycle for each sample. The Co_3O_4 data is taken from Ref. 20. (c) Stability studies for the putative CoV_2O_4 during OER. The green circles are measured overpotentials at 10 mA/cm^2 geometric ($\eta_{j=10\ mA/cm2}$) during 28-h CCE measurements plotted vs the polarization time on the bottom axis. The blue squares are the $\eta_{j=10\ mA/cm2}$ values during 10,000 cycle experiments plotted vs the number of cycles on the top x-axis. The 10,000 cycle experiment lasts ca. 28 h, and the bottom axis also reflects the time points in the cycling measurements. The $\eta_{j=10\ mA/cm2}$ values were average measurements from at least three independently-prepared samples, and the error bars represent the standard deviations. (d) The first six RDEVs measured for the as-synthesized CoV_2O_4. There is a large pre-catalytic peak at $\eta \approx 0.05$ V that shifts negative and decreases in intensity in subsequent scans.

This is qualitatively similar to observations within the vanadium battery literature. It has been noted that the dissolution of vanadium based cathode materials for batteries leads to a decreased capacitance, suggested to be in part due to increased resistance within the cell.[40] Due to these observations, there have been multiple studies over the last five years looking into methods to hinder the dissolution process for vanadium cathodes within the battery literature.[41, 42] However, in the electrochemical catalysis literature, vanadium catalysts dissolution is often not discussed, despite these materials being shown to activate catalytic pathways such as the oxygen evolution reaction.

Previous studies have reported that V-doped Co oxide materials show higher activity for the OER than their parent oxide materials.[5-13] In many cases, this observed higher OER activity compared to the V-free parent materials is attributed to specific changes in the physical structure and/or electronic structure upon V incorporation resulting in changes to material conductivity, adsorption energy of OER intermediates, and/or the rate determining step in the catalytic mechanism. These mechanistic arguments are often motivated by detailed experimental and computational analysis, and all are based on the continued presence of V in the material structure during the OER. In the case of V-doped amorphous CoO_x films,[7, 9] crystalline V-doped CoOOH[8] and CoFe-based[12] nanoparticles, and Co-V hydroxide nanostructures,[13] postmortem characterization shows these materials retain significant concentrations of V after OER stability measurements, consistent with the assertion that the continued presence of V is an important component of the OER mechanism for these materials.[7, 8, 12, 13]

However, in previous studies of crystalline V-doped Co_3O_4-based spinel materials, a lack of postmortem characterization introduces ambiguity as to the role of V in the catalytic mechanism. For example, in previous studies of OER by $CoV_{2-x}Fe_xO_4$ and $Co_{3-x}V_xO_4$ nanoparticles,

comprehensive mechanistic analysis was conducted with the assumption that V was an important component in the active catalyst species.[5, 6] However, in these studies either postmortem analysis was not reported to confirm the presence of V in the material after the OER,[6] or reported postmortem characterization showing the loss of V during the OER was not considered in the mechanistic analysis.[5] Similarly, studies of V-doped CoP materials and Co-Mo-V catalysts both attribute increased catalytic activity to the presence of V in the materials, but did not include postmortem characterization showing the continued presence of V after the OER.[10, 14] This is not to say that the mechanistic arguments in these previous studies are incorrect, but rather suggests that the composition of the post-OER catalyst should be reported and discussed when considering possible catalytic mechanisms.

3.7 Conclusion

V-doped Co oxide materials are an emerging class of promising electrocatalysts for the OER. In our work, we show that a putative CoV_2O_4 spinel catalyst shows remarkable specific activity based on as-synthesized catalyst characterization when compared to Co_3O_4 and other reported OER catalysts. However, postmortem characterization shows dissolution of V from the material resulting in lattice collapse and the formation of amorphous CoO_x particles, the presumed true active catalysts for the OER. Our findings introduce uncertainty into the mechanistic arguments made in previous studies of V-doped Co_3O_4-based spinel materials for the OER that suggest V plays an important role in catalytic mechanism without considering postmortem materials characterization to confirm the continued presence of V during the OER. Conducting compositional and structural characterization of OER materials after electrocatalytic stability studies is recommended as a minimum requirement in assigning plausible catalytic active species according to recent reviews of best practices for OER measurements.[38, 39, 43, 44] We believe our

work serves as a case study highlighting the importance of postmortem characterization in determining possible catalytic species prior to in-depth mechanistic analysis.

3.8 References

1. W. T. Hong, M. Risch, K. A. Stoerzinger, A. Grimaud, J. Suntivich and Y. Shao-Horn, *Energy & Environmental Science*, 2015, **8**, 1404-1427.
2. L. Han, S. Dong and E. Wang, *Adv. Mater.*, 2016, **28**, 9266-9291.
3. N.-T. Suen, S.-F. Hung, Q. Quan, N. Zhang, Y.-J. Xu and H. M. Chen, *Chemical Society Reviews*, 2017, **46**, 337-365.
4. W.-J. Jiang, T. Tang, Y. Zhang and J.-S. Hu, *Acc. Chem. Res.*, 2020, **53**, 1111-1123.
5. R. Wei, X. Bu, W. Gao, R. A. B. Villaos, G. Macam, Z.-Q. Huang, C. Lan, F.-C. Chuang, Y. Qu and J. C. Ho, *ACS Applied Materials & Interfaces*, 2019, **11**, 33012-33021.
6. K. Chakrapani, G. Bendt, H. Hajiyani, T. Lunkenbein, M. T. Greiner, L. Masliuk, S. Salamon, J. Landers, R. Schlögl, H. Wende, R. Pentcheva, S. Schulz and M. Behrens, *ACS Catal.*, 2018, **8**, 1259-1267.
7. L. Liardet and X. Hu, *ACS Catal.*, 2018, **8**, 644-650.
8. Y. Cui, Y. Xue, R. Zhang, J. Zhang, X. a. Li and X. Zhu, *Journal of Materials Chemistry A*, 2019, **7**, 21911-21917.
9. G. Merle, I. Abrahams and J. Barralet, *Mater. Today Energy*, 2018, **9**, 247-253.
10. J.-F. Qin, J.-H. Lin, T.-S. Chen, D.-P. Liu, J.-Y. Xie, B.-Y. Guo, L. Wang, Y.-M. Chai and B. Dong, *J. Energy Chem.*, 2019, **39**, 182-187.
11. J. M. Gonçalves, M. Ireno da Silva, L. Angnes and K. Araki, *J. Mater. Chem. A*, 2020, **8**, 2171-2206.
12. T. Gao, Z. Jin, M. Liao, J. Xiao, H. Yuan and D. Xiao, *J. Mater. Chem. A*, 2015, **3**, 17763-17770.
13. M. Yang, X. Fu, M. Shao, Z. Wang, L. Cao, S. Gu, M. Li, H. Cheng, Y. Li, H. Pan and Z. Lu, *ChemElectroChem*, 2019, **6**, 2050-2055.
14. J. Bao, Z. Wang, J. Xie, L. Xu, F. Lei, M. Guan, Y. Zhao, Y. Huang and H. Li, *Chem. Commun.*, 2019, **55**, 3521-3524.
15. W. F. Linke, *Solubilities: Inorganic and Metal-Organic Compounds*, American Chemical Society, Washington, D.C., 4th edn., 1965.
16. R. Battino, *J. Phys. Chem. Ref. Data*, 1983, **12**, 163-178.
17. P. W. Menezes, A. Indra, D. González-Flores, N. R. Sahraie, I. Zaharieva, M. Schwarze, P. Strasser, H. Dau and M. Driess, *ACS Catalysis*, 2015, **5**, 2017-2027.
18. N. K. Nag and F. E. Massoth, *J. Catal.*, 1990, **124**, 127-132.
19. B. S. Allimi, S. P. Alpay, D. Goberman, T. Huang, J. I. Budnick, D. M. Pease and A. I. Frenkel, *Journal of Materials Research*, 2007, **22**, 2825-2831.
20. G. Silversmit, D. Depla, H. Poelman, G. B. Marin and R. De Gryse, *J. Electron. Spectrosc. Relat. Phenom.*, 2004, **135**, 167-175.
21. J. S. Lu, I. V. B. Maggay and W. R. Liu, *Chem. Commun.*, 2018, **54**, 3094-3097.
22. C.-C. Lin and C. C. L. McCrory, *ACS Catal.*, 2017, **7**, 443-451.

23. S. Jung, C. C. L. McCrory, I. M. Ferrer, J. C. Peters and T. F. Jaramillo, *Journal of Materials Chemistry A*, 2016, **4**, 3068-3076.
24. F. M. Al-Kharafi and W. A. Badawy, *Electrochim. Acta*, 1997, **42**, 579-586.
25. M. S. Burke, M. G. Kast, L. Trotochaud, A. M. Smith and S. W. Boettcher, *J. Am. Chem. Soc.*, 2015, **137**, 3638-3648.
26. S. C. Petitto, E. M. Marsh, G. A. Carson and M. A. Langell, *J. Mol. Catal. A: Chem.*, 2008, **281**, 49-58.
27. J. Wei, Y. Y. Feng, Y. Liu and Y. Ding, *J. Mater. Chem. A*, 2015, **3**, 22300-22310.
28. K. Post and R. G. Robins, *Electrochim. Acta*, 1976, **21**, 401-405.
29. M. Pourbaix, *Atlas of Electrochemical Equilibria in Aqueous Solution*, Pergamon Press, Oxford, 1966.
30. I. Povar, O. Spinu, I. Zinicovscaia, B. Pintilie and S. Ubaldini, *J. Electrochem. Sci. Eng.*, 2019, **9**, 75-84.
31. J. Erlebacher, M. J. Aziz, A. Karma, N. Dimitrov and K. Sieradzki, *Nature*, 2001, **410**, 450-453.
32. S. Koh and P. Strasser, *J. Am. Chem. Soc.*, 2007, **129**, 12624-12625.
33. Z. Zhang, Y. Wang, Z. Qi, W. Zhang, J. Qin and J. Frenzel, *J. Phys. Chem. C*, 2009, **113**, 12629-12636.
34. X. Lu, M. Ahmadi, F. J. DiSalvo and H. D. Abruña, *ACS Catal.*, 2020, **10**, 5891-5898.
35. A. Pavlišič, P. Jovanovič, V. S. Šelih, M. Šala, M. Bele, G. Dražić, I. Arčon, S. Hočevar, A. Kokalj, N. Hodnik and M. Gaberšček, *ACS Catal.*, 2016, **6**, 5530-5534.
36. R. L. Doyle, I. J. Godwin, M. P. Brandon and M. E. G. Lyons, *Physical Chemistry Chemical Physics*, 2013, **15**, 13737-13783.
37. K. Klingan, F. Ringleb, I. Zaharieva, J. Heidkamp, P. Chernev, D. Gonzalez-Flores, M. Risch, A. Fischer and H. Dau, *ChemSusChem*, 2014, **7**, 1301-1310.
38. M. B. Stevens, L. J. Enman, A. S. Batchellor, M. R. Cosby, A. E. Vise, C. D. M. Trang and S. W. Boettcher, *Chem. Mater.*, 2017, **29**, 120-140.
39. C. Wei, R. R. Rao, J. Peng, B. Huang, I. E. L. Stephens, M. Risch, Z. J. Xu and Y. Shao-Horn, *Adv. Mater.*, 2019, **31**, 1806296.
40. M. J. Root, *Journal of The Electrochemical Society*, 2011, **158**, A1347.
41. S. Luo, X. Cao, Q. Su, Y. Zhang, S. Liu, X. Xie, S. Liang and A. Pan, *ACS Applied Energy Materials*, 2021, **4**, 6197-6204.
42. Y. Liu, Y. Jiang, Z. Hu, J. Peng, W. Lai, D. Wu, S. Zuo, J. Zhang, B. Chen, Z. Dai, Y. Yang, Y. Huang, W. Zhang, W. Zhao, W. Zhang, L. Wang and S. Chou, *Advanced Functional Materials*, 2021, **31**, 2008033.
43. R. Frydendal, E. A. Paoli, B. P. Knudsen, B. Wickman, P. Malacrida, I. E. L. Stephens and I. Chorkendorff, *ChemElectroChem*, 2014, **1**, 2075-2081.
44. S. Geiger, O. Kasian, M. Ledendecker, E. Pizzutilo, A. M. Mingers, W. T. Fu, O. Diaz-Morales, Z. Li, T. Oellers, L. Fruchter, A. Ludwig, K. J. J. Mayrhofer, M. T. M. Koper and S. Cherevko, *Nat. Catal.*, 2018, **1**, 508-515.

Chapter 4 Electrochemical Alcohol Oxidation using a Co_2NiO_4 Catalyst: How Variations in Alcohol Identity and Electrochemical Bias Alter Product Selectivity

4.1 Preface

This chapter discusses a Co_2NiO_4 catalyst which shows remarkable activity for alcohol oxidation. This material shows activity for alcohol oxidation for a wide range of aliphatic alcohols into both aldehyde and carboxylic acid products, with varying ranges of product selectivity. The potential dependence of this product selectivity is them observed using n-butanol as a test alcohol, showing how alteration in the energy applied to the system changes both the product selectivity in alcohol oxidation, as well as the reaction selectivity between the OER and the AOR. This work is part of a manuscript in preparation of which I am the primary author responsible for material synthesis, method development, electrochemical measurements, material analysis, and manuscript preparation. Author two was responsible for assisting with electrolysis data. My advisor Dr. Charles C. L. McCrory was responsible for assisting with manuscript preparation.

4.2 Abstract

Electrochemical oxidation of organic alcohols through the alcohol oxidation reaction (AOR) offers the ability to produce an alternative product at the anode rather than producing oxygen or chlorine gas in aqueous conditions. Here we study the activity and product selectivity using a Co_2NiO_4 catalyst that shows moderate activity for the Oxygen Evolution Reaction with an overpotential of 0.39 V however shows a dramatic increase in activity upon addition of straight chain alcohols to the solution (n=1-5), with the system reaching a current density of 10 mA/cm^2 at

roughly 1.42V vs RHE for all alcohols. The product selectivity for this system is shown to favor aldehyde formation for shorter chain alcohol and carboxylic acid production for longer chain alcohols. Additionally, we report the potential dependence of the AOR for this catalyst system showing the presence of both aldehyde and carboxylic acid products at all potentials in the range of 1.4V to 1.7V vs RHE. The system is also able to outcompete chloride oxidation with charge efficiencies for AOR reaching >90% FE in solutions containing 1M NaCl with comparable charge and charge efficiencies between both chlorinated and non chlorinated systems.

4.3 Introduction

One of the most promising strategies to overcome the intermittency limitations of renewable solar and wind electricity production is to store renewable energy on-cycle in the form of chemical fuels—e.g. solar fuels.[1-7] In particular, recent technoeconomic studies suggest that coupling renewable electricity to the efficient electrochemical production of H_2 from H_2O or C-based fuels from CO_2 may be economically viable strategies for storing renewable electricity.[8-10] However, one of the larger challenges solar fuels is the sluggish kinetics of the oxygen evolution reaction (OER). In electrochemical reactors, the electrochemical reduction of H_2O to H_2 or CO_2 to C-containing products at the cathode is coupled to the oxygen evolution reaction (OER) at the anode, and the sluggish electrode kinetics of the OER limit the maximum current densities which can be achieved at the cathode.[11-17] One possible alternative to the OER is the alcohol oxidation reaction (AOR), which has been shown in some studies to achieve higher current densities at less positive applied potentials compared to the OER.[18-22] In addition, the large number of possible alcohol substrates, including everything from straight-chain alcohols[23-27] to biomass-derived products,[9, 28-36] increase the likelihood that the AOR will produce chemicals that can be further processed into value-added chemical feedstocks.

Cobalt-based materials have shown particular promise as active catalysts for the AOR.[29, 37-42] Ni-doped cobalt oxide (Co_2NiO_4) has been reported as a particularly highly active for alcohol oxidation that is much more active than its Co_3O_4 and NiO parent materials.[43, 44] The reason for the increased AOR activity for Co_2NiO_4 compared to Co_3O_4 and NiO has been attributed to its increased material conductivity[45] and a positive shift in the $Co^{3+/4+}$ redox couple that aligns better with the onset of the AOR.[46] Specifically, Co_2NiO_4 has been shown to operate with high activity for CH_3OH oxidation, achieving current densities $\geq$ 10 mA cm^{-2} at ~1.4 V vs RHE, approximately 0.2 V less positive than the onset of OER.[44, 47, 48] Co_2NiO_4 has also shown promise as an electrocatalyst for the oxidation of 5-hydroxymehtyl furfural (HMF), a bioremediation product, to furandicarboxylic acid (FDCA), a useful polymerization feedstock.[49-51]

While previous studies of AOR at Co_2NiO_4 electrocatalysts highlight the versatility of this catalyst material, these studies have not necessarily quantified the potential-dependence of product distribution. Most AOR studies at Co_2NiO_4 electrocatalysts either focus primarily on measured current densities and do not quantify product identities or amounts,[44, 47, 48] or quantify products at only single or a few applied potentials.[49-51] The few studies that explore potential dependence for the AOR at Co_2NiO_4 show changes in product selectivity as a function of applied potential,[46] suggesting a complicated interrelationship between potential and the reaction mechanism and kinetics. Although previous studies of the AOR at Co_2NiO_4 have been very informative as to the catalytic nature of Co_2NiO_4, the lack of product analysis, and particularly potential-dependent product analysis, hinders deeper understanding reaction and product selectivity, and possible mechanistic and kinetic pathways for the AOR. In general, the dearth of studies investigating potential-dependent AOR product analysis at Co_2NiO_4 electrocatalysts

hinders our understanding of possible mechanistic pathways and electrocatalytic kinetics under relevant reaction conditions. This general dearth of potential-dependent product analysis in the AOR is not unique to the Co_2NiO_4 system, but applies more broadly to most studies of the AOR for numerous alcohols at various catalysts,[32, 34, 52-56] with a few important exceptions.[46, 57-59]

In this study, we report the activity and product distribution of the electrochemical oxidation of C1-C5 aliphatic primary alcohols at phase-pure Co_2NiO_4 electrocatalysts in alkaline electrolytes (Figure 4.1). We show that Co_2NiO_4 is a competent electrocatalyst for all alcohols investigated, oxidizing each with high activity with a catalytic onset near the putative $Co^{3+/2+}$ couple of the material near 1.4 V vs RHE, ~0.2 V less positive than the onset of the OER at this catalyst. We also show that after controlled potential electrolyses at a given potential of 1.55 V vs RHE, the major AOR products detected change as a function of the size of the alcohol, switching from ~45% Faradaic efficiency for the 2-e^- aldehyde oxidation product of ethanol (EtOH) to > 75% Faradaic efficiency for the 4-e^- carboxylic acid oxidation product of *n*-pentanol (*n*-PnOH). This result suggest that the AOR for aliphatic primary alcohols at Co_2NiO_4 catalysts may operate via a cascade (or domino) catalysis mechanism, where the alcohol is oxidized sequentially first to the aldehyde, and then to the carboxylic acid as the final product. Importantly, attempts to conduct the oxidation of *n*-BuOH at an electrodeposited $CoNiO_x$ film were unsuccessful, suggesting that the structure of Co_2NiO_4 electrocatalyst is critical to its activity for the AOR.

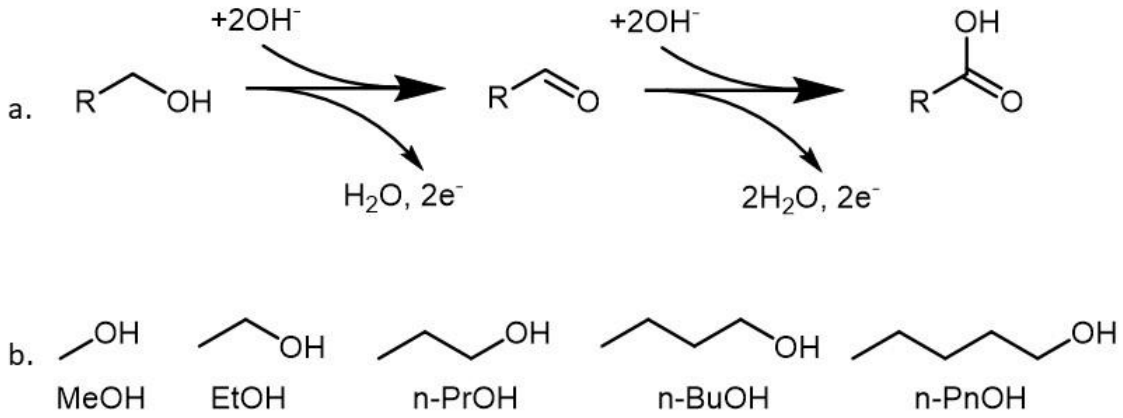

Figure 4.1 Reaction for the electrochemical alcohol oxidation on a general alcohol showing the aldehyde and carbocyclic acid products that can be formed.

We also analyzed the product distribution on *n*-BuOH after a series of controlled potential electrolyses at different applied potentials. At potentials more positive than the onset of the AOR but less positive than the onset of the OER (e.g. between 1.45 and 1.60 V vs RHE), the product distribution of the alcohol oxidation is equivalent at every potential. At potentials more positive of the OER onset, the fractional charge going towards the AOR remains relatively constant, but the overall Faradaic efficiency decreases due to the onset of the OER reaction. These results suggest that the kinetics of *n*-BuOH is similar at every potential at Co_2NiO_4 catalysts, and that the OER and AOR are non-competitive parallel processes—the onset of the OER does not inhibit the rate of the AOR.

Finally, we show that the presence of 1.0 M NaCl in alkaline solution does not inhibit the activity or product selectivity of Co_2NiO_4 electrocatalysts for the AOR. 1.0 M NaCl solutions contain approximately double the concentration of Cl^- found in seawater.[60, 61] This result suggests that the AOR at Co_2NiO_4 is compatible with the use of basified seawater as the electrolyte, an important consideration for sustainable solar fuels production.[62-64] Overall, these studies indicate that the AOR at Co_2NiO_4 electrocatalysts is a promising alternative to the OER for solar fuels

production, requiring less-positive operating potentials at the anode and possibly producing additional value-added chemical feedstocks in solar fuels devices.

4.4 Experimental

4.4.1 Materials

Unless otherwise noted, all commercial chemicals were used as received without further purification. 1-Butanol (*n*-BuOH, ACS 99.4+%), 1-pentanol (*n*-PnOH, 98+%), 1-propanol (*n*-PrOH, ACS 99.5+%), acetic acid (CH_3COOH, TM 99.5), Valeric Acid ($CH_2CH_2CH_2CH_2CH_2COOH$, ACS 99%), cobalt(II) acetate tetrahydrate ($Co(OAc)_2{\cdot}4\ H_2O$, 98%), nickel(II) nitrate hexahydrate ($Ni(NO_3)_2{\cdot}6\ H_2O$, 98.5%), nitric acid (HNO_3, Trace Metal), oxalic acid dihydrate (ACS, 99.5+%), sodium hydroxide (NaOH, 98.5%), and sulfuric acid (H_2SO_4, Optima) were purchased from Thermo Fisher Scientific. 2-Propanol (*i*-PrOH, ACS 99.5+%), methanol (MeOH, HPLC 99.9+%), formic Acid (HCOOH, ACS >96%), formaldehyde (HCHO, 37%), acetaldehyde (CH_3CHO, ACS >99.5%), propionic acid (CH_3CH_2COOH, ACS 99.5%), propionaldehyde (CH_3CH_2COOH, 97%), butyric acid ($CH_2CH_2CH_2COOH$, ACS 99%), buteraldehyde ($CH_2CH_2CH_2COH$, ACS >96%), valeraldehyde ($CH_2CH_2CH_2CH_2COOH$, ACS 97%), ferrocenecarboxylic acid (C11H10FeO2, 97%), sodium phosphate monobasic dihydrate ($NaH_2PO_4{\cdot}2\ H_2O$, ACS) and 5 wt % Nafion 117 solution (in a mixture of lower aliphatic alcohols and water) were purchased from Millipore Sigma. Ethanol (EtOH, 200 proof, anhydrous) was purchased from Decon Labs, Inc., and used without further purification. Solid Nafion 117 membranes were purchased from the Fuel Cell Store. Nickel and cobalt ICP standards (1000 ppm in 3% HNO_3) were purchased from Ricca Chemical Company. All water used in this study was ultrapure water (18.2 MΩ cm resistivity) purified using a Thermo

Scientific Barnstead™ Nanopure water purification system. Argon () was purchased from Cryogenic Gas. All nitrogen used was boil-off gas from a liquid nitrogen source.

4.4.2 Co_2NiO_4 synthesis and deposition

Co_3O_4 was prepared according to a previously reported synthesis.[65] $Co_2Ni_2O_4$ was synthesized according to a modified literature procedure involving the thermal decomposition of oxalate gel precursors.[65] In a typical synthesis, 0.2 mmol of $Co(OAc)_2 \cdot 4\ H_2O$ and 0.01 mmol of $Ni(NO_3)_2 \cdot 6\ H_2O$ were dissolved in 40 mL EtOH and stirred at 50 °C for 30 min. 10 mL of a prepared 1.8 M oxalic acid solution in EtOH was added dropwise to the previous solution. After the addition of the oxalic acid solution the mixture was stirred at 50° C for 2 h. The solvent then was removed by vacuum, and the remaining pink gel was added to a 400 °C oven for 2 hr. The resulting black $Co_2Ni_2O_4$ powder was ground manually with mortar and pestle prior to analysis and use.

Working electrodes were either 5 mm diameter glassy carbon disks (4 mm thick, 0.196 cm^2 surface area, Sigradur G, HTW Hochtemperatur-Werkstoffe GmbH) or 1.6 cm × 3.2 cm glassy carbon plates (0.1 mm thick, 5.1 cm2 surface area, HTW Hochtemperatur-Werkstoffe GmbH). The glassy carbon disks were sonicated sequentially in water, isopropanol, and then water for 1 minute, and then lapped with silicon carbide abrasive papers (CarbiMet 2, 600/P1200, Buehler). Following a sonication in 1M nitric acid for 30 minutes, and then water for 1 minute, the electrodes were polished sequentially with diamond abrasive slurries (MetaDi Supreme, Buehler) in an order of 9 µm, 6 µm, 3 µm, 1 µm on synthetic nap based polishing pads (MD Floc, Struers). Between each polishing step, the electrodes were sonicated for ~30 s in *i*-PrOH. The lapping and polishing were performed using a Struers LaboPol-5 polisher with a LaboForce-1 specimen mover. The disks were held in the LaboForce-1 specimen mover with 5

psi of applied pressure per disk, and during lapping and polishing the platen speed was held at 200 rpm and the head speed at 8 rpm in the opposite rotation direction from the platen. After the final polishing step, the glassy carbon disks were sonicated in aqueous 1 M HNO_3 for 10 min, followed by sequential 3 min sonication steps in acetone and ultrapure water, and then dried in an N_2 stream.

Co_2NiO_4 was deposited onto the polished glassy carbon surfaces via dropcasting of a catalyst ink suspension as previously described.[65, 66] Briefly, catalyst ink suspensions were prepared by adding 80 mg of the Co_2NiO_4 powder into a solution of 3.8 mL H_2O, 1 mL *i*-PrOH, and 40 µL of 5 wt % Nafion 117 solution added in that order. Immediately prior to dropcasting, the suspension was sonicated for 30 minutes to disperse the Co_2NiO_4 powder. The Co_2NiO_4 suspension was dropcast onto the polished glassy carbon surface through 2 sequential additions of 5 µL each using a calibrated micropipetter, with continued sonication of the ink solution between additions. Electrodes were dried for 10 min in air at 60 °C after each addition. The mass loading of the as-synthesized catalyst on the surface was 0.84 mg cm^{-2}, and was the same for every electrode prepared. Co_3O_4-modified electrodes were prepared using the same procedure.

Electrodeposited Co/Ni was prepared on polished glassy carbon disk electrodes as described previously.[67] 1.05g $Ni(NO_3)_2$ 6 H_2O, and 0.12g $Co(NO_3)_2$6 H_2O (Thermo fisher, 97.7%) were dissolved in 40mL of water. Glassy carbon disk electrodes were dropped into the solution and rotated at 1200 rpm. An applied current density of -16mA cm^{-2} was used for 10s and the electrode was removed. The resulting electrode was rinsed with water and dried under N_2.

4.4.3 Characterization of the As-Synthesized Materials

The $CoNi_2O_4$ powder phase was confirmed by powder X-ray diffraction (PXRD). PXRD data was collected using a Rigaku Miniflex 600 X-ray diffractometer with a Cu Kα radiation source (40 kV/15 mA). Reference materials were collected from the ICSD-FIZ Karlsruhe and peak matching was performed using the Jade software. The BET (Brunauer-Emmet-Teller) surface areas of the Co_2NiO_4 material were estimated from N_2 adsorption/desorption isotherms of the $CoNi_2O_4$ powder measured using a Micromeritics ASAP 2020 surface area and porosimetry analyzer. The Co_2NiO_4 samples were heated at 150°C for 8-12 h to remove impurities, then immediately weighed and transferred to the sample tube for the measurement. The surface area was calculated with the Brunauer-Emmett-Teller (BET) method in the relative pressure range of 0.005 to 0.25 of adsorption data.

The metal composition of the as-synthesized Co_2NiO_4 material was determined using inductively coupled plasma—mass spectrometry (ICP-MS) and X-ray photoelectron spectroscopy (XPS). For ICP-MS measurements, 5 mg of the as-synthesized Co_2NiO_4 powder was added to 10 mL of aqueous 1.0 M trace-metal grade HNO_3 and heated at 70 °C for 12 h to ensure the metal particles were fully dissolved. The resulting solution was diluted by a factor of 1000 to reach metal ion concentrations in the 100 ppb range. The Co and Ni content in the solution was determined using a Perkin-Elmer Nexion 2000 ICP-MS. Calibration standards for Co and Ni were prepared by diluting the as-received standards with 1 M HNO_3 to create calibration standards at the 10, 20, 50, 100, 200 and 50 ppm level. All samples were run against a Bi internal standard.

Scanning electron microscopy—energy dispersive X-ray spectroscopy (SEM-EDS) measurements were conducted directly on the dropcast films on the glassy carbon electrodes using a JEOL-7800FLV FE SEM operating at 20 kV accelerating voltage equipped with an

energy dispersive X-ray detector. X-ray photoelectron spectroscopy (XPS) measurements were conducted directly on the dropcast films on the glassy carbon electrodes. The XPS spectra were acquired using a Kratos Axis Ultra XPS with a monochromatic Al x-ray source operating at 8 mA and 14 kV. High-resolution spectra were collected with a pass energy of 20 eV and a step size of 0.1 eV. The XPS peak positions were calibrated according to the sp^2 C 1s peak from adventitious carbon centered at 284.8 eV. XPS data analysis was processed using CasaXPS version 2.3.17 (Casa Software Ltd). Peaks in the XPS high-resolution were fit to symmetric Voight line shapes comprised of 10% Gaussian and 90% Lorentzian functions with a Shirley background. Elemental ratios were calculated by quantifying the total peak areas in the Co $2p_{3/2}$ peak and Ni $2p_{3/2}$ peak and then dividing by their respective relative sensitivity factors specific to the Kratos Ultra XPS instrument.

4.4.4 Electrochemical measurements and Product Analysis

Electrochemical measurements were conducted with a Bio-Logic SP200 or SP300 potentiostat/galvanostat. Reference electrodes were commercial Ag/AgCl/KCl(sat.) electrodes (CH instruments) that were externally referenced to ferrocenecarboxylic acid in 0.2 M phosphate buffer at pH 7 (0.329 V vs $Ag/AgCl_{sat}$) prior to each set of experiments. Auxiliary electrodes were graphitic carbon rods (99.999%, Strem Chemicals). Electrolyte solutions used for oxygen evolution reaction (OER) experiments contained 1 M NaOH in water, and electrolyte solutions used for alcohol oxidation experiments (AOR) contained 1 M NaOH and 100 mM of alcohol (MeOH, EtOH, *n*-PrOH, *n*-BuOH, or *n*-PnOH) in water. For example, to prepare an electrolyte solution for an *n*-BuOH oxidation experiment, ~15 mL of 1 M NaOH was added to a 25 mL volumetric flask, followed by addition of 183 µL of *n*-BuOH. The flask was then filled to the volume line with 1 M NaOH and mixed vigorously to ensure dissolution of the *n*-BuOH.

For RDE experiments, catalyst-modified glassy carbon working electrodes were mounted into a Pine Instrument Company E6-series ChangeDisk RDE assembly and affixed to an MSR rotator (AFMSRCE, Pine Instrument Company). All RDE experiments were conducted in a custom two-compartment H-cell comprised of a working chamber in which the working electrode and reference electrode were submerged in 10 mL of electrolyte solution, and an auxiliary chamber in which the auxiliary electrode was submerged in 5 mL of electrolyte solution (Figure A.29). The two compartments were separated using a Nafion 117 membrane. The electrolyte was exposed to air throughout the RDE experiments, and the electrode was rotated at a rotation rate of 1600 rpm to ensure steady-state mass transport at the electrode surface and to aid in bubble removal in the OER potential regime. Prior to each set of experiments, the uncompensated solution resistance (Ru) was measured with a high-frequency single point impedance measurement at 100 kHz with a 20 mV amplitude about the open-circuit potential (OCP), and electrochemical RDE measurements were corrected for iR drop at 85% through positive feedback using the Bio-Logic ECLab software. Our typical electrochemical setup resulted in Ru ≈ 10 Ω in 1 M NaOH. RDE cyclic voltammograms (RDEVs) were collected by scanning from open circuit potential to 1.7 V vs RHE before cycling back to 1.2 V vs RHE at 0.20 V/s scan rate. 2-h unsealed controlled-potential electrolysis (CPEs) were performed in the same H-Cell under identical conditions to the RDEV measurements, but at the constant potentials reported. After each unsealed CPE, approximately 2 mL of solution was collected and added to an HPLC vial for product determination.

Sealed CPE experiments were performed in a gas-tight modified H-cell that has been used previously in CO_2 reduction experiments (Figure A.28).[68, 69] Briefly, the catalyst-modified glassy carbon working electrode was held in an RDE internal hardware kit (Pine Research

Instrumentation) and then mounted into a custom PEEK sleeve. This PEEK sleeve was then sealed into a side-on electrode attachment on the working chamber of the H-cell. The working chamber was filled with ~20 mL of electrolyte in which the working electrode and reference electrode were submerged and containing a magnetic Teflon-coated stir bar, and the auxiliary chamber was filled with ~5 mL of electrolyte in which the auxiliary electrode was submerged. The two chambers were separated by a gas-impermeable Nafion 117 membrane. Prior to each sealed electrolysis experiment, the working chamber was sparged with Ar for at least 30 min, and then sealed under Ar atmosphere. R_u was measured and compensated identically to the RDE measurements. Sealed electrolysis experiments were conducted with stirring at the stir bar at the reported applied potentials for 2 h. After each sealed CPE, approximately 2 mL of solution was collected and added to an HPLC vial for product determination. After sealed CPEs for MeOH oxidation, 5 mL of the headspace in the working chamber was collected also to test for CO_2 production.

High performance liquid chromatography (HPLC) product analysis was performed using a Thermo Scientific Ultimax 3000 HPLC system with a UV detector, a Refractomax refractive index detector, and a HyperREZ^{TM} XP Carbohydrate H^+ 7.7 mm x 30 cm (8 µm particle size) column. The column oven was set to a constant 50° C, and the flow rate was isocratic at 0.300 mL min^{-1} using 0.005 M H_2SO_4 as the elution solvent. 30 µL of samples were injected from the HPLC vial into the HPLC instrument for each measurement. Calibrations standards for AOR products were prepared by diluting a stock solution containing both 10 mM of the aldehyde product and 10 mM of the carboxylic product with 1 M NaOH to from calibration standards at the 0.1 mM, 0.5 mM, 1mM, 2mM, 5mM, and 10 mM levels. For each set of possible AOR products, three different calibration curves were constructed from independently prepared stock

solutions, and these curves were averaged to create the final calibration curve for each AOR system. Calibration curves were checked weekly against aldehyde and carboxylic acid standard concentrations, and were updated as needed.

4.4.5 Postmortem Catalyst Collection and Analysis

Postmortem analysis of the Co_2NiO_4 catalysts were conducted after unsealed CPEs at 1.55 V vs RHE and 1.65 V vs RHE in electrolytes containing 1.0 M NaOH and 100mM *n*-BuOH. Postmortem analysis of the catalyst-modified surfaces and Co_2NiO_4 particles included a combination of SEM, XPS, pXRD, and ICP-MS measurements. Postmortem SEM and XPS measurements were conducted directly on the modified working electrode upon removing it from electrolyte after the unsealed CPE measurements. The modified working electrodes were lightly rinsed with water, but otherwise unaltered after removing them from the electrolyte solution before the SEM and XPS measurements.

For postmortem pXRD and ICP-MS measurements, particles were collected from the electrode surface using a previously-reported procedure.[66] Briefly, each modified working electrodes were removed from electrolyte and RDE sheath after the unsealed CPE measurements and submerged in *i*-PrOH in a centrifuge tube. The centrifuge tube containing the modified working electrodes in *i*-PrOH was sonicated for 30 min to dissolve the Nafion binder and release the particles into the *i*-PrOH. After sonication, the working electrodes were rinsed into the centrifuge tube with *i*-PrOH to remove any residual catalyst, and then the working electrodes were removed. This process was repeated for 7-8 modified working electrodes such that ~1 mg of catalyst powder is suspended in the centrifuge tube. The centrifuge tube containing the catalyst powder was then centrifuged at 7000 rpm, and the supernatant was decanted leaving being the postmortem catalyst for analysis. The remaining powder was dried under vacuum, and

collected for postmortem pXRD using the procedure described above. After the pXRD experiments, the samples were digested in 1 M HNO_3, diluted by a factor of 100, and analyzed using ICP-MS according to the procedure described above. Note that from postmortem ICP-MS using this procedure we are able to estimate the elemental composition of the catalyst, but not the post-mortem catalyst loading because the analysis is conducted on a composite from multiple electrodes. The entire process, from powder collection to pXRD and ICP-MS analysis, was conducted at 3 times to collect relevant averages and standard deviations (using electrodes from 21-24 unsealed CPEs at each potential).

4.5 Results

4.5.1 Material characterization

Co_2NiO_4 particles were synthesized by a gelation-thermal decomposition method, and the resulting powder was analyzed by PXRD, ICP-MS, and BET gas adsorption, and the results are summarized in Table A.8-A.9. The PXRD pattern of the as-synthesized Co_2NiO_4 matches closely with that of a spinel Co_2NiO_4 reference as seen in Figure 4.2a. The absence of diffraction peaks from Co_3O_4 and NiO suggests the synthesized materials are phase pure. ICP-MS measurements of the as-synthesized Co_2NiO_4 powder dissolved in 1 M HNO_3 show Co and Ni ions in a Co/Ni ratio of 2.07 ± 0.05, close to the theoretical Co/Ni ratio of 2.00 expected for Co_2NiO_4. The BET surface area of the as-synthesized Co_2NiO_4 material is 80.9 ± 3.1, similar to that reported previously for $CoNiO_4$ materials prepared using similar synthesis procedures.[70-72]

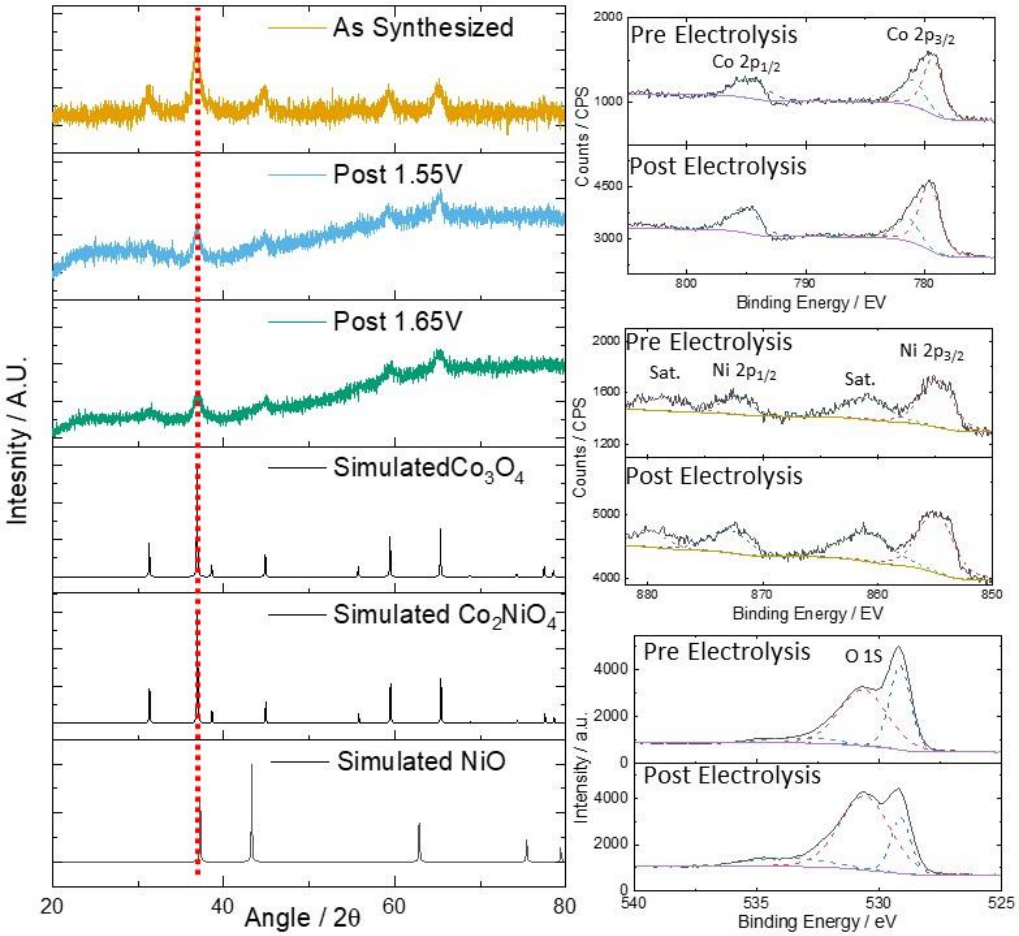

Figure 4.2a. PXRD patterns for the as synthesized, and post electrolysis samples showing good agreement with all samples with the Co_2NiO_4 simulation suggesting a phase pure material was synthesized. b. shows the pre and post electrolysis Cobalt high resolution XPS spectrum with both the Co $2p_{1/2}$ and Co $2p_{3/2}$ peaks labeled. c. shows the pre and post electrolysis nickel high resolution XPS spectrum with the Ni $2p_{1/2}$, Ni $2p_{3/2}$, and corresponding satellite peaks labeled.

The Co_2NiO_4 catalysts were dropcast with a Nafion binder onto 0.195 cm^2 glassy carbon electrodes at a catalyst loading of 0.84 mg cm^{-2}, and the resulting films were characterized by XPS and SEM-EDS. SEM images of the surface show a well defined surface. To determine elemental composition of the deposited film, EDS measurements were conducted on three random spots on each SEM image, and this was repeated on three different independently-prepared catalyst films. The EDS measurements indicate the catalyst films have an average Co/Ni ratio of 2.07 ± 0.02, consistent with the ICP-MS measurements of the as-synthesized material and close to the theoretical value of 2.00 for Co_2NiO_4.

Representative XPS core scans of the as-synthesized Co_2NiO_4 material in the Co 2p, Ni 2p, and O 1s regions are shown in Figure 4.2b (for completeness, the C 1s region is included in Figure A.25). The Co/Ni ratio based on XPS analysis was 1.96 ± 0.02, which is close to the value observed from ICP-MS analysis of the as-synthesized powder and that from the EDS measurements of the deposited catalyst film. The XPS compositional analysis provides a fourth level of confirmation that the material deposited has analogous elemental composition to that of Co_2NiO_4.

In the Co 2p spectra, there are two broad peaks centered at 779.7 eV and 794.7 eV binding energies that are assigned to Co 2 $p_{3/2}$ and Co $2p_{1/2}$, respectively. Each Co peak has two Co contributions assigned to Co^{3+} and Co^{2+}, with Co^{3+} being the primary contribution.[73] The absence of shakeup peak in the Co XPS suggests the Co atoms exists in a Co_3O_4-like environment.[74, 75] In the Ni 2p spectra, there are two broad peaks centered at 854.8 eV and 872.3 eV binding energies that are assigned to Ni 2 $p_{3/2}$ and 2 $p_{1/2}$, respectively, accompanied by satellite peaks. These peaks are consistent with those assigned to Ni^{2+} cations in $Co_xNi_yO_z$ materials.[76] The O 1s spectra shows a broad, convoluted peak with major O contributions

centered at 529.7 eV, 531.2 eV, and 533.2 eV binding energies. These O contributions are attributed to O ions existing in M(OOH), $M(OH)_2$, and moisture oxygen-like environments, respectively.[77-80] In general, this XPS characterization is consistent with other synthesized Co_2NiO_4 spinel materials.[81]

4.5.2 Postmortem Characterization of CO_2NiO_4

The PXRD, ICP-MS, SEM-EDS, and XPS measurements described above are consistent with our assignment of the as-synthesized material as a phase-pure Co_2NiO_4 spinel material, and suggest that the material composition and phase is retained upon dropcasting the catalyst in electrocatalytic films onto the glassy carbon electrode surface. However, it is also important to confirm whether the catalyst structure and composition is maintained after electrochemical AOR experiments.[66, 82-84] To this end, we conducted postmortem materials characterization on the Co_2NiO_4 catalysts after subjecting electrocatalytic films to rotating disk electrode controlled potential electrolysis (RDE-CPE) measurements under catalytically-relevant conditions: mounted into a rotating-disk electrode (RDE) assembly at 1600 rpm rotation rate and held at 1.55 V vs RHE in 0.1 M NaOH electrolyte with 0.10 M *n*-BuOH. A representative RDE-CPE experiment under these conditions is shown in Figure A.41, and shows a modest ~25% decrease in activity over the 2-h electrolysis consistent with the modest activity losses seen for various analogously prepared catalyst films studied for the OER.[65, 85, 86]

Postmortem analysis suggests that the Co_2NiO_4 catalyst phase is maintained even after electrolysis. XPS Core scans of the Co 2p and Ni 2p regions for the post-CPE film are nearly identical to those of the as-synthesized Co_2NiO_4 catalyst film as seen in Figure 4.2b, suggesting the Co and Ni environment on the catalyst surface is maintained after electrochemical measurements. The XPS core scan of the O 1s region shows a modest change in the intensity of

the peak contribution at 529.7 eV increasing relative to the peak contribution at 531.2 eV compared to that of the as-synthesized catalyst film. This change in the O 1s spectra is consistent with a relative increase in the surface speciation for $Co(OH)_2$ compared to Co(OOH), but is not indicative of a change in the overall catalyst structure. The Co/Ni ratio calculated from postmortem XPS analysis is 1.91 ± 0.07, only very slightly increased compared to that from the film prepared with the as-synthesized catalysts and still close to the expected value of 2.00 for Co_2NiO_4. The elemental composition of the post-CPE film was confirmed with SEM-EDS measurements that show a Co/Ni ratio of 2.05 ± 0.01.

After the CPE measurements, the deposited catalysts was removed from several electrodes and combined to collect enough material for PXRD and ICP-MS analysis. ICP-MS measurements of the post-CPE catalysts harvested from the electrodes show a Co/Ni ratio of 2.18 ± 0.09, providing another confirmation that the composition of the post-CPE catalyst is not changed substantially compared to the as-synthesized materials. PXRD patterns of the harvested catalyst material suggests the catalysts retain crystallinity after CPE experiments, although there is an increase in the baseline compared to the peak heights in the post-CPE PXRD patterns compared to those of the as-synthesized material. This increase in background in the PXRD patterns likely results from the relatively small amount of sample harvested and present on the XRD sample disk, which in turn results in increased contribution from the amorphous back material. However, we caution that we cannot discount conclusively that this increase in background in the PXRD for the post-CPE measurements is not indicative of a slight decrease in catalyst crystallinity.

Overall, the postmortem analysis suggests that Co_2NiO_4 material remains largely intact after the electrochemical CPE measurements. The modest loss of activity observed over the

course of the 2-h CPE experiments likely is not due to catalyst degradation, but instead may result from a modest extent of film delamination or physical catalyst loss from the electrode under rotation.

4.5.3 The Electrocatalytic Alcohol Oxidation Reaction by Co_2NiO_4

Co_2NiO_4 is a competent catalyst for the electrocatalytic oxidation of aliphatic alcohols with onset potentials less positive than that for the OER, as shown in the rotating disk cyclic voltammograms (RDEVs) in Figure 4.2a. When exposed to solutions of 1 M NaOH in the absence of any added alcohols, Co_2NiO_4 is a moderately active catalyst for the OER, achieving 10 mA cm^{-2}_{geo} current density at 0.39 ± 0.01 V vs RHE. This OER activity is similar to that reported for the Co_3O_4,[65, 87, 88] and consistent with the reported activities of similar Co-Ni OER catalysts.[89-92] Note that there is a reversible redox feature prior to the onset of the OER at 1.42 V vs RHE (Figure 4.3a) and this redox feature is attributed to the $Co^{3+/4+}$ couple of the Co_2NiO_4 material.[28, 46] The oxidation of the surface species to Co^{4+} in Co_3O_4-based materials is hypothesized to be critical in the OER mechanism for these systems.[93]

Upon addition of 0.1 M C_1-C_5 straight chain aliphatic alcohols to the 1 M NaOH electrolyte, there is a large increase in the catalytic activity at potentials more positive than the onset of the OER, as seen in the representative RDEVs in Figures 3b-e. The onset of catalytic activity for the AOR at Co_2NiO_4 occurs identically at ~1.4 V vs RHE for all alcohols investigated, and this is consistent with previous studies of the AOR at Co_2NiO_4.[46] The catalytic onset for the AOR coincides with the $Co^{3+/4+}$ redox couple, and suggests that oxidation of the Co sites to Co^{4+} is necessary for the AOR. Thus, the onset potential of the AOR is dictated by the $Co^{3+/4+}$ potential of the Co_2NiO_4 material, and this explains why every alcohol investigated has an identical onset at ~1.4 vs RHE regardless of alcohol identity. Note that the electrocatalytic

AOR activity by Co_3NiO_4 is highly dependent on electrolyte pH, and nearly all activity is lost if the electrolyte is made even moderately less basic at pH = 12 (Figure A.37).

For comparison, the AOR activity of the Co_3O_4 parent material and an electrodeposited $CoNiO_x$ catalyst were also investigated. RDEVs of the OER and oxidation of *n*-BuOH at Co_3O_4 and $CoNiO_x$ are shown in Figures S1 and S10, respectively. The Co_3O_4 shows some small activity for *n*-BuOH oxidation, but this activity is almost negligible compared to that of Co_2NiO_4 (Figure A.30). Note that this result is consistent with previous reports that show that general AOR activity of Co_3O_4-based materials increase with Ni doping.[94] Electrodeposited $CoNiO_x$ materials demonstrated no appreciable activity for the AOR (Figure A.36), suggesting that the specific structure of the Co_2NiO_4 may be important for the observed higher catalytic activity of the crystalline material.

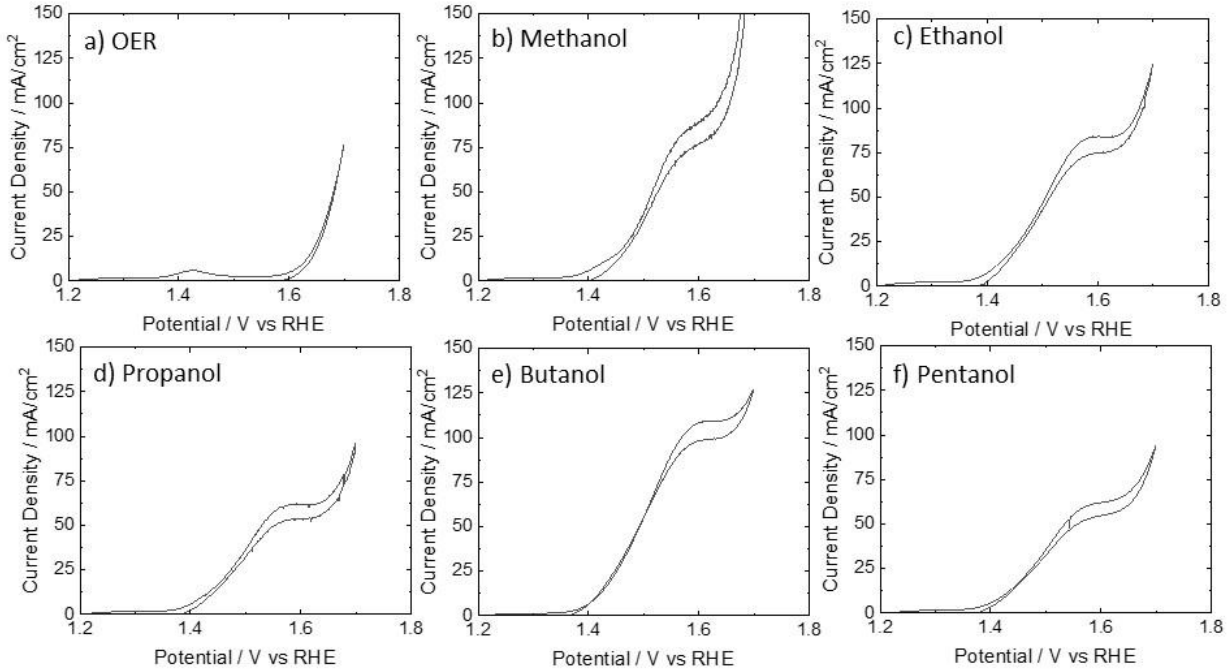

Figure 4.3 Representative cyclic voltammograms for the Co_2NiO_4 catalyst under a. OER conditions b. 100mM methanol, c. 100mM ethanol, d. 100mM n-propanol, e. 100mM n-butanol, and f. 100mM n-pentanol. All tests were performed on glassy carbon disks rotating at 1600 RPM in 1M NaOH electrolyte.

To quantify the products of the AOR for each alcohol investigated, we conducted a series of 2-h sealed-cell controlled potential electrolysis experiments at 1.55 V vs RHE (SC-CPE). The catalyst-modified working electrodes were sealed into a gas-tight electrolysis cell as previously described (Figure A.28).[68, 69] The electrolyte was sparged vigorously with Ar prior to the experiments, and the electrolysis cell was sealed under an Ar atmosphere. The electrolyte was stirred with a magnetic stir bar at 600 rpm stir rate throughout each SC-CPE measurement. The potential of 1.55 V vs RHE was chosen for these measurements because there is appreciable AOR at this potential for all alcohols investigated based on the RDEVs in Figure 4.3, but it is less positive than the onset of the competitive OER. After each SC-CPE experiment, the electrolyte solution was analyzed for solution-phase products using HPLC, and representative HPCL chromatographs are shown on Figures S5-S9. The average product distribution from three independent 2-h SC-CPE measurements for each alcohol investigated is shown in Figure 4.4a-b, and tabulated in Table A.10. For the C2-C5 alcohols investigated, their combined 2 e^- aldehyde products and 4 e^- carboxylic acid products account for > 95% of the Faradaic efficiency in the SC-CPE experiments (Figure 4.4a).

In the case of MeOH, the measured Faradaic efficiency is only ~36%, and the only measured product at appreciable concentration is formic acid. Previous reports have suggested that MeOH can be oxidized by 6 e^- to CO_2 under similar conditions to those used in this study,[95-97] but we see no evidence of CO_2 production in our system. In particular, following SC-CPE experiments with MeOH, we sampled also the headspace of the sealed cell subsequent to the electrolysis experiments and used gas chromatography (GC) to look for the presence of CO_2 in the headspace. No CO_2 was detected above the limit of quantification for CO_2, ~0.04% v/v CO_2 for our instrument and method. If CO_2 produced were at the limit of quantification, the CO_2 level would correspond to < 1 C of

charge for MeOH oxidation to CO_2, or < 2% Faradaic efficiency for CO_2 production. Additionally, Co_2NiO_4 shows no appreciable electrochemical activity for HCOOH oxidation compared to the OER background activity (Figure A.44), suggesting that MeOH oxidation does not proceed past the 4 e^- oxidation to HCOOH, at least in a stepwise manner. These results suggest that the unaccounted for product is likely not CO_2. Instead, we postulate that the unaccounted for product may be HCHO, and that HCHO polymerization in aqueous solution may be inhibiting product detection in our HPLC system. [98-100]

For all alcohols investigated, the Faradaic efficiency for the AOR to the carboxylic acid product increases with increasing chain length, and the Faradaic efficiency for the aldehyde product consequently decreases with increasing chain length. We hypothesized this change in Faradaic efficiency may be related to the solubility and diffusion coefficient of the 2 e^- oxidized aldehyde product. This result is consistent with the AOR occurring via a cascade (or tandem) catalysis mechanism, in which the alcohol is oxidized sequentially to the 2-e^- oxidized aldehyde product, and then again to the 4-e^- oxidized carboxylic acid product. In such a cascade catalysis, the retention of the aldehyde intermediate product at the catalyst surface is crucial for the subsequent oxidation steps. Longer-chain alkyl-aldehydes with lower water solubility and smaller diffusion coefficients will have larger retention times at the catalyst surface, leading to the production of more-oxidized final products as is observed in our experimental results.

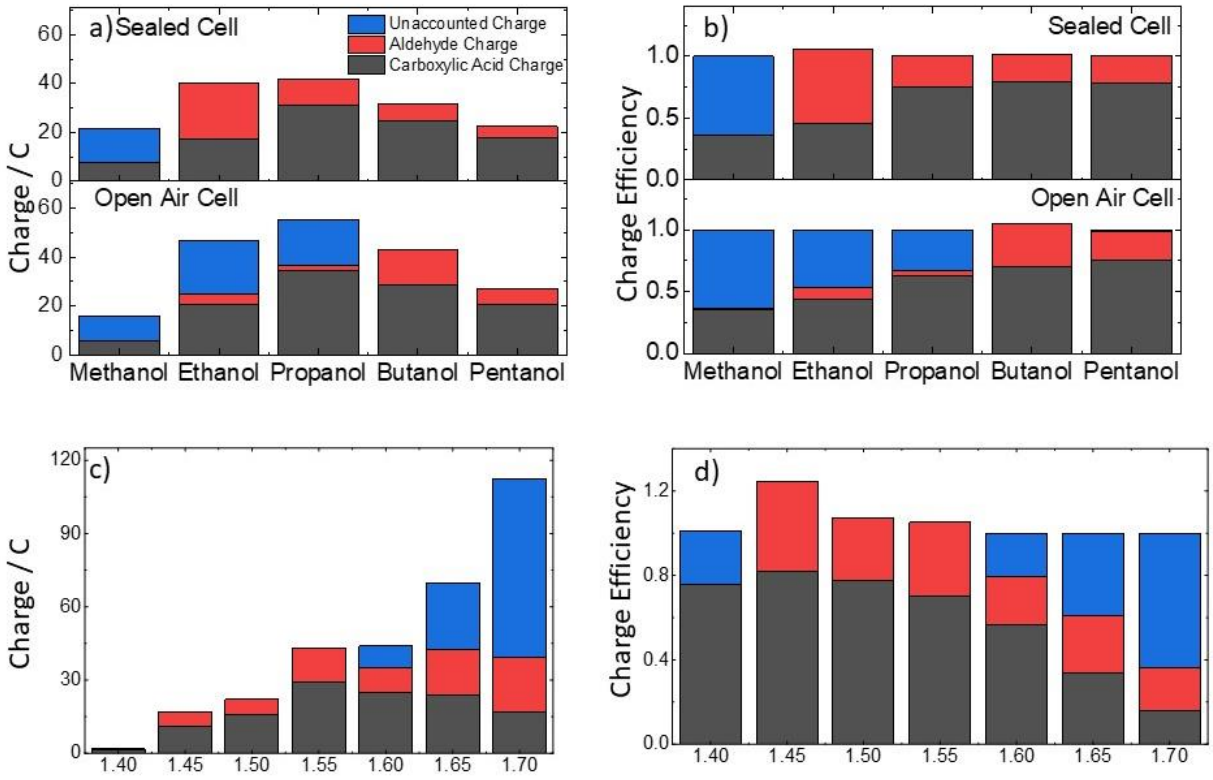

Figure 4.4 a. shows the specific charge passed as a function of added alcohol (100Mm) in 1M NaOH in both a sealed (upper) and unsealed (lower) cell setup. The grey trace shows the charge for the 4 electron carboxylic acid product, the red trace shows the specific charge passed for the 2 electron aldehyde product and the blue trace shows all unaccounted charge passed. b. shows the corresponding charge efficiency for these experiments, with the colors corresponding to the specific product. The upper and lower graphs represent the sealed, and unsealed cell setups. c. shows the potential dependence for the bulk electrolysis of 1M NaOH solutions containing 100mM n-butanol with an unsealed setup under hydrodynamic control. d. shows the corresponding charge efficiencies from experiments in c.

One limitation of SC-CPE measurements is that mass transport is ill defined in the system. This can complicate interpretation of activity metrics in these studies. To this end, we also conducted controlled-potential electrolysis measurements under hydrodynamic control using a rotating disk electrode in an unsealed electrolysis cell under air (Figure A.29). In these RDE-CPE studies, the catalyst-modified rotating disk electrode is rotated at 1600 rpm to ensure rapid delivery of substrate to the electrode, and controlled egress of product from the electrode. The average product distribution from three independent 2-h RDE-CPE measurements for each alcohol investigated is shown in Figure 4.4a-b, and tabulated in Table A.11. Note that the total Faradaic efficiencies for the measured carboxylic acid and aldehyde products from the RDE-CPE measurements with EtOH and *n*-PrOH are < 100%. We attribute this to the evaporative loss of the volatile CH_3CHO and C_2H_5CHO aldehyde products from the aqueous solution prior to HPLC detection.[101] In the SC-CPE studies, where evaporative loss was minimized, the Faradaic efficiencies for the measured carboxylic acid and aldehyde products from oxidation of EtOH and *n*-PrOH were 100%. The total Faradaic efficiency for the measured products from RDE-CPE experiments with MeOH is < 100%, similar to what we observed in our SC-CPE measurements, and we again suggest this may be due to formation of a polymerized-HCHO product not detected by our HPLC method.

For each given alcohol, the overall charged passed during the RDE-CPA is larger than that from the SC-CPE measurements, consistent with the larger rate of alcohol transport to the catalyst in the rotating disk system (Figure 4.4a). However, the Faradaic efficiencies for carboxylic acid products from the oxidation of *n*-PrOH, *n*-BuOH, and *n*-PnOH in the RDE-CPA experiments is decreased compared that measured in the SC-CPE experiments. This is consistent with our assertion that the AOR at Co_2NiO_4 occurs via a cascade mechanism—the larger egress

of the aldehyde intermediate products under rotation results in a decrease in the relative production of carboxylic acid. Interestingly, the Faradaic efficiencies for carboxylic acid production from EtOH and MeOH are largely unchanged in the RDE-CPA experiments compared to the SC-CPE experiments. This result may suggests that for small-chain alcohols such as MeOH and EtOH, the egress of the HCHO and CH_3CHO intermediate products are sufficiently fast that they leave the surface rapidly even without electrode rotation

4.5.4 Expanded electrolysis with n-butanol

To explore the possible potential-dependence of the product distribution of the AOR by Co_2NiO_4 catalysts, we conducted RDE-CPE experiments for *n*-BuOH oxidation at different applied potentials between 1.4 V vs RHE, the approximate onset potential of the AOR at Co_2NiO_4, and 1.7 V vs RHE, more positive than the onset potential for the OER. *n*-BuOH was chosen as the model acid for these studies because: 1) it is oxidized Co_2NiO_4 with high activity as evidenced by the RDEV measurements in Figure 4.3e) it is oxidized to both the aldehyde (C_3H_7CHO) and carboxylic acid (C_3H_7COOH) products in the SC-CPE and RDE-CPE measurements in Figure 4.4a-b, allowing us to explore potential-dependence of acid and aldehyde product distributions; and 3) the products of *n*-BuOH are nonvolatile, making its electrocatalytic oxidation amenable to RDE-CPE experiments with full product detection and analysis.

The results of the RDE-CPE measurements of *n*-BuOH oxidation at Co_2NiO_4 at different applied potentials is shown in Figure 4.4c-d. The overall charge passed during the RDE-CPE measurements increases as a function of more positive applied potential, consistent with the RDEV data in Figure 4.2e. At potentials $\leq$ 1.55 V vs RHE, all of the charge goes to the production of CH_3H_7CHO and CH_3H_7COOH. Interestingly, the Faradaic efficiency for

CH_3H_7CHO and CH_3H_7COOH are largely unchanged as a function of applied potential at potentials ≤ 1.55 V vs RHE, remaining at ~75% and ~30%, respectively.

However, at 1.60 V vs RHE, the sum of the partial charges for CH_3H_7CHO and CH_3H_7COOH decreases slightly compared to those at 1.55 V vs RHE, while the total charge passed remains the same. The unaccounted for charge is at 1.60 V is attributed to O_2 production from the OER, which onsets at ~1.60 V vs RHE at Co_2NiO_4. This is mirrored by a decrease in the Faradaic efficiency for CH_3H_7CHO and CH_3H_7COOH production and a corresponding increase in the Faradaic efficiency for an unspecified product, presumably O_2 from the OER. At even more positive potentials ≥ 1.60 V vs RHE, the total charge continues to increase while the partial charges for CH_3H_7CHO and CH_3H_7COOH remain constant. These results suggest that the OER accounts for much of the observed catalytic activity at potentials ≥ 1.60 V vs RHE, and is the primary source of catalytic activity at 1.75 V vs RHE, the most positive potential investigated. Crucially, the fact that the partial charge for CH_3H_7CHO and CH_3H_7COOH production does not *decrease* appreciably at these OER potentials suggests that the OER does not inhibit the AOR at the Co_2NiO_4 catalyst, but is instead a parallel reaction.

4.5.5 Alcohol Oxidation in Highly-Chlorinated Environments

Seawater has been suggested as an ideal water source for solar fuels production.[62-64] However, seawater contains large concentrations of Cl^- ions that can be oxidized to corrosive Cl_2 in the chlorine-evolution reaction (CER) at potentials comparable to those of the OER.[64, 102-105] The possibility of producing corrosive Cl_2 at solar fuels anodes at OER potentials makes seawater an undesirable electrolyte for traditional water-splitting and solar fuels electrolyzers. However, the AOR at Co_2NiO_4 catalysts operates with appreciable activity at potentials less

positive than the onset of the OER and the competing CER. Thus, unlike the OER, the AOR may be compatible with using abundant seawater as an electrolyte source.

To test the ability of Co_2NiO_4 to perform the AOR in chloride-containing environments, we measured the activity and product selectivity for *n*-BuOH in an electrolyte containing 1 M NaOH and 1 M NaCl, approximately double the Cl^- concentration found in natural seawater.[60, 61] In the absence of added alcohol, RDEVs of Co_2NiO_4 in this 1 M NaOH and 1 NaCl electrolyte show higher activity compared to those in a chloride-free 1 M NaOH electrolyte (Figure 4.5a). The onset of the catalysis is the same in both electrolytes. This suggests the CER may be occurring when Cl^- is present in the electrolyte, and that the onset of the CER is the same as that of the OER. These results in the absence of alcohol are qualitatively consistent with previous studies of the CER on the parent Co_3O_4 material.[104, 106, 107]

RDEVs conducted with Co_2NiO_4 catalysts in electrolytes containing 1 M NaOH, 1 M NaCl, and 0.1 M *n*-BuOH show appreciable activity for AOR with a catalytic onset at ~1.4 V vs RHE (Figure 4.5a). The AOR activity observed in the RDEVs in the chloride-containing electrolyte are similar to those conducted in chloride-free electrolyte under otherwise analogous conditions, albeit a possibly slightly lower total activity. To quantify better the charge going to each product, we conducted RDE-CPEs experiments for the oxidation of 0.1 M *n*-BuOH by Co_2NiO_4 catalysts at 1.55 V vs RHE in electrolytes containing 1 M NaOH and 1 M NaCl, and the results are summarized in Figure 4.5b and Table A.12. Analogous RDE-CPEs were conducted in chloride-free electrolyte, and the results of these measurements are included for comparison. The addition of chloride to the electrolyte solution had no bearing on the activity or product selectivity measured in the RDE-CPEs. Specifically, the total charge passed, partial charge for each product (C_3H_7CHO and C_3H_7COOH) (Figure 4.5b), and Faradaic efficiencies

(Table A.12) determined from the RDE-CPEs in the chloride-containing and chloride-free electrolytes were identical. These results suggest that Co_2NiO_4 remains a competent electrocatalyst for the AOR in alkaline chloride-containing electrolytes, and thus may be compatible with using basified seawater as an electrolyte source.

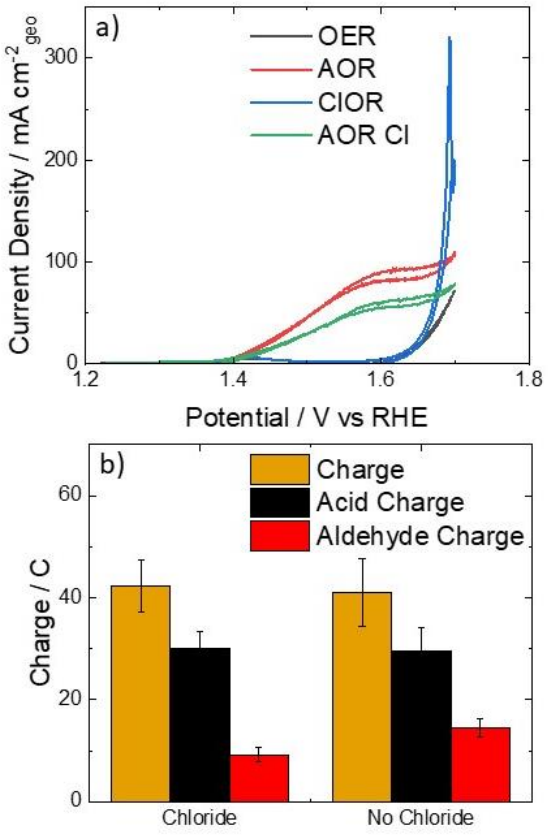

Figure 4.5 a. shows the current density for alcohol oxidation and the background current via cyclic voltammogram for solutions both with and without 1M NaCl added. CVs were taken at 20mV/s scan rate and samples with alcohol contained 100mM n-butanol. B. shows the electrolysis products formed at 1.55V vs RHE applied current density, showing that both chlorinated and non chlorinated electrolysis products are the same and the total charge passed in electrolysis is consistent both with and without chloride ions present.

4.6 Discussion

Much of the work in electrochemical alcohol oxidation focuses on the methanol oxidation reaction.[23, 47, 48] Few of these systems report product analysis after chronoamperometry experiments, with the assumption being, the methanol substrate is completely oxidized to CO_2. Other systems looking at 5-hydroxymethyl-furfural (HMF) oxidation typically report reaction yields for the fully oxidized product 2,5-Furandicarboxylic acid at single potential lacking evidence regarding the rate of product formation in other oxidative regimes. There are reports suggesting a potential dependence in the product formation for HMF, showing an increase in relative production of 5-hydroxymethyl-2-furancarboxylic acid (HMFCA) at more negative potentials suggesting a strong correlation between potential and product formation in HMF oxidation. Our comprehensive report on both alcohol substrate and potential dependence highlights the critical importance of full analysis in these types of systems to include both activity metrics, as well as product analysis at a range of potentials, in order to increase the understanding both of how these systems work, as well as how the product distribution changes as a function of applied potential, including within the OER regime where the competitive OER occurs. Table A.14 shows activity and selectivity metrics reported in a range of studies on various substrates with similar materials for comparison. Lacking within this table are multiple data points for either activity or product formation, this before accounting for the effect that applied potential might have in these types of systems. Our study shows the production of both aldehyde and acid during electrolysis in ratios that suggest that this type of potential dependent data is critical in reporting catalysts and transformations in alcohol oxidation.

We notice that similar to other studies, the onset of oxidation of the oxidation of all alcohols tested correlates to the redox feature observed in the OER cyclic voltammogram which is attributed

to the shifted $Co^{3+/4+}$ redox couple.[46] The specific active site for AOR is not established for this system with both parent oxide materials being active for AOR[25, 37, 108, 109], however the observation that the catalytic onset correlates to one of these oxidative features suggests the mechanistic importance of the oxidized Co^{4+} ions. This is highly similar to what is seen in the OER literature for cobalt catalyzed OER,[93] suggesting that there may be mechanistic similarities between the two systems. Another interesting mechanistic detail is the decrease in AOR activity as the solution pH is decreased from 14 to 12 (Figure A.37). This suggests that at some step in the process a deprotonation, or some other pH dependent reaction, occurs limiting the ability for catalytic turnover at lower pH values. The Koper group in their work on Au surfaces, suggests that the first step in the catalytic cycle for alcohol oxidations is the deprotonation of the hydroxyl group forming a more reaction alkoxide species.[110] Our pH data would suggest this may also be the case in the Co_2NiO_4 system as well with the alkoxide being almost non present at pH 12 due to the high pKa of the protonated alcohol ($pKa_{butanol}$= 16.1).

After the first oxidation of the alcohol group, we propose the $2e^-$ aldehyde product is desorbed from the surface and then interacts with the electrode surface a second time for an independent oxidation to form the $4e^-$ acid product. We notice that for the aldehydes with higher water solubility, there is an increase in aldehyde production and subsequent decrease in acid production, suggesting the diffusion of the aldehyde away from electrode into the bulk solution where it becomes less likely to react with the polarized anode. As the aldehyde solubility decreases the acid concentration is shown to increase, and this is especially prevalent in the sealed cell experiments, as in these systems the decreased solution turbidity at the electrode decreases the likelihood for the insoluble aldehyde to diffuse into the bulk solution thus increasing the likelihood for a second oxidation event to occur. This further supports the hypothesis that the produced

aldehydes are an intermediate to acid production as increased mass transport at the electrode surface, will increase the amount of aldehyde being transported away from the electrode surface.

In the butanol system we also see an inverse relationship between acid production and applied potential as we increase the potential past the onset of OER. This inverse relationship is interesting as the overall production of acid product during this time is lower at 1.7V vs RHE than 1.55V vs RHE so from a purely kinetic standpoint the system is not limited. Therefore, we prose pose that firstly, OER dominates in this potential region primarily due to the 3 order of magnitude higher reagent concentration for oxygen evolution and secondly, that these two systems share a similar mechanistic active site on the electrode surface. Due to the higher presence of OER substrates in the system, these substrates should preferentially interact with surface active sites, effectively consuming active sites for alcohol oxidation. This is signaled by the lower total AOR current as the electrode is further polarized past OER onset.

With this in mind, we propose a mechanistic intercept model where both water and the organic alcohol both share the same catalytic active site. After the oxidation of the Co surface atoms, the deprotonated alcohol attacks the metal site forming a metal oxygen bond similar to the mechanism for oxygen evolution. The alcohol is then oxidized with a proton from the nearest carbon being abstracted by either a surface hydroxide species, or a solution phase hydroxide species, forming the aldehyde intermediate product. Then in a similar way to oxygen evolution, nucleophilic attack by either a hydroxide ion, or another alcohol, regenerates the catalytic active site and eliminates the aldehyde where the cycle can restart. This aldehyde can then interact with the catalyst a second time to be oxidized to the carboxylic acid, or diffuse away from the surface into the bulk, yielding the detected solution phase aldehyde.

4.7 Conclusion

We have shown that our Co_2NiO_4 catalyst is able to catalyze the AOR at applied potentials roughly 200mV less positive to the OER under alkaline conditions. Using n-butanol as our major test alcohol, we were able to show high faradaic efficiency for the AOR at potentials less positive of 1.6V vs RHE, with the $4e^-$ acid product being the predominate species in solution. Past 1.6V vs RHE, the faradaic charge decreased for AOR due to competitive OER dominating at the catalyst surface. We also showed this system works in highly chlorinated with no change to the product distribution observed at 1.55V vs RHE. The relatively high faradic efficiencies for aldehydes observed in this study suggests the presence of two separate oxidation steps where production of the aldehyde precedes the further oxidation of the aldehyde to the carboxylic acid. This study highlights not only a possible mechanistic interpretation for the AOR on Co_2NiO_4 but also highlights the need for potential dependent, and substrate depended product analysis in AOR to discern trends in both activity and selectivity, both of which are critical to account for when discerning the viability for alcohol oxidation as a replacement for the OER.

4.8 References

1. M. Graetzel, *Accounts of Chemical Research*, 1981, **14**, 376-384.
2. A. J. Bard and M. A. Fox, *Accounts of Chemical Research*, 1995, **28**, 141-145.
3. J. A. Turner, *Science*, 2004, **305**, 972-974.
4. N. S. Lewis and D. G. Nocera, *Proc. Natl. Acad. Sci. U.S.A.*, 2006, **103**, 15729-15735.
5. T. E. Mallouk, *Nature Chemistry*, 2013, **5**, 362-363.
6. T. R. Cook, D. K. Dogutan, S. Y. Reece, Y. Surendranath, T. S. Teets and D. G. Nocera, *Chemical Reviews*, 2010, **110**, 6474-6502.
7. J. H. Wang, W. Cui, Q. Liu, Z. C. Xing, A. M. Asiri and X. P. Sun, *Adv. Mater.*, 2016, **28**, 215-230.
8. J. M. Spurgeon and B. Kumar, *Energy & Environmental Science*, 2018, **11**, 1536-1551.
9. J. Na, B. Seo, J. Kim, C. W. Lee, H. Lee, Y. J. Hwang, B. K. Min, D. K. Lee, H.-S. Oh and U. Lee, *Nature Communications*, 2019, **10**, 5193.
10. R. Yukesh Kannah, S. Kavitha, Preethi, O. Parthiba Karthikeyan, G. Kumar, N. V. Dai-Viet and J. Rajesh Banu, *Bioresource Technology*, 2021, **319**, 124175.
11. M. W. Kanan and D. G. Nocera, *Science*, 2008, **321**, 1072-1075.

12. N.-T. Suen, S.-F. Hung, Q. Quan, N. Zhang, Y.-J. Xu and H. M. Chen, *Chemical Society Reviews*, 2017, **46**, 337-365.
13. M. Tahir, L. Pan, F. Idrees, X. Zhang, L. Wang, J.-J. Zou and Z. L. Wang, *Nano Energy*, 2017, **37**, 136-157.
14. J. Wang, J. Liu, B. Zhang, F. Cheng, Y. Ruan, X. Ji, K. Xu, C. Chen, L. Miao and J. Jiang, *Nano Energy*, 2018, **53**, 144-151.
15. Y. Wang, D. Yan, S. El Hankari, Y. Zou and S. Wang, *Advanced Science*, 2018, **5**, 1800064.
16. H.-Y. Su, Y. Gorlin, I. C. Man, F. Calle-Vallejo, J. K. Nørskov, T. F. Jaramillo and J. Rossmeisl, *Physical Chemistry Chemical Physics*, 2012, **14**, 14010-14022.
17. W. T. Hong, M. Risch, K. A. Stoerzinger, A. Grimaud, J. Suntivich and Y. Shao-Horn, *Energy & Environmental Science*, 2015, **8**, 1404-1427.
18. Y. Huang, R. Yang, G. Anandhababu, J. Xie, J. Lv, X. Zhao, X. Wang, M. Wu, Q. Li and Y. Wang, *ACS Energy Letters*, 2018, **3**, 1854-1860.
19. C. R. Lhermitte and K. Sivula, *ACS Catalysis*, 2019, **9**, 2007-2017.
20. Y. Zhong, R.-Q. Ren, L. Qin, J.-B. Wang, Y.-Y. Peng, Q. Li and Y.-M. Fan, *New J. Chem.*, 2021, **45**, 11213-11221.
21. F. J. Holzhäuser, T. Janke, F. Öztas, C. Broicher and R. Palkovits, *Advanced Sustainable Systems*, 2020, **4**, 1900151.
22. M. T. Bender, X. Yuan and K.-S. Choi, *Nature Communications*, 2020, **11**, 4594.
23. J. B. Wu, Z. G. Li, X. H. Huang and Y. Lin, *Journal of Power Sources*, 2013, **224**, 1-5.
24. S. Sun, Y. Zhou, B. Hu, Q. Zhang and Z. J. Xu, *J. Electrochem. Soc.*, 2015, **163**, H99-H104.
25. S. Sun, L. Sun, S. Xi, Y. Du, M. U. Anu Prathap, Z. Wang, Q. Zhang, A. Fisher and Z. J. Xu, *Electrochimica Acta*, 2017, **228**, 183-194.
26. D. Martín-Yerga, G. Henriksson and A. Cornell, *Electrocatalysis*, 2019, **10**, 489-498.
27. V. Hassanzadeh, M. A. Sheikh-Mohseni and B. Habibi, *Journal of Electroanalytical Chemistry*, 2019, **847**, 113200.
28. L. Gao, Y. Bao, S. Gan, Z. Sun, Z. Song, D. Han, F. Li and L. Niu, *ChemSusChem*, 2018, **11**, 2547-2553.
29. M. J. Kang, H. Park, J. Jegal, S. Y. Hwang, Y. S. Kang and H. G. Cha, *Applied Catalysis B: Environmental*, 2019, **242**, 85-91.
30. Z. Zhou, C. Chen, M. Gao, B. Xia and J. Zhang, *Green Chemistry*, 2019, **21**, 6699-6706.
31. X. Deng, G.-Y. Xu, Y.-J. Zhang, L. Wang, J. Zhang, J.-F. Li, X.-Z. Fu and J.-L. Luo, *Angew. Chem. Int. Ed.*, 2021, **60**, 20535-20542.
32. N. Jiang, B. You, R. Boonstra, I. M. Terrero Rodriguez and Y. Sun, *ACS Energy Letters*, 2016, **1**, 386-390.
33. X. Liu, B. Li, G. Han, X. Liu, Z. Cao, D.-e. Jiang and Y. Sun, *Nature Communications*, 2021, **12**, 1868.
34. B. You, X. Liu, N. Jiang and Y. Sun, *Journal of the American Chemical Society*, 2016, **138**, 13639-13646.
35. D.-H. Nam, B. J. Taitt and K.-S. Choi, *ACS Catalysis*, 2018, **8**, 1197-1206.
36. H. G. Cha and K.-S. Choi, *Nature Chemistry*, 2015, **7**, 328-333.
37. Y. Cao, D. Zhang, X. Kong, F. Zhang and X. Lei, *Journal of Materials Science*, 2021, **56**, 6689-6703.

38. R. Zhang, S. Jiang, Y. Rao, S. Chen, Q. Yue and Y. Kang, *Green Chemistry*, 2021, **23**, 2525-2530.
39. R. Elakkiya and G. Maduraiveeran, *New Journal of Chemistry*, 2019, **43**, 14756-14762.
40. X. Huang, J. Song, M. Hua, Z. Xie, S. Liu, T. Wu, G. Yang and B. Han, *Green Chemistry*, 2020, **22**, 843-849.
41. T. Vijayabarathi, S. Muzhumathi and M. Noel, *Journal of Applied Electrochemistry*, 2007, **37**, 297-301.
42. W. J. King and A. C. C. Tseung, *Electrochimica Acta*, 1974, **19**, 493-498.
43. J. Zhan, M. Cai, C. Zhang and C. Wang, *Electrochimica Acta*, 2015, **154**, 70-76.
44. R. Ding, L. Qi, M. Jia and H. Wang, *Catalysis Science & Technology*, 2013, **3**, 3207-3215.
45. L. Hu, L. Wu, M. Liao, X. Hu and X. Fang, *Advanced Functional Materials*, 2012, **22**, 998-1004.
46. X. Deng, G.-Y. Xu, Y.-J. Zhang, L. Wang, J. Zhang, J.-F. Li, X.-Z. Fu and J.-L. Luo, *Angewandte Chemie International Edition*, 2021, **n/a**.
47. S. Chen, D. Huang, D. Liu, H. Sun, W. Yan, J. Wang, M. Dong, X. Tong and W. Fan, *Applied Catalysis B: Environmental*, 2021, **291**, 120065.
48. A. K. Das, S. Jena, S. Sahoo, R. Kuchi, D. Kim, T. A. Aljohani, G. C. Nayak and J.-R. Jeong, *Journal of Saudi Chemical Society*, 2020, **24**, 434-444.
49. Y. Zhong, R. Ren, L. Qin, J. Wang, Y. Peng, Q. Li and Y. Fan, *New Journal of Chemistry*, 2021, DOI: 10.1039/D1NJ01489G.
50. Y. Yang and T. Mu, *Green Chemistry*, 2021, DOI: 10.1039/D1GC00914A.
51. B. Liu, S. Xu, M. Zhang, X. Li, D. Decarolis, Y. Liu, Y. Wang, E. K. Gibson, C. R. A. Catlow and K. Yan, *Green Chemistry*, 2021, DOI: 10.1039/D1GC00901J.
52. O. Simoska, Z. Rhodes, S. Weliwatte, J. R. Cabrera-Pardo, E. M. Gaffney, K. Lim and S. D. Minteer, *ChemSusChem*, 2021, **14**, 1674-1686.
53. L. Dai, Q. Qin, X. Zhao, C. Xu, C. Hu, S. Mo, Y. O. Wang, S. Lin, Z. Tang and N. Zheng, *ACS Central Science*, 2016, **2**, 538-544.
54. B. You, G. Han and Y. Sun, *Chemical Communications*, 2018, **54**, 5943-5955.
55. B. J. Taitt, D.-H. Nam and K.-S. Choi, *ACS Catalysis*, 2019, **9**, 660-670.
56. M. T. Bender, R. E. Warburton, S. Hammes-Schiffer and K.-S. Choi, *ACS Catalysis*, 2021, **11**, 15110-15124.
57. D. J. Chadderdon, L. Xin, J. Qi, Y. Qiu, P. Krishna, K. L. More and W. Li, *Green Chemistry*, 2014, **16**, 3778-3786.
58. C. Dai, L. Sun, H. Liao, B. Khezri, R. D. Webster, A. C. Fisher and Z. J. Xu, *Journal of Catalysis*, 2017, **356**, 14-21.
59. Y. Kwon and M. T. M. Koper, *Analytical Chemistry*, 2010, **82**, 5420-5424.
60. H. W. Harvey, *Journal of the Marine Biological Association of the United Kingdom*, 1956, **35**, 289-289.
61. C. Huber, I. Klimant, C. Krause, T. Werner, T. Mayr and O. S. Wolfbeis, *Fresenius' journal of analytical chemistry*, 2000, **368**, 196-202.
62. S. Fukuzumi, *Joule*, 2017, **1**, 689-738.
63. K. Nakata, T. Ozaki, C. Terashima, A. Fujishima and Y. Einaga, *Angew. Chem. Int. Ed.*, 2014, **53**, 871-874.
64. S. Fukuzumi, Y.-M. Lee and W. Nam, *ChemSusChem*, 2017, **10**, 4264-4276.
65. C.-C. Lin and C. C. L. McCrory, *ACS Catal.*, 2017, **7**, 443-451.

66. S. E. Michaud, M. T. Riehs, W.-J. Feng, C.-C. Lin and C. C. L. McCrory, *Chemical Communications*, 2021, **57**, 883-886.
67. D. A. Corrigan and R. M. Bendert, *Journal of The Electrochemical Society*, 1989, **136**, 723-728.
68. Y. Liu and C. C. L. McCrory, *Nature Communications*, 2019, **10**, 1683.
69. T. L. Soucy, Y. Liu, J. B. Eisenberg and C. C. L. McCrory, *ACS Appl. Energy Mater.*, 2021, **ASAP**.
70. S. Ghosh, R. Jana, S. Ganguli, H. R. Inta, G. Tudu, H. V. S. R. M. Koppisetti, A. Datta and V. Mahalingam, *Nanoscale Advances*, 2021, **3**, 3770-3779.
71. P. Peshev, A. Toshev and G. Gyurov, *Mater. Res. Bull.*, 1989, **24**, 33-40.
72. B. Chi, J.-B. Li, Y.-S. Han and J.-H. Dai, *Mater. Lett.*, 2004, **58**, 1415-1418.
73. J.-X. Feng, S.-H. Ye, A.-L. Wang, X.-F. Lu, Y.-X. Tong and G.-R. Li, *Adv. Funct. Mater.*, 2014, **24**, 7093-7101.
74. P. W. Menezes, A. Indra, D. González-Flores, N. R. Sahraie, I. Zaharieva, M. Schwarze, P. Strasser, H. Dau and M. Driess, *ACS Catalysis*, 2015, **5**, 2017-2027.
75. M. Oku and K. Hirokawa, *Journal of Electron Spectroscopy and Related Phenomena*, 1976, **8**, 475-481.
76. L.-K. Wu, W.-Y. Wu, J. Xia, H.-Z. Cao, G.-Y. Hou, Y.-P. Tang and G.-Q. Zheng, *Journal of Materials Chemistry A*, 2017, **5**, 10669-10677.
77. N. S. McIntyre and M. G. Cook, *Analytical Chemistry*, 1975, **47**, 2208-2213.
78. K. J. Kim, M. K. Rath, H. H. Kwak, H. J. Kim, J. W. Han, S.-T. Hong and K. T. Lee, *ACS Catalysis*, 2019, **9**, 1172-1182.
79. X. He, Y. D. Huang, X. T. Sun, P. Du, Z. B. Zhao, R. Y. Wang, H. Yang, Y. Wang and K. Huang, *Applied Physics A*, 2020, **126**, 841.
80. I. Thaheem, S. Ali, M. Waqas, A. Hussain, A. M. Soomro, Z. Bhutto, S. A. R. Shah, W. Muhammad and J. Shah, *physica status solidi (a)*, 2022, **219**, 2100542.
81. J. G. Kim, D. L. Pugmire, D. Battaglia and M. A. Langell, *Appl. Surf. Sci.*, 2000, **165**, 70-84.
82. M. B. Stevens, L. J. Enman, A. S. Batchellor, M. R. Cosby, A. E. Vise, C. D. M. Trang and S. W. Boettcher, *Chem. Mater.*, 2017, **29**, 120-140.
83. C. Wei, R. R. Rao, J. Peng, B. Huang, I. E. L. Stephens, M. Risch, Z. J. Xu and Y. Shao-Horn, *Adv. Mater.*, 2019, DOI: 10.1002/adma.201806296, 1806296.
84. S. Geiger, O. Kasian, M. Ledendecker, E. Pizzutilo, A. M. Mingers, W. T. Fu, O. Diaz-Morales, Z. Li, T. Oellers, L. Fruchter, A. Ludwig, K. J. J. Mayrhofer, M. T. M. Koper and S. Cherevko, *Nat. Catal.*, 2018, **1**, 508-515.
85. K. Y. Niu, F. Lin, S. Jung, L. Fang, D. Nordlund, C. C. L. McCrory, T. C. Weng, P. Ercius, M. M. Doeff and H. M. Zheng, *Nano Lett.*, 2015, **15**, 2498-2503.
86. S. Jung, C. C. L. McCrory, I. M. Ferrer, J. C. Peters and T. F. Jaramillo, *Journal of Materials Chemistry A*, 2016, **4**, 3068-3076.
87. C. Alex, S. C. Sarma, S. C. Peter and N. S. John, *ACS Applied Energy Materials*, 2020, **3**, 5439-5447.
88. P. T. Babar, A. C. Lokhande, B. S. Pawar, M. G. Gang, E. Jo, C. Go, M. P. Suryawanshi, S. M. Pawar and J. H. Kim, *Applied Surface Science*, 2018, **427**, 253-259.
89. W. J. King and A. C. C. Tseung, *Electrochimica Acta*, 1974, **19**, 485-491.
90. A. Dymerska, W. Kukułka, M. Biegun and E. Mijowska, *Materials (1996-1944)*, 2020, **13**, 3918.

91. I. Abidat, N. Bouchenafa-Saib, A. Habrioux, C. Comminges, C. Canaff, J. Rousseau, T. W. Napporn, D. Dambournet, O. Borkiewicz and K. B. Kokoh, *Journal of Materials Chemistry A*, 2015, **3**, 17433-17444.
92. C. Bocca, A. Barbucci, M. Delucchi and G. Cerisola, *International Journal of Hydrogen Energy*, 1999, **24**, 21-26.
93. M. Zhang, M. de Respinis and H. Frei, *Nature Chemistry*, 2014, **6**, 362.
94. A. R. Jadhav, H. A. Bandal, A. A. Chaugule and H. Kim, *Electrochimica Acta*, 2017, **240**, 277-287.
95. M. U. Anu Prathap and R. Srivastava, *Nano Energy*, 2013, **2**, 1046-1053.
96. Z. Wei, H. Guo and Z. Tang, *Journal of Power Sources*, 1996, **58**, 239-242.
97. M. M. Shahid, A. Pandikumar, A. M. Golsheikh, N. M. Huang and H. N. Lim, *RSC Advances*, 2014, **4**, 62793-62801.
98. W. M. D. Bryant and J. B. Thompson, *Journal of Polymer Science Part A-1: Polymer Chemistry*, 1971, **9**, 2523-2540.
99. J. Kua, J. E. Avila, C. G. Lee and W. D. Smith, *The Journal of Physical Chemistry A*, 2013, **117**, 12658-12667.
100. F. Walker, *The Journal of Physical Chemistry*, 2002, **35**, 1104-1113.
101. K. P. Kuhl, E. R. Cave, D. N. Abram and T. F. Jaramillo, *Energy & Environmental Science*, 2012, **5**, 7050-7059.
102. J. G. Vos, T. A. Wezendonk, A. W. Jeremiasse and M. T. M. Koper, *Journal of the American Chemical Society*, 2018, **140**, 10270-10281.
103. F. Dionigi, T. Reier, Z. Pawolek, M. Gliech and P. Strasser, *ChemSusChem*, 2016, **9**, 962-972.
104. S. Trasatti, *Electrochim. Acta*, 1984, **29**, 1503-1512.
105. C. Belmont, R. Ferrigno, O. Leclerc and H. H. Girault, *Electrochimica Acta*, 1998, **44**, 597-603.
106. L. Szpyrkowicz, M. Radaelli and S. Daniele, *Catal. Today*, 2005, **100**, 425-429.
107. X. Zhu, P. Wang, Z. Wang, Y. Liu, Z. Zheng, Q. Zhang, X. Zhang, Y. Dai, M.-H. Whangbo and B. Huang, *J. Mater. Chem. A*, 2018, **6**, 12718-12723.
108. Q. Zhang, X. Fu, Q. Kan and J. Guan, *Industrial & Engineering Chemistry Research*, 2019, **58**, 4774-4779.
109. R. S. Amin, R. M. A. Hameed, K. M. El-Khatib, M. E. Youssef and A. A. Elzatahry, *Electrochimica Acta*, 2012, **59**, 499-508.
110. Y. Kwon, S. C. S. Lai, P. Rodriguez and M. T. M. Koper, *Journal of the American Chemical Society*, 2011, **133**, 6914-6917.

Chapter 5 Conclusions and Future Work

5.1 Conclusions

This thesis discusses my work on doped $Co_{3-x}M_xO_4$ systems for electrocatalytic oxidation reactions. Initially the projects central hypothesis regarded furthering the understanding on how through a mechanistic understanding we can make systematic changes to materials to develop predictive trends in OER activity. By initiating these studies with Al, Ga, and Fe dopants in Chapter 2 we sought to observe how through changing the electron filling and size of dopant ions we can further elucidate how these changes alter OER activity. However, our initial screening of these materials found that none of these dopant ions were able to improve the activity of Co_3O_4. We then synthesized a full range of Fe doped $Co_{3-x}Fe_xO_4$ finding that low levels of Fe incorporation does increase OER activity with $CO_{2.75}Fe_{0.25}O_4$ showing the highest OER activity with η=0.35V. Past this dopant level however, the activity is found to decrease drastically. We believe this is a two-fold issue with Fe the iron doped system, the first is a higher resistance within the material as calculated through EIS with resistance being observed to increase with increasing Fe content, and due to increased iron oxide phases at the electrode surface which is much less active than a more cobalt rich surface structure.

In Chapter 3 we sought to perform a similar study to that performed in Chapter 2 though use of a vanadium doped CoV_2O_4 catalytic material. Previous literature suggested vanadium has would increase the activity of cobalt oxide based materials. Similar to these studies we showed the our vanadium species has highly active and also three order of magnitude more active than the base Co_3O_4 material when normalized for the BET surface area. However, upon analysis of the

material after electrocatalytic measurements, we discovered a complete lack of vanadium and a new amorphous structure is present suggesting that the activity increase is not due to vanadium incorporation, but rather due to the formation of a new cobalt based amorphous structure formed through the collapse of the initial CoV_2O_4 lattice. This study highlights the critical importance of post electrocatalytic material analysis in the field of electrocatalysis.

In Chapter 4 we synthesized a Co_2NiO_4 catalyst that showed moderate activity for the OER. However, when organic alcohols were added to the solution the activity increases and achieves the similar current densities potentials 200mV less positive to that required for the OER, greatly increasing the viability of this system for an anode in the water splitting reaction. We then tested a range of alcohols for alcohol oxidation activity and selectivity showing an increase in carboxylic acid production as the carbon chain length is increased. We then showed a potential dependent product distribution for alcohol oxidation using butanol as a test substrate which also showed that in regimes where OER is active the OER greatly outcompetes the AOR. However, under moderate conditions, the AOR is a viable anodic alternative to increase current densities in water splitting systems, and to outcompete both alcohol oxidation and chloride oxidation.

Overall, the work presented in this thesis further defines the use of dopant ions in $CO_{3-x}M_xO_4$ systems. The use of dopant ions was shown to affect OER activity, but these alterations did not follow the expected trends which are observed in other cobalt based systems, likely due to the well-ordered structure of the material, which generates well defined catalytic active sites which results in a systems that vary from that observed in electrodeposited systems. This is especially noticeable in Fe doped systems where only low levels of iron increases OER activity in the crystalline phase, where in amorphous phases, iron levels higher than 50% still are shown to increases the OER activity. Additionally, the critical importance of full analysis of the catalytic

material is key when making mechanistic interpretations of the data collected, as highlighted by the studies on vanadium doped CoV_2O_4. By changing the substrate from water to organic alcohols the activity of the anodic reaction can be increased at less positive potentials, and products formed can be changed through modifications to the alcohol system as well as the applied electrochemical bias, opening the door for studies which can eliminate a membrane divider typically required for water splitting systems, while producing value added products.

5.2 Future Directions

Furthering the fundamental understanding of both oxygen evolution and alcohol oxidation will aid in increasing the viability of electrochemical transformations for intermittent energy storage applications. To date most of the focus on understanding how catalysts for the OER operate, has been observing trends within single dopant species, typically these systems are centered around the use of iron, cobalt, and nickel, with a few of these studies branching out into other metals. As work in this area progresses the ability to alter materials with multiple dopant ions offers the ability to produce novel catalytic materials with increased activity for the OER. In the alcohol oxidation reaction the ability to both define new substrates as well as new catalytic materials offer routes to increased oxidative activities, while also increasing the economic value within the system. The remainder of this chapter will focus on the future directions that I foresee research in both areas continuing with a specific focus on catalyst development for OER and AOR, as well as defining key system conditions for alcohol oxidation.

5.3 Co-doping Transition Metals into $Co_{3-x}M_xO_4$ lattices

The work discussed in this dissertation focuses on the doping of single metals into the cobalt oxide lattice. In addition to the dopants discussed chromium dopants have also been

observed in the McCrory lab showing increased activity at all dopant levels.[1] To further these studies co-doping a combination of metals into the cobalt oxide lattice should be performed, as this offers the ability to take advantage positive aspects associated with different dopant species. Various groups have observed increased activity for the OER by doping more than one metal into a catalytic material[2, 3] however, the lack of systematic variations within these studies, limits the ability to uses these systems as a predictive tool for further material development. Taking a more systematic approach to these studies will allow for increased knowledge in how combining metal ions in different concentrations alters the OER activity for cobalt-based oxides. Based off the research presented within this thesis and previously reported in the McCrory lab, these types of studies are a logical next step for progression in the OER catalyst project.

A starting point for these studies, which will be vital in understanding initial co-doped activity trends, is the co-doped Cr and Ni cobalt oxide. The preference of each element to dope into a specific lattice site will allow for separating the effects of the specific dopant on the OER activity trends. The first trend to observe is the importance of specific cobalt sites for OER activity, with this system being able to selectively remove either Co^{2+} or Co^{3+} by maximizing the amount of Ni and Cr dopant ions respectively as each ion will selectively dope into either the T_d or O_h sites. Ni atoms are similar in size to cobalt atoms, thus minimizing the effect that lattice strain might have on the OER activity, while at the same time altering the redox activity of the Co sites, allowing for a controlled method for separating two of effects proposed. Systems like the CoCrNiOx co-doped lattice where effects can be teased out more easily are great starting points for systematic co-doping studies. This study is an ideal starting point for the co doped oxides, due to having two well defined comparison points, that being the activity of the based Co_3O_4, and the

activity of the $Co_{3-x}M_xO_4$ materials, both of which act as comparative baselines for activity measures.

Once this initial baseline study is completed using the Cr and Ni dopants, expansion into other systems should be conducted. Our work with Al, Ga, and Fe suggests these metals should be used for co doping as there already exist baselines for comparison. Of these materials, the most interesting is the Fe samples, this due to the high prevalence of Fe doped oxides in the literature[3, 4] despite our reported low activity with Fe doping. By using cooping as a strategy we will increase the conductivity of these systems allowing the intrinsic activity of cobalt iron oxides to be more apparent should literature reports regarding the high activity of Fe sites to be true.[4, 5] Although Al and Ga were found to be inactive dopants, this inactivity will allow co doping with these ions to be highly effective as they can alter the material properties without having a large impact on the direct catalytic reaction. These studies which expand on our studies using single species doped materials, will allow for insight into how different dopant species interact with one another under electrocatalytic conditions.

5.4 Kinetic Studies for Alcohol Oxidation

To expand upon the work previously discussed on the Co_2NiO_4 system, specifically as it pertains to alcohol oxidation, the next step is defining kinetic parameters for both alcohol oxidation and aldehyde oxidation on the substrates already tested. Discerning the specific kinetics for alcohol oxidation allows for further investigation into catalytic mechanism as well as other systems which might be active for the AOR.[6] Due to the production of a reactive intermediates, as well as a competitive OER at more positive potentials, this type of analysis is nontrivial for alcohol oxidation as isolating the specific currents at a given time point is difficult. However, if operating potentials are kept negative of the OER onset potential, the competitive reaction currents can be

minimized. This data coupled with activity and kinetic data from performing identical studies on the intermediate itself will allow for the back calculation of the specific kinetic parameters for the oxidation of the alcohol substrate. These studies will first be completed through performing rotation rate dependent electrolysis on the aldehyde intermediate and alcohol independently to get baseline activity and selectivity data for the intermediate product. For molecules with a single aldehyde functional group, the only product from this reaction in the region prior to OER onset will be the $2e^-$ carboxylic acid product making this system more feasible to analyze as a primary test system. Data collected over a range of rotation rates at specific potentials allows for determination of the kinetically limiting current through Koutecky-Levich analysis. Once the kinetic information is obtained for an aldehyde this information can be used as a background reaction occurring at the electrode, modeled as a function of current, to correct for the production carboxylic acids during alcohol oxidation, allowing for the determination of kinetic parameters in the oxidation of the alcohol itself. This analysis is still nontrivial as factors such as substrate diffusion away from the electrode surface, substrate concentration within the stagnant layer, and substrate solubility will play a major factor in reactivity and will likely need to be modeled as a function of the measured current.

I hypothesize that the first oxidation (alcohol to aldehyde) will be kinetically slower when compared to the second oxidation (aldehyde to carboxylic acid) at the potentials in question. This is suggested by the relative product distribution of aldehydes and acids for all alcohols tested and for n-butanol at all potentials tested. If true, this hypothesis suggests that it is difficult to achieve a product distribution that favors the presence of the two-electron oxidation product explaining the most oxidized product being observed commonly in the AOR literature.[7-9] These kinetic studies

will pioneer these types of studies within the AOR field, as well as generate data which can be used to develop routes to selectively produce one product over the other.

5.5 Expanding AOR Substrate Scope

Altering the identity of the added alcohol offers the ability to produce both new and interesting products, as well generate systems which operate at higher current densities at less positive potentials. Substrate scope studies are commonplace in the organic chemistry literature highlighting products formed and the same principles followed can be used in the electrical AOR system. The analysis in the AOR system however must extend beyond product selectivity to include activity metrics as well to highlight the specific current density as a key metric which is lost in the modern organic electrochemistry community. For our system the ability to predict activity trends is low due to the simplicity of the substrates used so far, so moving forward modifications of the alcohols in systematic ways will allow for the roles of thermodynamics and kinetics can be discerned for a variety of systems, allowing for further understanding of possible substrates with high activity and selectivity.

The specific alcohols that we will test for both increased activity and increased selectivity will fall in to two groups. The first group consists of alkyl alcohols, where modifications to the carbon backbone to increase the hydrodynamic radius of the molecule or alter the electronics of the molecule to observe how size and electronics alter both the activity and selectivity during alcohol oxidation. Specific modifications will use halogenated and methylated butanol substrates, both groups which will not be directly oxidized by the polarized electrode but will alter the size and relative electron density at the hydroxyl group. The expectation of this study is through increasing the steric bulk of the alcohol substrate by addition of functional groups, it will become more difficult kinetically to oxidize the alcohol group, thus decreasing the observed current

density. I expect this effect to be independent of any alterations in thermodynamic potential as the onset for alcohol oxidation appears to coincide with the $Co^{3+/4+}$ redox couple and not the thermodynamic potential of the substrate. Large functional groups should limit the ability for the alcohol to interact with the electrode surface, decreasing the probability for an electrode-based reaction to occur. Additionally, the position of the bulkier functional group will affect activity, with groups further away from the hydroxyl group showing less AOR activity. As far as electronics are concerned, removal of electron density will alter the kinetically limited current density of the substrate. These studies will be completed with both product analysis as well as determination of the kinetically limited currents through methods used in section 5.4, to find the metrics that best describe an active and selective substrate material.

The second group of alcohols that should be tested are diols and triols. These systems introduce the ability to produce a wide range of products, which complicates product analysis as well as determining kinetic parameters. There is some evidence of activity for these complex systems in the literature, with glycerol being a major target molecule for study due to its presence as a bioremediation product. However, the complexity of the triol system which can generate eight possible products even before accounting for the possibility of carbon-carbon bond cleavage, makes this a difficult starting system. To begin these studies, simpler diol systems will be studied, and the product distributions determined. These would begin with 1,3 butanediol and 1,4 butanediol. The expectation for these systems is that the major product observed will be the most oxidized species, for the 1,4 butanediol this would be the diacid product where the 1,3-butanediol would give the $6e^-$ acid, ketone product. This expectations is based off the high charge efficiency for butyric acid in butanol oxidation as well as the high efficiency for the acid products in other systems. The effects of alcohol proximity will be tested with the 1,2 butanediol which can be

compared to the activity and selectivity of the 1,3-butanediol system, as well as give vital information for the types of products that might be expected in glycerol oxidation. Following the results of these studies, glycerol oxidation will be performed, focusing on the rate of production for the specific products produced. This is a much more complex system than the simpler primary alcohol systems for kinetic studies due to the presence of a significant number of possible intermediates.

The completion of these studies will greatly influence the field of alcohol oxidation, by furthering the fundamental understandings in what makes a good and active substrate for aqueous AOR. By increasing the fundamental knowledge in this field though these studies, we can use the knowledge gained to predict new target molecules which may either greatly increase the activity at the anode or generate a highly valued product. Additionally, through understanding of product formation rates, and kinetic parameters from a range of substrates, methods to produce specific products electrocatalytically can be developed within this system.

5.6 Doping Effects for Alcohol Oxidation

Doped cobalt oxides, using metals such as iron, chromium, copper, and magnesium offer the ability to increase the activity of the AOR system similarly to how they alter the OER activity. The major effect that will be key in determining the initial activity for these systems for AOR, is the possibility of shifting the $Co^{3+/4+}$ redox couple in the system to facilitate the activation of AOR mechanism, while also increasing the susceptibility for nucleophilic attack by the alcohol. Transition metals such as Cu being added to the system should assist in moving the redox couple thus increasing AOR activity similar to Ni dopants. Other metals such as iron and chromium which have shown to shift the $Co^{3+/4+}$ couple more positive, we would expect to decrease the AOR activity making these systems have catalytic onsets at potentials similar to oxygen evolution, thus

limiting product formation in AOR. Preliminary studies on Cr and Fe doped cobalt oxides for activity metrics show limited activity increases upon addition of benzyl alcohol to the electrolyte, however due to the difficulty in analyzing product distributions with benzyl alcohol, product distributions are inconclusive. For these systems, due to the shift in the redox couple, it is likely that a larger potential dependent product formation occurs, due to the preferential oxidation of aldehydes prior to the $Co^{3+/4+}$ couple.[10]

Preliminary screening with synthesized materials should screen for OER and AOR using a butanol system for initial activity through cyclic voltammetry. These initial screens will cover both OER and AOR as these experiments can be done on the same electrodes sequentially. Once preliminary activity metrics are recorded for a range of metal doped species is collected, the more active of the systems will be tested for product distributions to see how potential alters the product formation across a range of dopant species. Additionally, samples should be checked for product formation after OER onset to observe if on different materials the kinetics of OER are sluggish enough to increase the relative formation of alcohols at more positive applied potentials. Through determination of product distributions, I expect that some materials will preferentially produce aldehydes, showing that through catalyst modification the reaction selectivity can be fine-tuned to receive a desired product with electrochemical AOR.

The completion of these studies coupled with kinetic studies as outlined in section 5.4, will allow for a greater understanding on what makes AOR catalysts both active for the AOR and selective for specific products in the AOR. These findings will allow for future processes to be developed that will be able to produce selective products, over a wide range of alcohols, with high activity, creating a system that is viable for industrial use as an anodic reaction in the production of hydrogen gas.

5.7 References

1. C.-C. Lin and C. C. L. McCrory, *ACS Catalysis*, 2017, **7**, 443-451.
2. A. Badruzzaman, A. Yuda, A. Ashok and A. Kumar, *Inorganica Chimica Acta*, 2020, **511**, 119854.
3. R. D. L. Smith, M. S. Prévot, R. D. Fagan, S. Trudel and C. P. Berlinguette, *Journal of the American Chemical Society*, 2013, **135**, 11580-11586.
4. M. S. Burke, M. G. Kast, L. Trotochaud, A. M. Smith and S. W. Boettcher, *Journal of the American Chemical Society*, 2015, **137**, 3638-3648.
5. T. Zhang, M. R. Nellist, L. J. Enman, J. Xiang and S. W. Boettcher, *ChemSusChem*, 2019, **12**, 2015-2021.
6. C. Costentin and J.-M. Savéant, *Proceedings of the National Academy of Sciences*, 2019, **116**, 11147.
7. Z. Yin, Y. Zheng, H. Wang, J. Li, Q. Zhu, Y. Wang, N. Ma, G. Hu, B. He, A. Knop-Gericke, R. Schlögl and D. Ma, *ACS Nano*, 2017, **11**, 12365-12377.
8. Y. Cao, D. Zhang, X. Kong, F. Zhang and X. Lei, *Journal of Materials Science*, 2021, **56**, 6689-6703.
9. Y. Yang and T. Mu, *Green Chemistry*, 2021, DOI: 10.1039/D1GC00914A.
10. X. Deng, G.-Y. Xu, Y.-J. Zhang, L. Wang, J. Zhang, J.-F. Li, X.-Z. Fu and J.-L. Luo, *Angewandte Chemie International Edition*, 2021, **n/a**.

Appendices A Supporting Information

A.1 Supporting Information for Chapter 2

A.1.1 Supporting Figures

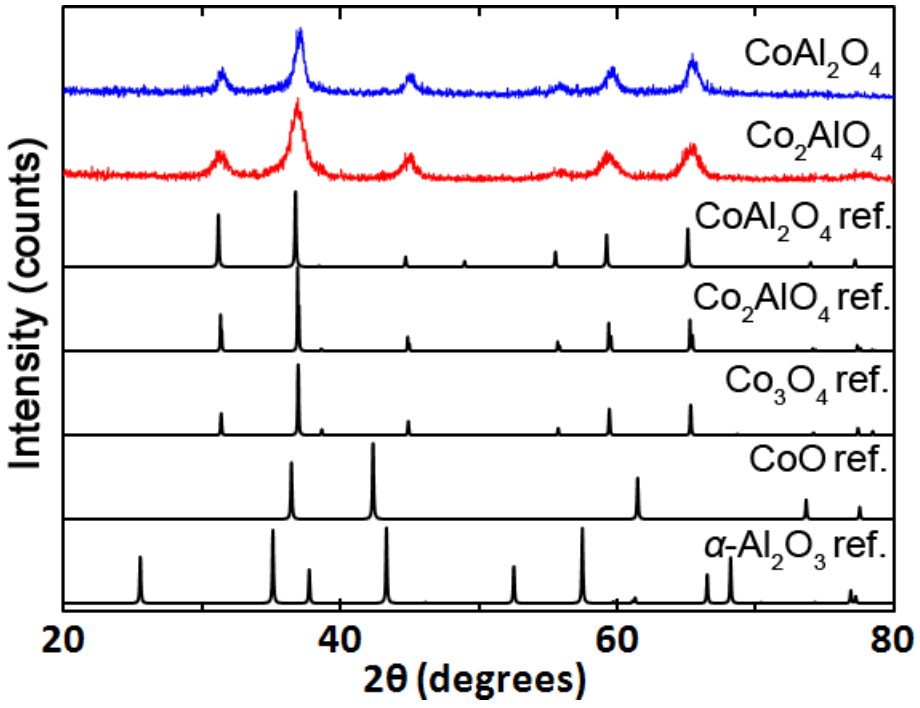

Figure A.1 PXRD data for the $Co_{3-x}Al_xO_4$ series

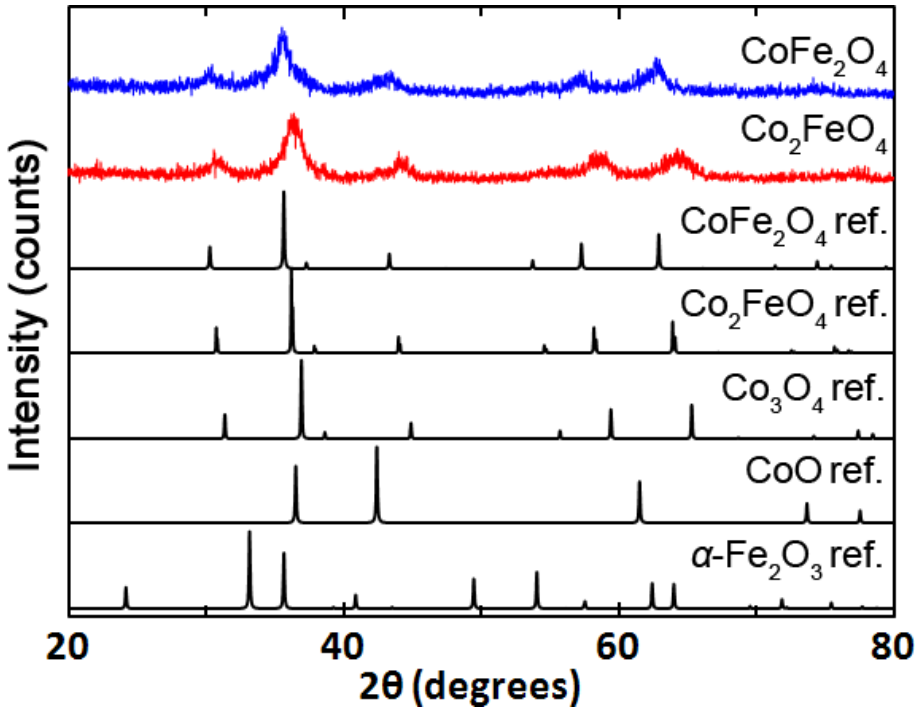

Figure A.2 PXRD data for the $Co_{3-x}Fe_xO_4$ series

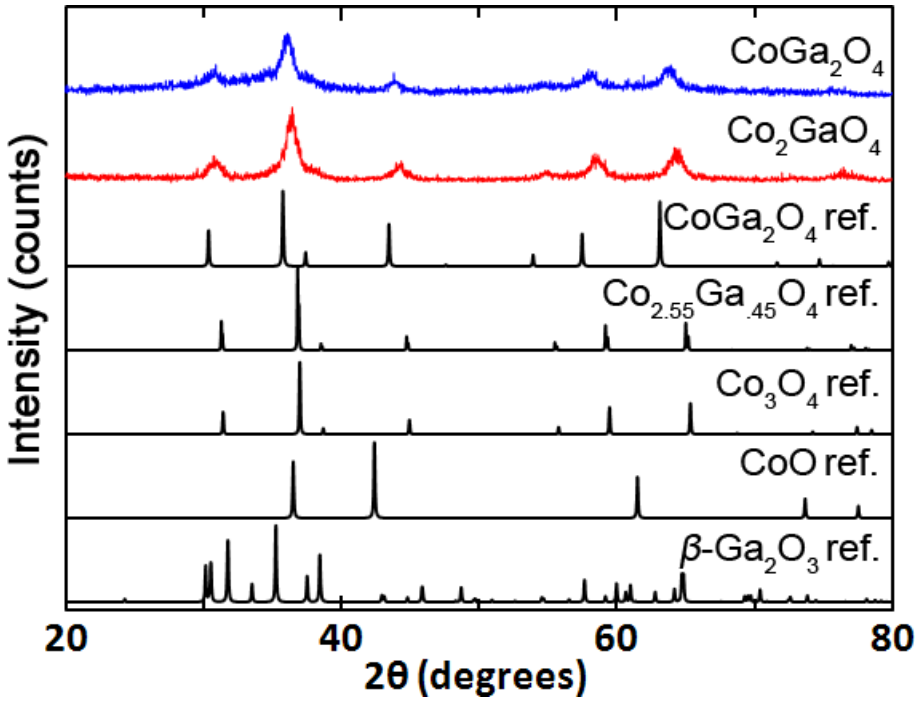

Figure A.3 PXRD data for the $Co_{3-x}Ga_xO_4$ series

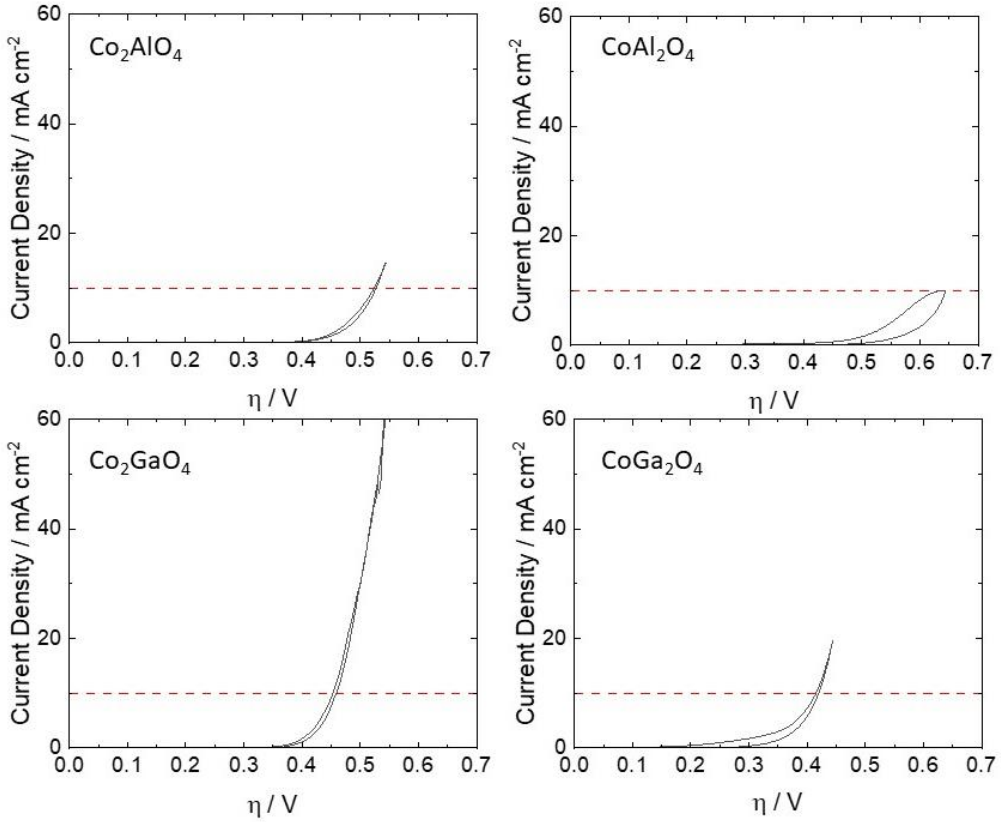

Figure A.4 Representative RDEVs of Al and Ga doped $Co_{3-x}M_xO_4$ samples in O_2-sparged 1 M NaOH with a rotation rate of 1600 rpm using Hg/HgO reference electrode. The red dash line shows current density at 10 mA/cm^2.

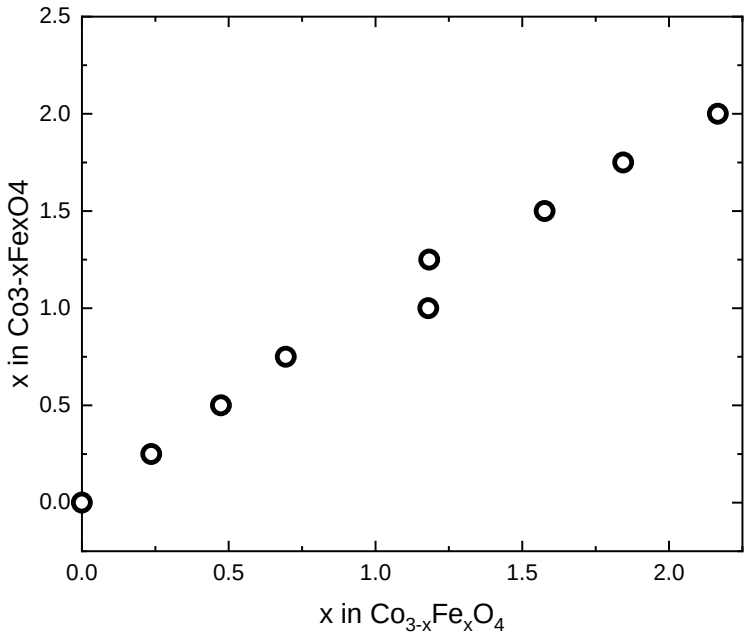

Figure A.5 Correlation between ICP calculated iron concentration and the empirical iron concentration relative to cobalt concentrations showing good agreement between the synthesized ratios, to those found in dissolved particles analyzed for metal content

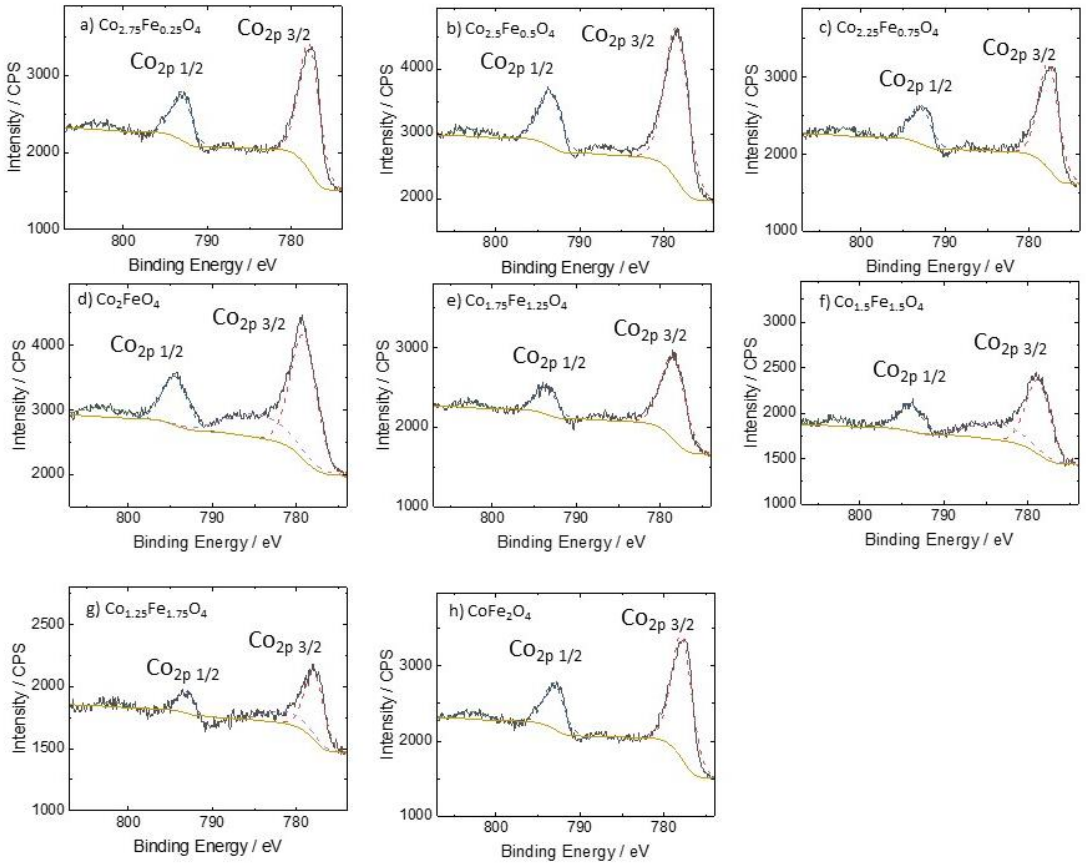

Figure A.6 Shows the cobalt XPS for (a) $Co_{2.75}Fe_{0.25}O_4$, (b) $Co_{2.5}Fe_{0.5}O_4$, (c) $Co_{2.25}Fe_{0.75}O_4$, (d) Co_2FeO_4, (e) $Co_{1.75}Fe_{1.25}O_4$, (f) $Co_{1.5}Fe_{1.5}O_4$, (g) $Co_{1.25}Fe_{1.75}O_4$ (h) $CoFe_2O_4$ powders.

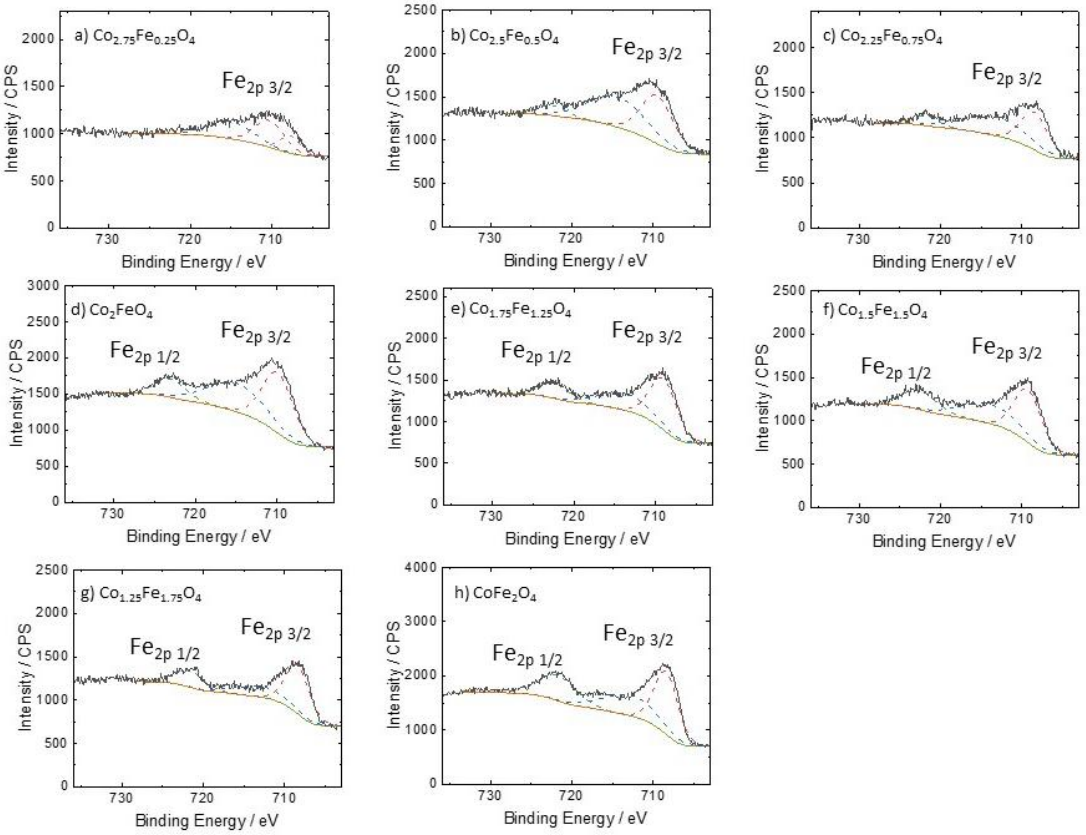

Figure A.7 Shows the Iron XPS for (a) $Co_{2.75}Fe_{0.25}O_4$, (b) $Co_{2.5}Fe_{0.5}O_4$, (c) $Co_{2.25}Fe_{0.75}O_4$, (d) Co_2FeO_4, (e) $Co_{1.75}Fe_{1.25}O_4$, (f) $Co_{1.5}Fe_{1.5}O_4$, (g) $Co_{1.25}Fe_{1.75}O_4$ (h) $CoFe_2O_4$ powders.

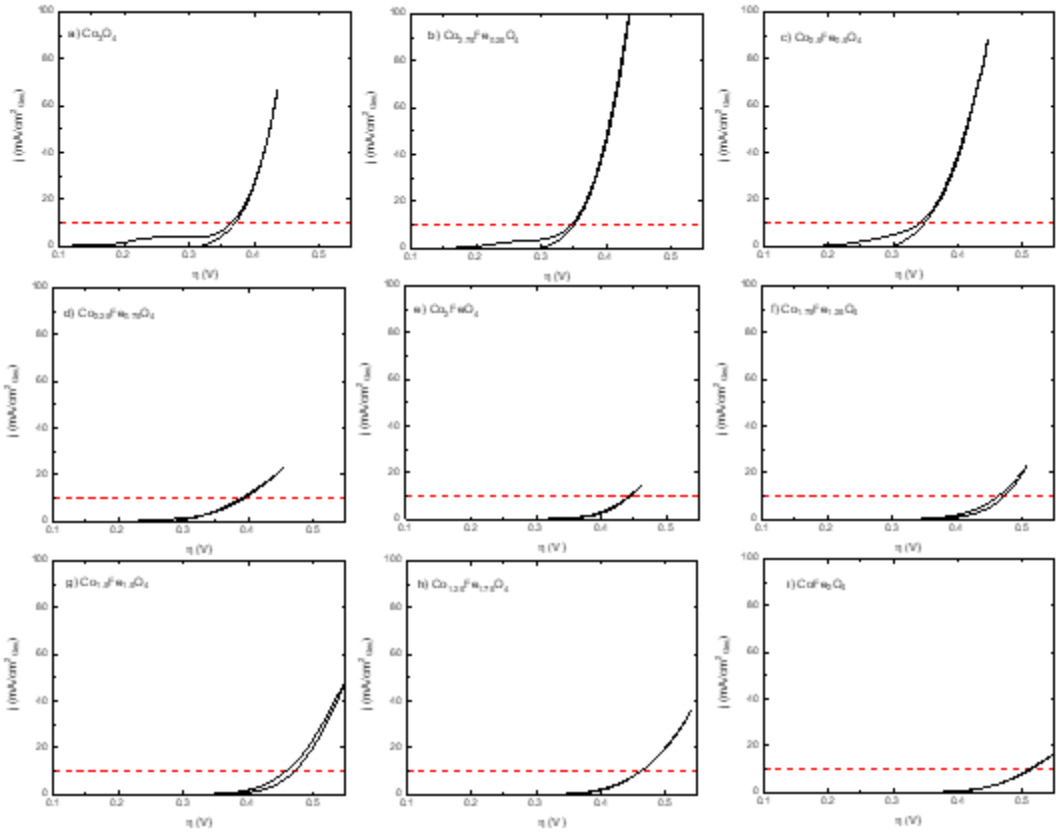

Figure A.8 Representative RDEVs of (a) Co_3O_4, (b) $Co_{2.75}Fe_{0.25}O_4$, (c) $Co_{2.5}Fe_{0.5}O_4$, (d) $Co_{2.25}Fe_{0.75}O_4$, (e) Co_2FeO_4, (f) $Co_{1.75}Fe_{1.25}O_4$, (g) $Co_{1.5}Fe_{1.5}O_4$, (h) $Co_{1.25}Fe_{1.75}O_4$ (i) $CoFe_2O_4$ in O_2-sparged 1 M NaOH with a rotation rate of 1600 rpm using Hg/HgO reference electrode. The red dash line shows current density at 10 mA/cm^2.

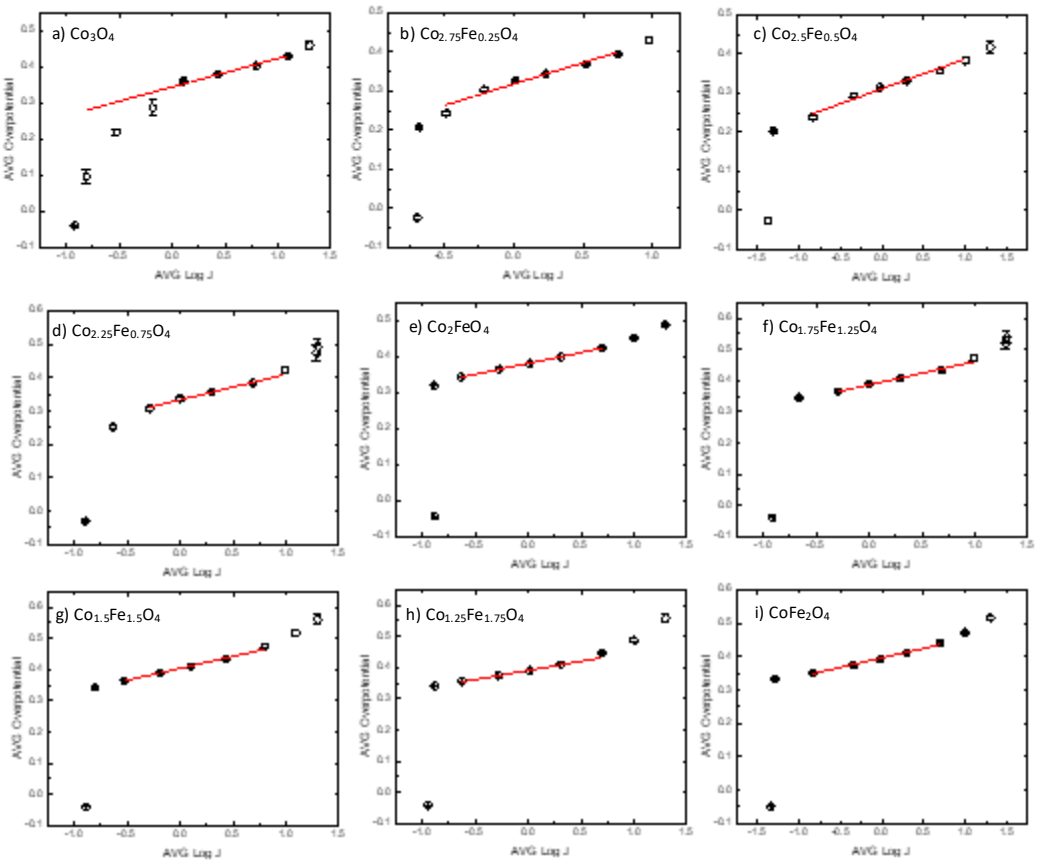

Figure A.9 Tafel Plots for (a) Co_3O_4, (b) $Co_{2.75}Fe_{0.25}O_4$, (c) $Co_{2.5}Fe_{0.5}O_4$, (d) $Co_{2.25}Fe_{0.75}O_4$, (e) Co_2FeO_4, (f) $Co_{1.75}Fe_{1.25}O_4$, (g) $Co_{1.5}Fe_{1.5}O_4$, (h) $Co_{1.25}Fe_{1.75}O_4$ (i) $CoFe_2O_4$ in O_2-sparged 1 M NaOH with rotator rate of 1600 rpm using Hg/HgO reference electrode. Tafel slope data was collected by recording the overpotential after 30s chronoamperometric steps following cyclic voltammetry measurements. The first data point was omitted from the Tafel slop calculations for each catalyst.

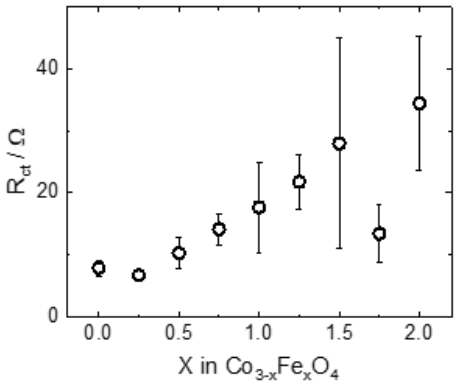

Figure A.10 Plot of the charge transfer resistance as a function of iron content. EIS data was collected about 1.6V applied vs RHE within the region where OER activity will occur, with limited bubble formation.

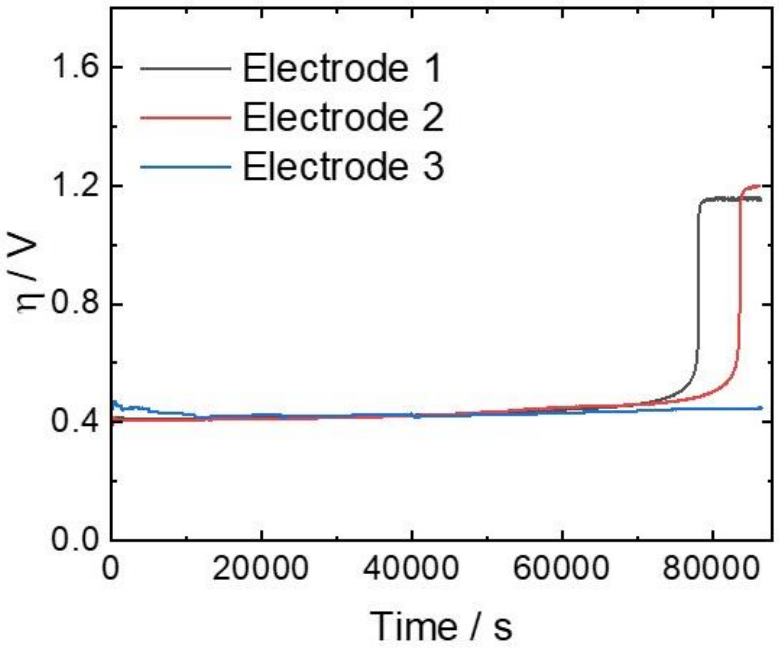

Figure A.11 Raw controlled current data for $Co_{2.75}Fe_{0.25}O_4$ catalysts over 24 hours showing the catastrophic delamination for electrodes one and two evident by the large decrease in OER activity.

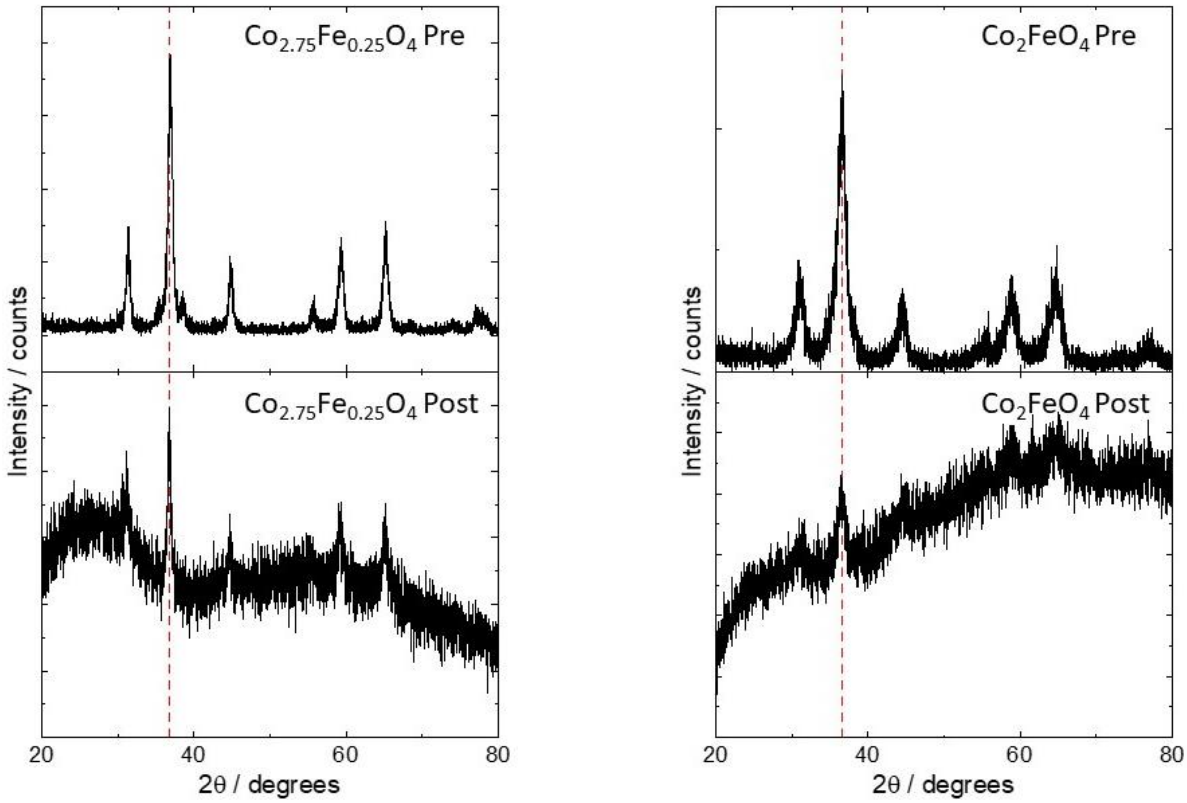

Figure A.12 Before and after electrolysis XRD for both $Co_{2.75}Fe_{0.25}O_4$ (left) and Co_2FeO_4 (right) showing crystalline stability of the lattice during the duration of electrochemical measurements. Red lines are added at the peak position of the (311) peak in the materials before electrolysis to highlight possible shifts in peak position.

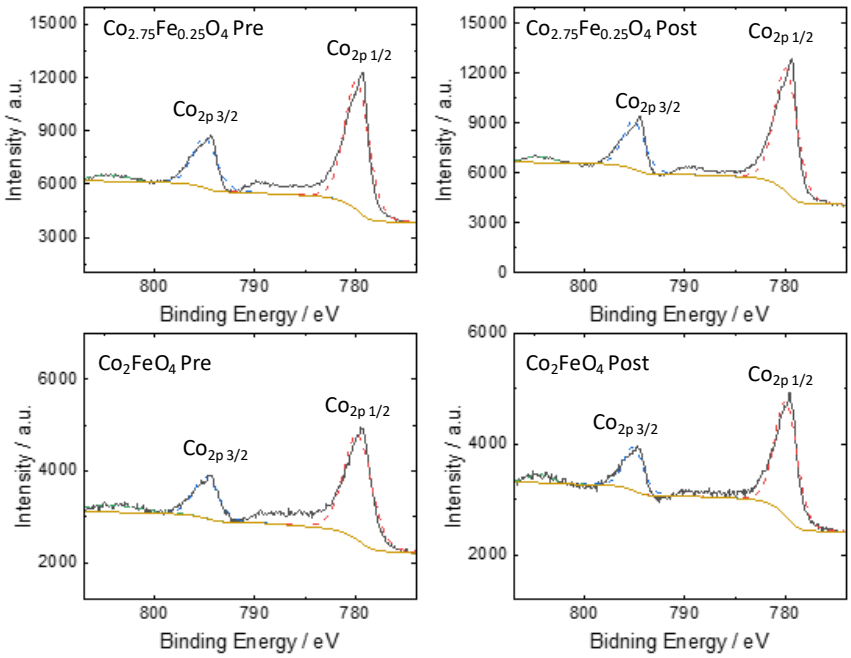

Figure A.13 Cobalt XPS of $Co_{2.75}Fe_{0.25}O_4$ (upper) and Co_2FeO_4 (lower) both before (left) and after (right) controlled current stability measurements at 10mA*cm^{-1} current density for 20hrs.

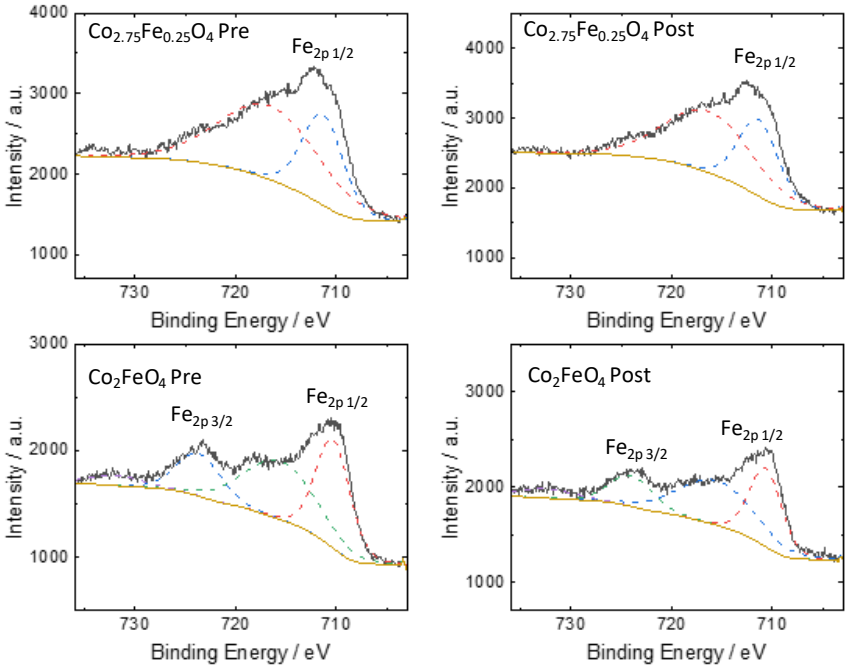

Figure A.14 Iron XPS of $Co_{2.75}Fe_{0.25}O_4$ (upper) and Co_2FeO_4 (lower) both before (left) and after (right) controlled current stability measurements at 10mA*cm^{-1} current density for 20hrs

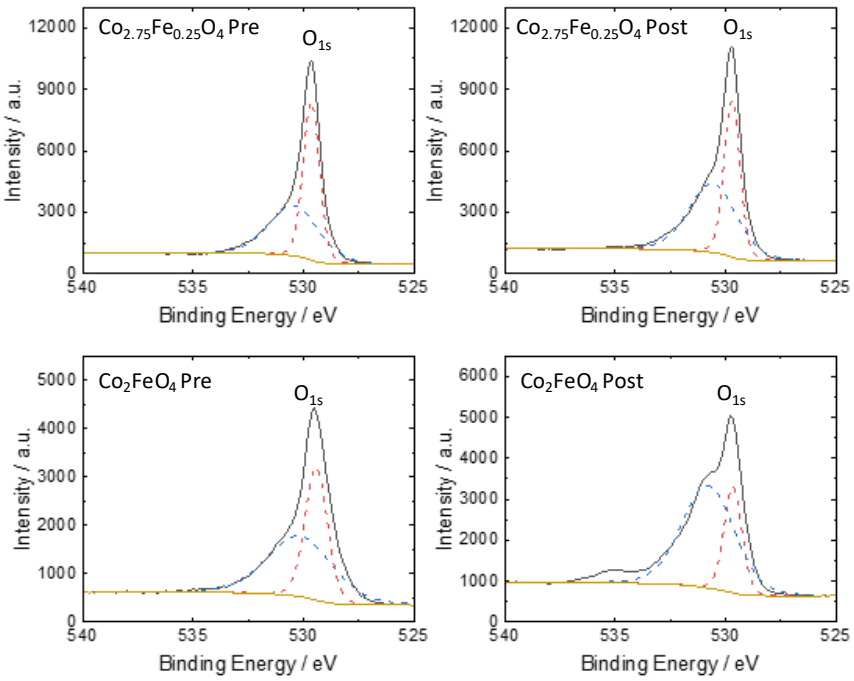

Figure A.15 Oxygen XPS of $Co_{2.75}Fe_{0.25}O_4$ (upper) and Co_2FeO_4 (lower) both before (left) and after (right) controlled current stability measurements at 10mA*cm^{-1} current density for 20hrs

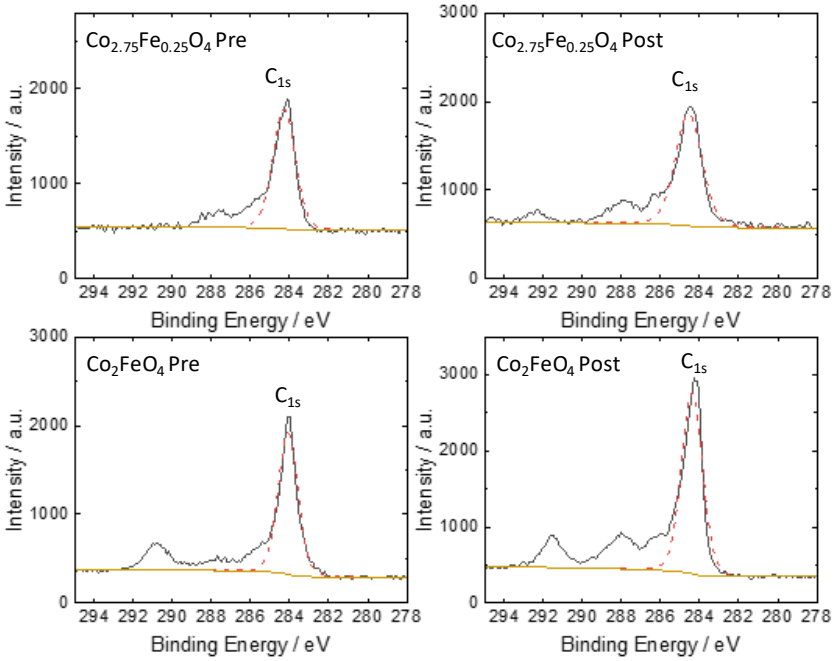

Figure A.16 Carbon XPS of $Co_{2.75}Fe_{0.25}O_4$ (upper) and Co_2FeO_4 (lower) both before (left) and after (right) controlled current stability measurements at 10mA*cm^{-1} current density for 20hrs

A.1.2 Supporting Tables

Table A.1 Material characterization data for the catalysts synthesized in Chapter 2

Catalyst	nominal Co/M	Co/M[a]	Lattice parameter (Å)[b]	S_{BET} (m^2/g)
Co_3O_4	-	-	8.080[c]	41.54 ± 0.94[c]
Co_2AlO_4	2	1.91	8.064	126.68 ± 1.50
Co_2GaO_4	2	2.26	8.167	88.62 ± 0.20
Co_2FeO_4	2	1.88 (1.95)[b]	8.188	225.62 ± 0.67
Co_2CrO_4	2	1.93[c]	8.203[c]	40.11 ± 0.90[c]
$CoAl_2O_4$	0.5	0.52	8.031	72.67 ± 3.83
$CoGa_2O_4$	0.5	0.55	8.254	41.56 ± 0.86
$CoCr_2O_4$	0.5	0.49[c]	8.285[c]	104.67 ± 0.48[c]
$CoFe_2O_4$	0.5	0.43	8.376	132.36 ± 1.14
$Co_{2.75}Fe_{0.25}O_4$	11	11.68 (10.51)[b-]	8.070	116.98 ± 3.60
$o_{2.5}Fe_{0.5}O_4$	5	5.33	8.074	91.36 ± 4.19
$Co_{2.25}Fe_{0.75}O_4$	3	3.32	8.112	100.97 ± 3.80
$Co_{1.75}Fe_{1.25}O_4$	1.4	1.54	8.170	231.54 ± 3.54
$Co_{1.5}Fe_{1.5}O_4$	1	0.90	8.200	307.75 ± 3.40
$Co_{1.25}Fe_{1.75}O_4$	0.71	0.63	8.308	135.84 ± 3.61

[a] Determined from ICP-MS
[b] Denotes measurement obtained after electrochemical experiments
[c] Calculated from PXRD (311) peak
[d] From previous publication[1]

Table A.2 All measured activity metrics for catalysts tested in Chapter 2. Included values are overpotential at 10mA/cm$^2_{geo}$, current density per geometric and BET normalized surface area at 350mV overpotential.

Catalyst	$\eta_{j=10mA/cm^2_{geo,t=0}}$ (V)[a]	$j_{s,\eta=350mV,geo}$ (mA/cm^2)[b]	$j_{s,\eta=350mV,BET}$ (μA/cm$^2_{BET}$)[b]	Tafel slope (mV/dec)
Co_3O_4	0.42 ± 0.01	0.42 ± 0.11	1.20 ± 0.31	52 ± 3
$CoAl_2O_4$	0.54 ± 0.03	0.064 ± 0.026	0.061 ± 0.025	59 ± 2
$CoGa_2O_4$	0.41 ± 0.01	1.47 ± 0.36	4.39 ± 1.23	65 ± 5
$CoCr_2O_4$	0.40 ± 0.03[c]	2.45 ± 0.64[c]	2.77 ± 0.72[c]	87 ± 16[c]
CoV_2O_4	0.37 ± 0.01[d]	2.44 ± 0.48[d]	368 ± 73[d]	52 ± 3[d]
Co_2AlO_4	0.46 ± 0.01	0.46 ± 0.06	0.77 ± 0.10	62 ± 1
Co_2GaO_4	0.50 ± 0.02	0.063 ± 0.019	0.086 ± 0.025	67 ± 7
Co_2CrO_4	0.37 ± 0.01[c]	4.01 ± 1.16[c]	11.78 ± 3.41[c]	56 ± 5[c]
$Co_{2.75}Fe_{0.25}O_4$	0.36 ± 0.01	8.70 ± 0.49	2.87 ± 0.46	109 ± 13
$Co_{2.5}Fe_{0.5}O_4$	0.36 ± 0.01	6.70 ± 1.60	8.78 ± 0.49	76 ± 6
$Co_{2.25}Fe_{0.75}O_4$	0.42 ± 0.01	1.58 ± 0.24	8.65 ± 2.11	76 ± 6
Co_2FeO_4	0.44 ± 0.01	0.33 ± 0.01	1.85 ± 0.28	60 ± 1
$Co_{1.75}Fe_{1.25}O_4$	0.48 ± 0.01	0.15 ± 0.02	0.17 ± 0.01	74 ± 5
$Co_{1.5}Fe_{1.5}O_4$	0.49 ± 0.01	0.18 ± 0.03	0.08 ± 0.01	77 ± 3
$Co_{1.25}Fe_{1.75}O_4$	0.45 ± 0.01	0.17 ± 0.06	0.07 ± 0.01	59 ± 4
$CoFe_2O_4$	0.46 ± 0.01	0.17 ± 0.02	0.15 ± 0.04	56 ± 3

[a] Overpotentials were calculated from CV scans and chronoamperometry measurements (j = 10 mA/cm^2).

[b] Current densities were calculated from CV scans and chronopotentiometry measurements (η = 0.350 V).

[c] From previous publication[1]

[d] From previous publication[2]

Table A.3 XPS peaks for synthesized $Co_{3-x}Fe_xO_4$ materials for both Co and Fe high resolution XPS measurements.

Material	Binding Energy (eV)			
	$Co_{2p\ 3/2}$	$Co_{2p\ 1/2}$	$Fe_{2p\ 3/2}$	$Fe_{2p\ 1/2}$
$CoFe_2O_4$	779.96	795.3	710.4	723.8
$Co_{1.25}Fe_{1.75}O_4$	779.8	795.3	710.5	723.5
$Co_{1.5}Fe_{1.5}O_4$	780.7	794	711.3	724.5
$Co_{1.75}Fe_{1.25}O_4$	780.4	795.7	710.9	724.5
Co_2FeO_4	779.1	794.4	711.8	725
$Co_{2.25}Fe_{0.75}O_4$	779.7	794.8	710.4	723.8
$Co_{2.5}Fe_{0.5}O_4$	780.4	795.6	711.4	724.3
$Co_{2.75}Fe_{0.25}O_4$	779.8	795.1	710.9	n.a.

Table A.4 XPS peaks for XPS peak table for post-mortem material analysis for both $Co_{2.75}Fe_{0.25}O_4$ and Co_2FeO_4 catalysts.

	$Co_{2p\ 3/2}$	$Co_{2p\ 1/3}$	$Fe_{2p\ 3/2}$	$Fe_{2p\ 1/2}$	O_{1s}
$Co_{2.75}Fe_{0.25}O_4$ Pre	779.9	794.9	711.4	N.A.	529.6
$Co_{2.75}Fe_{0.25}O_4$ Post	779.9	795.0	711.4	N.A.	529.7
Co_2FeO_4 Pre	779.7	794.8	710.3	723.7	529.4
Co_2FeO_4 Post	779.9	795.1	710.7	724.1	529.6, 530.8

Table A.5 Activity Comparison to other catalysts in literature

Catalyst	$\eta_{j=10mA/cm^2_{geo}}$ (V)[a]	$j_{s,\eta=350mV,geo}$ (mA/cm^2)[a]	$j_{s,\eta=350mV,BET}$ (μA/cm$^2_{BET}$)[a]	$j_{s,\eta=350mV,mass}$ (A/g)	Ref
Co_3O_4	0.42 ± 0.01	0.42 ± 0.11	1.2 ± 0.3	0.5 ± 0.1	This Work
$Co_{2.75}Fe_{0.25}O_4$	0.36 ± 0.01	8.70 ± 0.49	2.87 ± 0.46	10.4 ± 0.6	This Work
$Co_{2.25}Cr_{0.75}O_4$	0.35 ± 0.01	8.84 ± 2.7	14.06 ± 4.28	10.6 ± 3.2	[1]
$Ba_{0.5}Sr_{0.5}Co_{0.8}Fe_{0.2}O_{3-\delta}$	N.R.	~20[b]	~40[b]	~10[b]	[3]
Exfoliated NiFe LDH	~0.3	~9[c]	N.R.	~29[c]	[4]
$Ni_{0.9}Fe_{0.1}O_x$	0.336	1.24 ± 0.04	N.R.	1065 ± 129[c]	[5]
IrO_2	0.38 ± 0.01	2.23 ± 1.15	0.007 ± 0.003	2.8 ± 0.4	[6]
FeNiCoP	0.259	N.R.	N.R.	N.R.	[7]
Co-Ni-Fe_{511}	0.288	N.R.	N.R.	N.R.	[8]
$SrCo_{0.8}Fe_{0.2}O_3$	0.42	N.R.	N.R.	N.R.	[9]

A.1.3 References

1. C.-C. Lin and C. C. L. McCrory, *ACS Catalysis*, 2017, **7**, 443-451.
2. S. E. Michaud, M. T. Riehs, W.-J. Feng, C.-C. Lin and C. C. L. McCrory, *Chemical Communications*, 2021, **57**, 883-886.
3. J. Suntivich, K. J. May, H. A. Gasteiger, J. B. Goodenough and Y. Shao-Horn, *Science*, 2011, **334**, 1383-1385.
4. F. Song and X. Hu, *Nat Commun*, 2014, **5**, 4477.
5. L. Trotochaud, J. K. Ranney, K. N. Williams and S. W. Boettcher, *J. Am. Chem. Soc.*, 2012, **134**, 17253-17261.
6. S. Jung, C. C. L. McCrory, I. M. Ferrer, J. C. Peters and T. F. Jaramillo, *Journal of Materials Chemistry A*, 2016, **4**, 3068-3076.

7. K. Zhan, C. Feng, X. Feng, D. Zhao, S. Yue, Y. Li, Q. Jiao, H. Li and Y. Zhao, *ACS Sustainable Chemistry & Engineering*, 2020, **8**, 6273-6281.
8. G. Zeng, M. Liao, C. Zhou, X. Chen, Y. Wang and D. Xiao, *RSC Advances*, 2016, **6**, 42255-42262.
9. Y. Da, L. Zeng, C. Wang, C. Gong and L. Cui, *Electrochimica Acta*, 2019, **300**, 85-92.

A.2 Supporting information for Chapter 3

A.2.1 Supporting figures

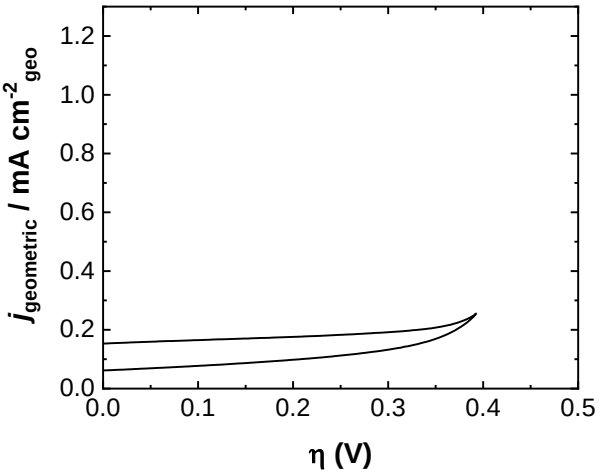

Figure A.17 Representative cyclic RDEV of V_2O_3 in 1 M NaOH in the potential window used for the OER studies in this report. The V_2O_3 system shows no evidence of OER activity under the conditions used in this study. The RDEVs shown is the 2nd cycle for V_2O_3.

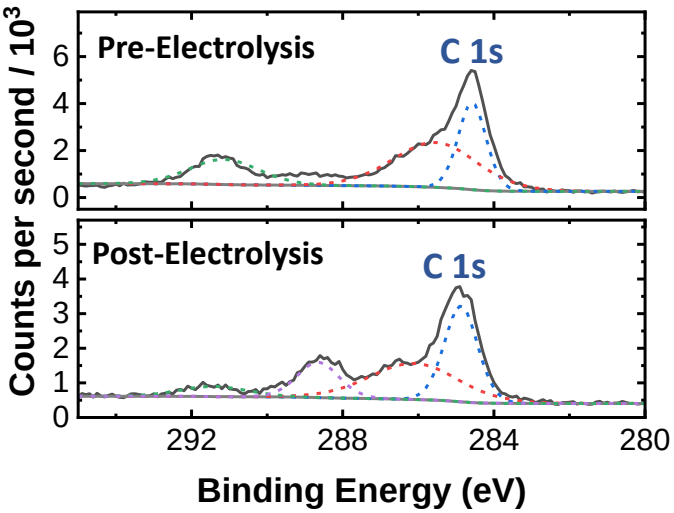

Figure A.18 High resolution XPS spectra of CoV_2O_4 both as-synthesized and after 28-h electrolysis in the C 1s region.

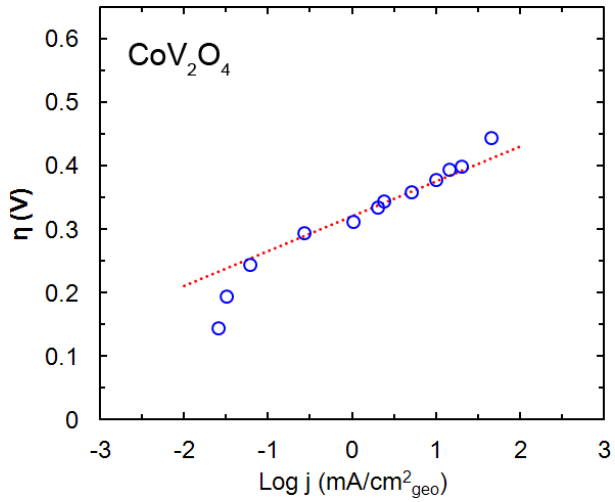

Figure A.19 Representative Tafel plot of CoV_2O_4 in O_2-purged 1 M NaOH with rotation rate of 1600 rpm. The linear regression region was chosen near the j = 10 mA/cm^2_{geo}. The Tafel slope is 52 ± 3.

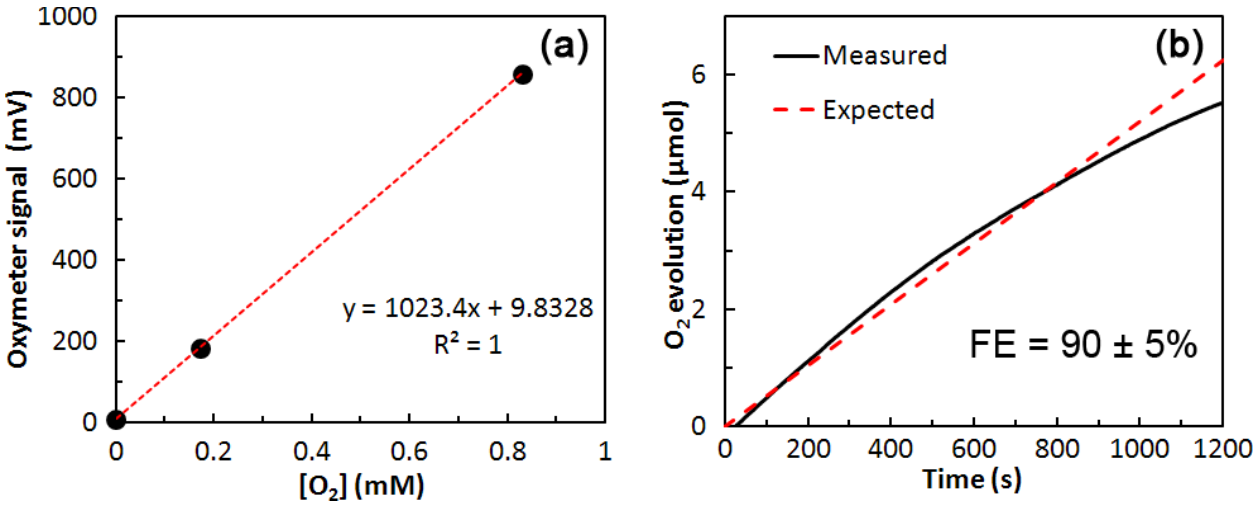

Figure A.20(a) Three-point calibration curve for the oxygen meter and (b) the time-dependent measurement of O_2 evolved by CoV_2O_4. The dashed red line is the expected amount of O_2 evolved based on charge passed, and the solid black line is the amount of O_2 measured. The Faradaic efficiency was calculated based on the total O_2 produced at the end of the experiment divided by the expected amount of O_2 based on total charge passed.

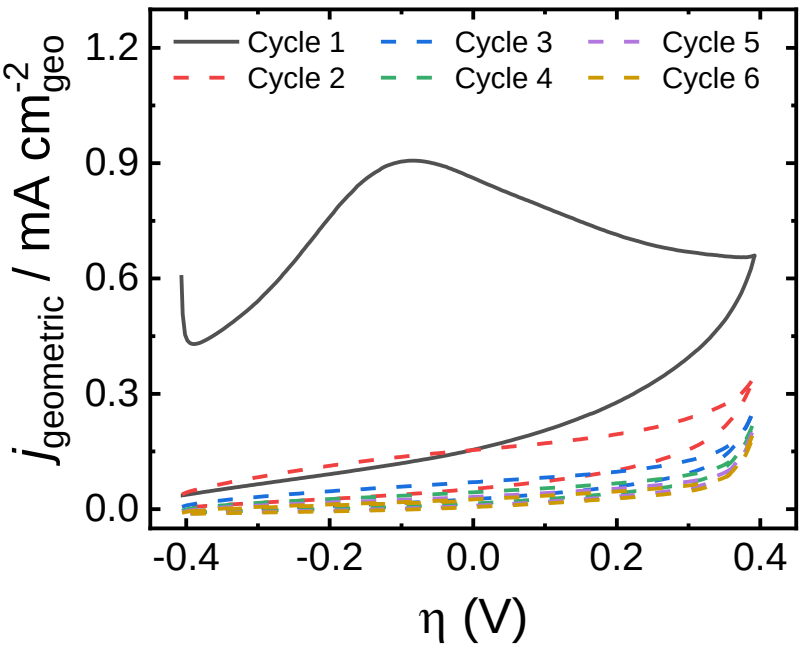

Figure A.21 The first six RDEVs measured for V_2O_3 at in O_2-saturated 1 M NaOH at 1600 rpm and 0.1 V/s scan rate. There is a large oxidative peak at $\eta \approx 0.05$ V that decreases substantially in current after the first cycle. This voltammetric behavior is qualitatively similar to that observed in the first six scans of CoV_2O_4 (see Figure 4.2 in the manuscript), and we attribute it to oxidative vanadium etching.

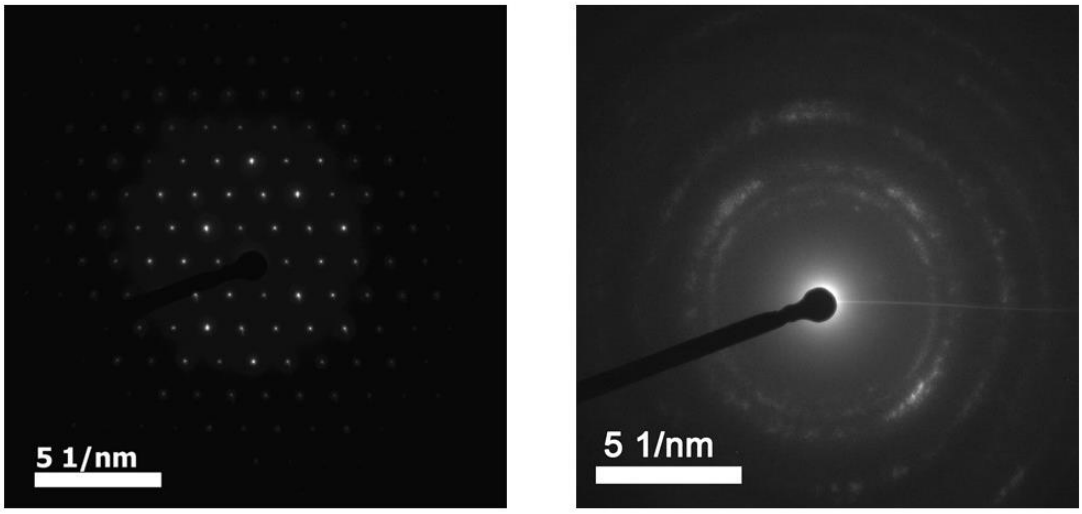

Figure A.22 Representative SAED patterns of CoV_2O_4 before (left) and after (right) constant current measurements showing a transformation from a highly crystalline system before electrolysis to a more amorphous materials after constant current electrolysis.

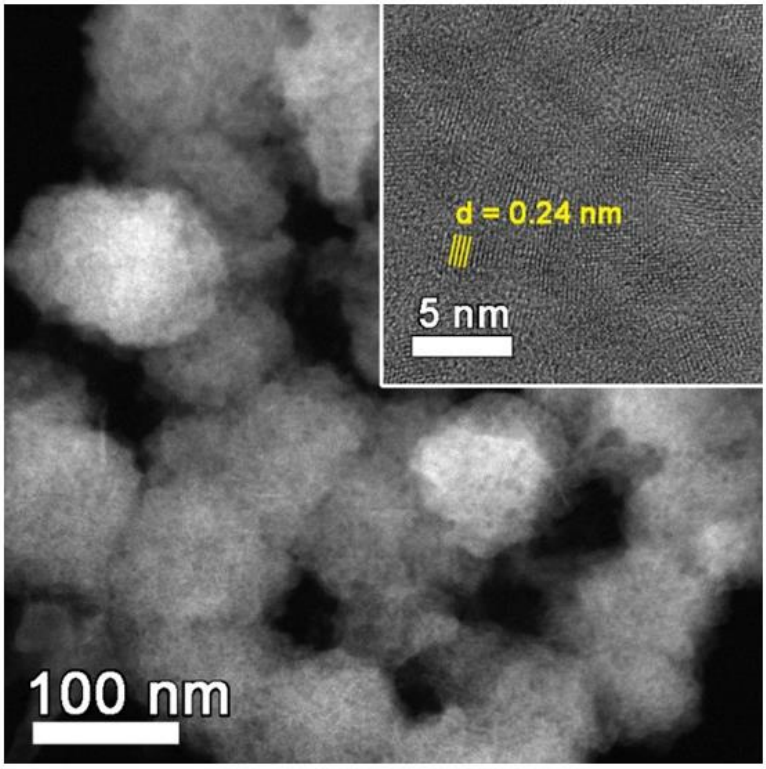

Figure A.23 Zoom in of Figure 3.1c showing CoV_2O_4 after long term stability measurements. Inset shows crystals with lattice fringes measured at 0.24 nm in d-spacing

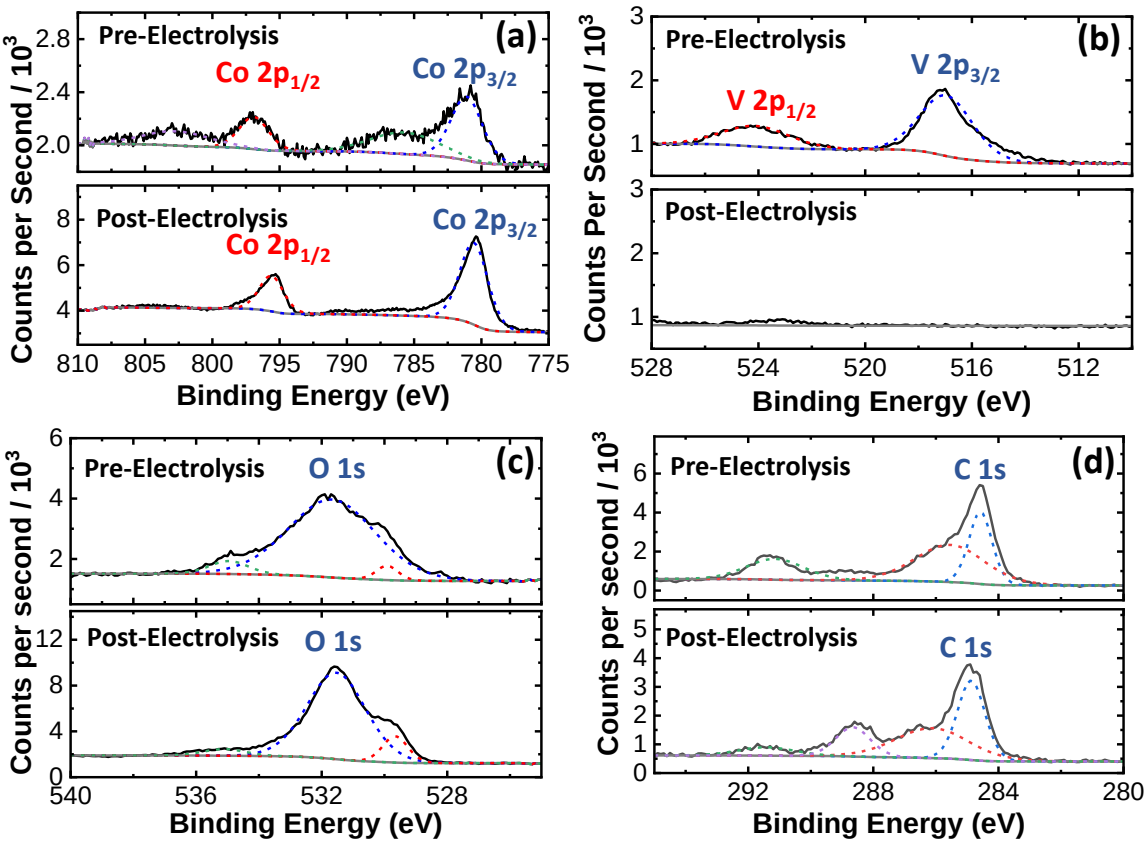

Figure A.24 High resolution XPS spectra of CoV_2O_4 both as-synthesized and after 10,000 cycle stability measurements in the (a) Co 2p region, (b) V 2p region, (c) O 1s region, and (d) C 1s regions.

A.2.2 Supporting Tables

Table A.6 Metal Contents, Lattice Parameters, and BET Surface Areas of as-synthesized Co_3O_4 and CoV_2O_4, and metal content of post-electrolysis CoV_2O_4 (in red).

Catalyst	**Calculated V (atom %)[a]**	**V (atom %) (ICP-MS)**	**V (atom %) (XPS)**	**Lattice parameter (Å)[b]**	**Grain size (nm)[b]**	**S_{BET} (m^2/g)**	V (atom %) (ICP-MS) Post-electrolysis
Co_3O_4[c]	-	-	-	8.080[c]	16.68[c]	41.54 ± 0.94[c]	-
CoV_2O_4	66.7%	64.9%	63.3%	8.380	> 100	0.80 ± 0.13	0.04%

[a]V atom % ratio = $\frac{n_V}{n_{Co}+n_V} \times 100\%$. [b]Calculated from PXRD (311) peak. [c]Data for Co_3O_4 from Reference [1]

Table A.7 OER activity of as-synthesized CoV_2O_4 compared to other OER catalysts. Note that activity metrics are based on the characterization of the as-synthesized CoV_2O_4 material.

Catalyst	**$\eta_{j=10mA/cm^2_{geo}}$ (V)[a]**	**$j_{s,\eta=350mV,geo}$ (mA/cm^2)[a]**	**$j_{s,\eta=350mV,BET}$ ($\mu A/cm^2_{BET}$)[a]**	**$j_{s,\eta=350mV,mass}$ (A/g)**	**Tafel Slope**	**Ref**
CoV_2O_4	**0.37 ± 0.01**	**2.44 ± 0.48**	**368 ± 73**	**2.90 ± 0.57**	**52 ± 3**	**This Work**
Co_3O_4	0.42 ± 0.01	0.42 ± 0.11	1.20 ± 0.31	0.5 ± 0.1	52 ± 3	[1]
$Co_{2.25}Cr_{0.75}O_4$	0.35 ± 0.01	8.84 ± 2.7	14.06 ± 4.28	10.6 ± 3.2	60 ± 3	[1]
$Ba_{0.5}Sr_{0.5}Co_{0.8}Fe_{0.2}O_{3-\delta}$	N.R.	~20[b]	~40[b]	~10[b]	N.R.	[2]
Exfoliated NiFe LDH	~0.3	~9[c]	N.R.	~29[c]	~40	[3]
$Ni_{0.9}Fe_{0.1}O_x$	0.336	1.24 ± 0.04	N.R.	1065 ± 129[c]	30	[4]
V-doped Co_3O_4 [d]	0.29	~90	N.R.	~160	53.3	[5]
V-doped $NiFe_2O_4$ [e]	0.27	~110[c]	N.R.	~200	42.08	[5]
a-CoVOx	0.35	~10	N.R.	69.5	51	[6]
$Ni_3Fe_{0.5}V_{0.5}$	~0.2	~1000[c]	N.R.	~4000[c]	39	[7]
$Co_4V_3Fe_3O_x$	0.307	98.1	N.R.	N.R.	36	[8]
NF@$Co_{1-x}V_x$-HNN	0.268	100	N.R.	N.R.	80	[9]
CoMoV LDH	0.15	N.R.	N.R.	N.R.	106	[10]
$Co_{0.8}V_{0.2}OOH$	0.19	N.R.	N.R.	N.R.	39.6	[11]
$CoV_{1.5}Fe_{0.5}O_4$	~0.3	N.R.	N.R.	N.R.	38	[12]

[a]Metrics were determined and reported primarily from RDEVs or other voltametric measurements. [b]Reported at 400 mV note CoV_2O_4 shows $j_{s,\eta=400mV,geo}$ of 18.4 ± 3.4 (mA/cm^2), $j_{s,\eta=400mV,BET}$ of 2770 ± 511 and $j_{s,\eta=400mV,mass}$ of 21.9 ± 4.0 (A/g). [c]Reported at 300 mV note CoV_2O_4 shows $j_{s,\eta=300mV,geo}$ of 1.88 ± 0.60 (mA/cm^2), $j_{s,\eta=300mV,BET}$ of 283 ± 90 ($\mu A/cm^2_{BET}$) and $j_{s,\eta=300mV,mass}$ of 2.24 ± 0.71 (A/g). [d]Reported for system with V doping at 7.7 atom %. [e] V doping atom % was not specified in manuscript.

A.2.3 References

1. C.-C. Lin and C. C. L. McCrory, *ACS Catal.*, 2017, **7**, 443-451.
2. J. Suntivich, K. J. May, H. A. Gasteiger, J. B. Goodenough and Y. Shao-Horn, *Science*, 2011, **334**, 1383-1385.
3. F. Song and X. Hu, *Nat Commun*, 2014, **5**, 4477.
4. L. Trotochaud, J. K. Ranney, K. N. Williams and S. W. Boettcher, *J. Am. Chem. Soc.*, 2012, **134**, 17253-17261.
5. R. Wei, X. Bu, W. Gao, R. A. B. Villaos, G. Macam, Z.-Q. Huang, C. Lan, F.-C. Chuang, Y. Qu and J. C. Ho, *ACS Applied Materials & Interfaces*, 2019, **11**, 33012-33021.
6. L. Liardet and X. Hu, *ACS Catal.*, 2018, **8**, 644-650.
7. J. Jiang, F. Sun, S. Zhou, W. Hu, H. Zhang, J. Dong, Z. Jiang, J. Zhao, J. Li, W. Yan and M. Wang, *Nat. Commun.*, 2018, **9**, 2885.
8. T. Gao, Z. Jin, M. Liao, J. Xiao, H. Yuan and D. Xiao, *J. Mater. Chem. A*, 2015, **3**, 17763-17770.
9. M. Yang, X. Fu, M. Shao, Z. Wang, L. Cao, S. Gu, M. Li, H. Cheng, Y. Li, H. Pan and Z. Lu, *ChemElectroChem*, 2019, **6**, 2050-2055.
10. J. Bao, Z. Wang, J. Xie, L. Xu, F. Lei, M. Guan, Y. Zhao, Y. Huang and H. Li, *Chem. Commun.*, 2019, **55**, 3521-3524.
11. Y. Cui, Y. Xue, R. Zhang, J. Zhang, X. a. Li and X. Zhu, *Journal of Materials Chemistry A*, 2019, **7**, 21911-21917.
12. K. Chakrapani, G. Bendt, H. Hajiyani, T. Lunkenbein, M. T. Greiner, L. Masliuk, S. Salamon, J. Landers, R. Schlögl, H. Wende, R. Pentcheva, S. Schulz and M. Behrens, *ACS Catal.*, 2018, **8**, 1259-1267.

A.3 Supporting information for Chapter 4

A.3.1 Supporting Figures

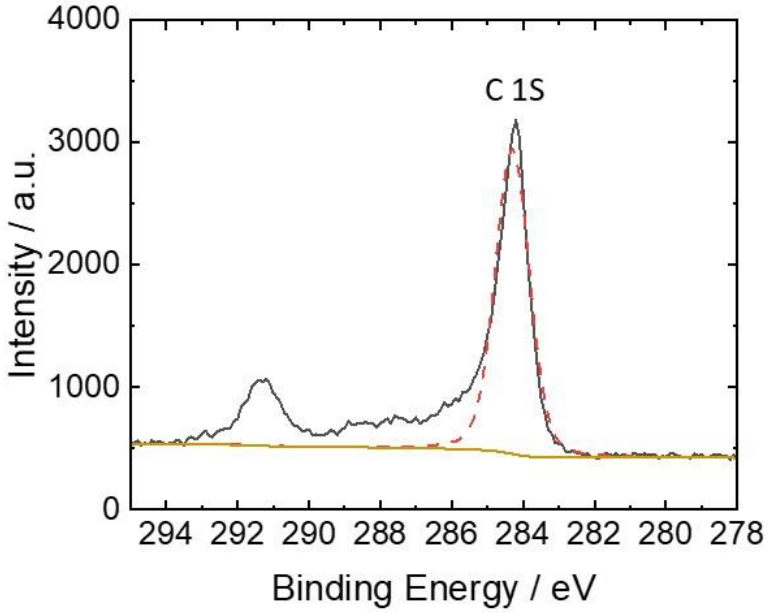

Figure A.25: Carbon XPS spectrum of a representative electrode taken prior to electrochemical measurements.

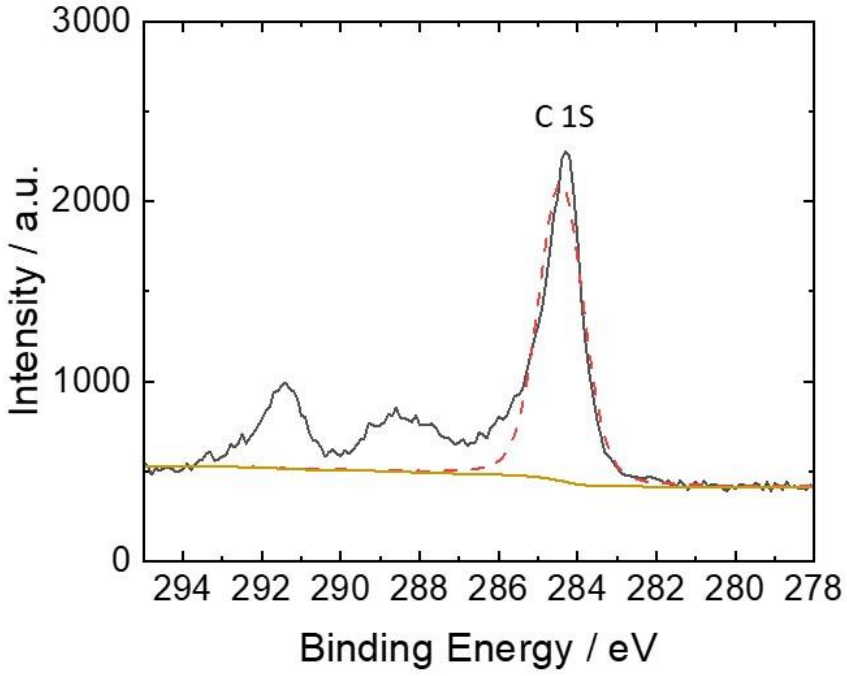

Figure A.26: Carbon XPS spectrum of an electrode after electrolysis at 1.55V vs RHE with n-BuOH added.

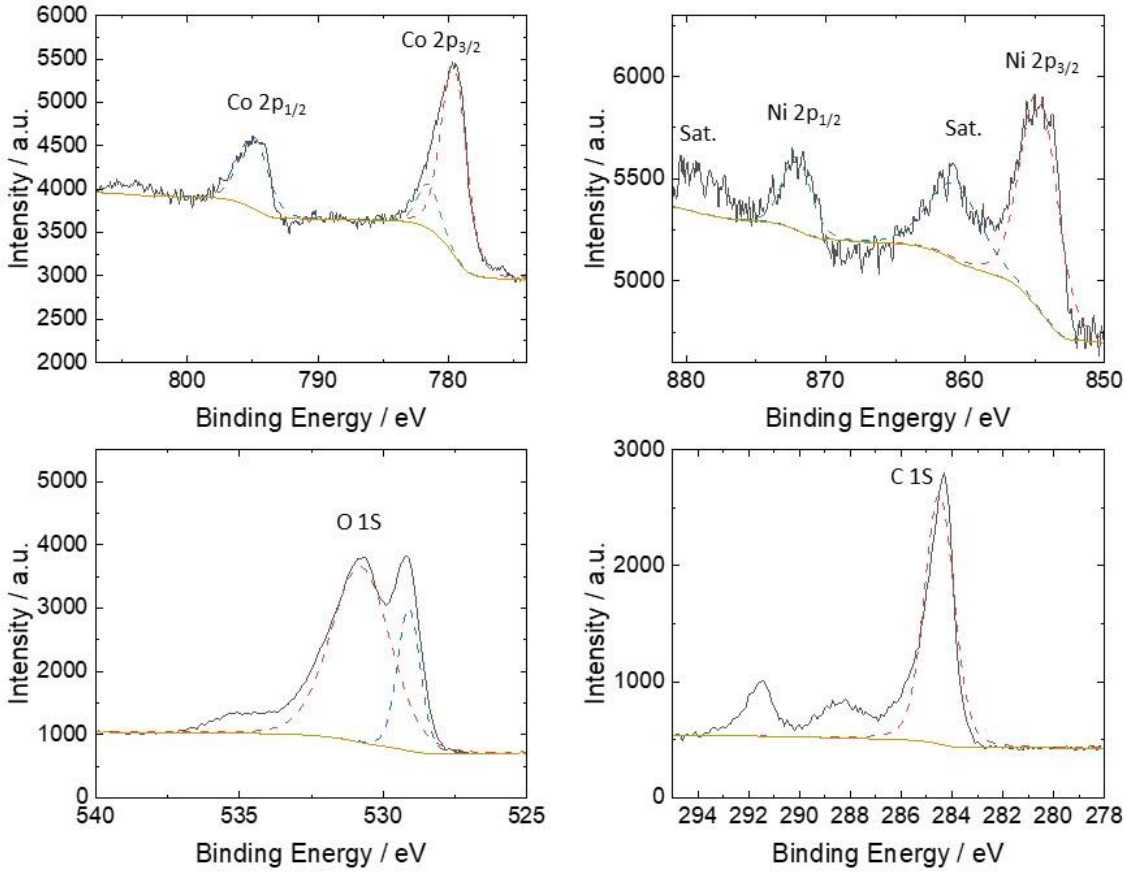

Figure A.27: XPS spectra of cobalt, nickel, oxygen, and carbon for an electrode after electrolysis at 1.65V vs RHE with n-BuOH added to the solution.

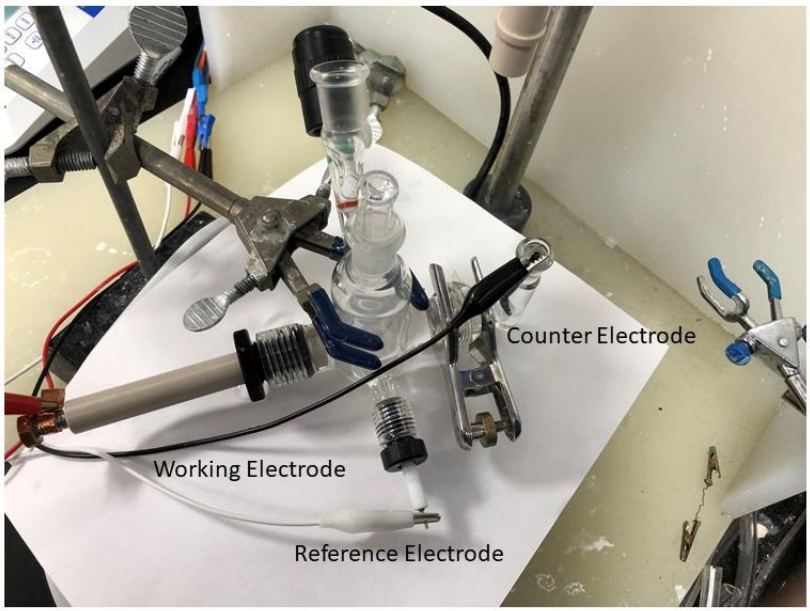

Figure A.28 Image of a typical sealed cell electrolysis cell. Working electrode is a glassy carbon electrode (d = 1.96mm), reference electrode is a Ag/AgCl reference electrode, and the counter electrode is a carbon rod. Membrane Separator is a Nafion™ 117 membrane.

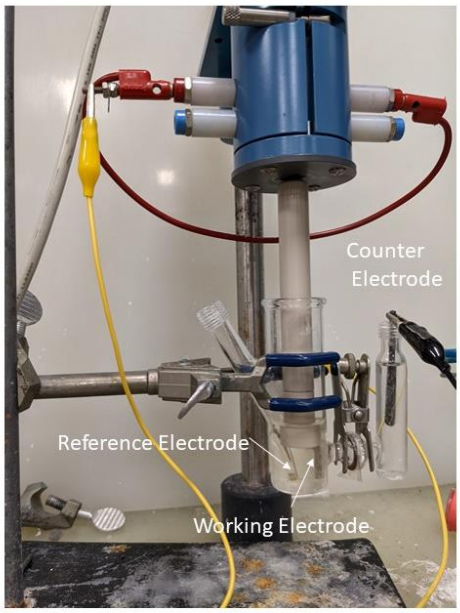

Figure A.29 Image of a typical unsealed cell electrolysis cell. Working electrode is a glassy carbon electrode (d = 1.96mm), reference electrode is a Ag/AgCl reference electrode, and the counter electrode is a carbon rod. Membrane Separator is a Nafion™ 117 membrane.

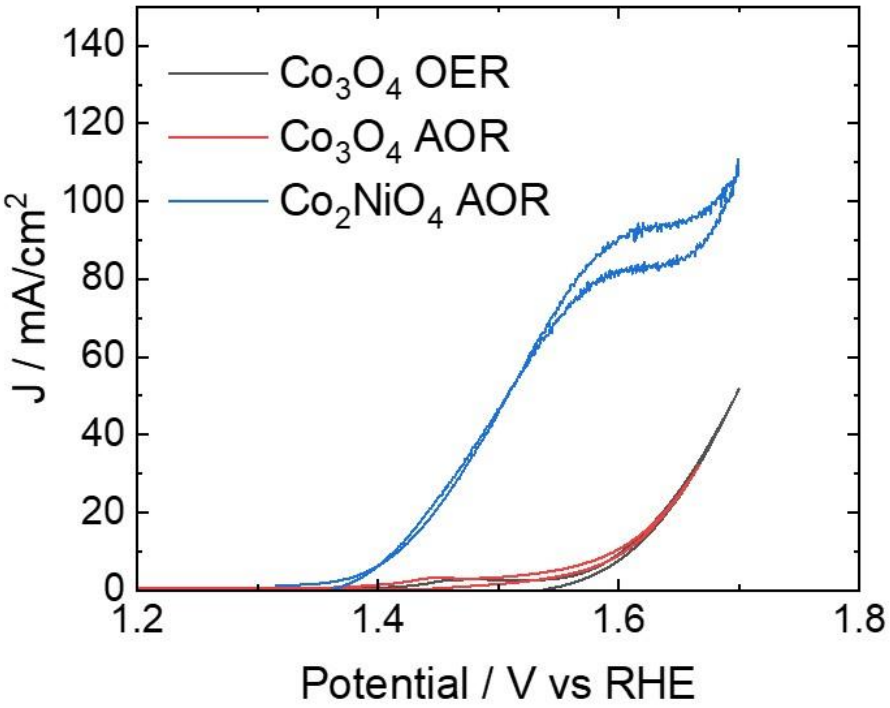

Figure A.30 Representative cyclic voltammograms for Co_3O_4 for oxygen evolution and alcohol oxidation. An AOR trace for Co_2NiO_4 is added as a comparison between the activities of the two different catalysts.

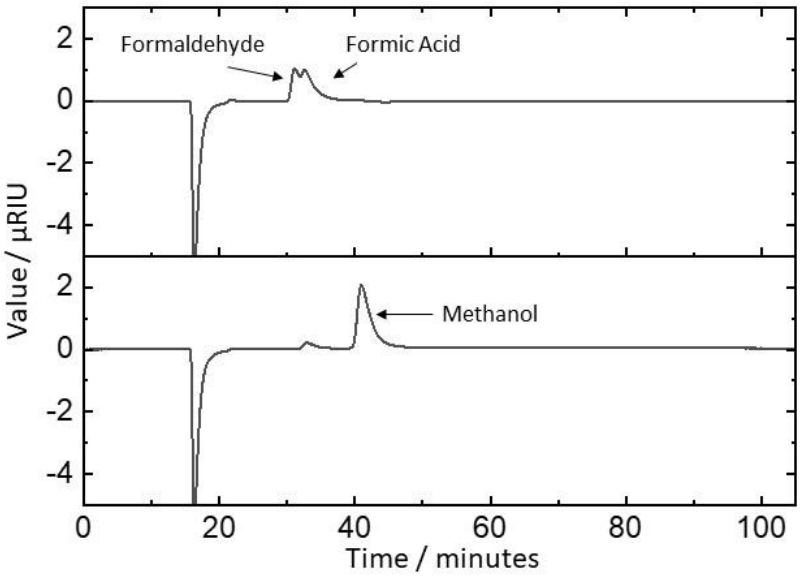

Figure A.31 Example Chromatograms of a calibration standard (upper) and a post electrolysis reaction mixture (lower) for the oxidation of methanol, with both the possibly products labeled in the calibration standard, and the starting alcohol labeled in the electrolysis reaction mixture.

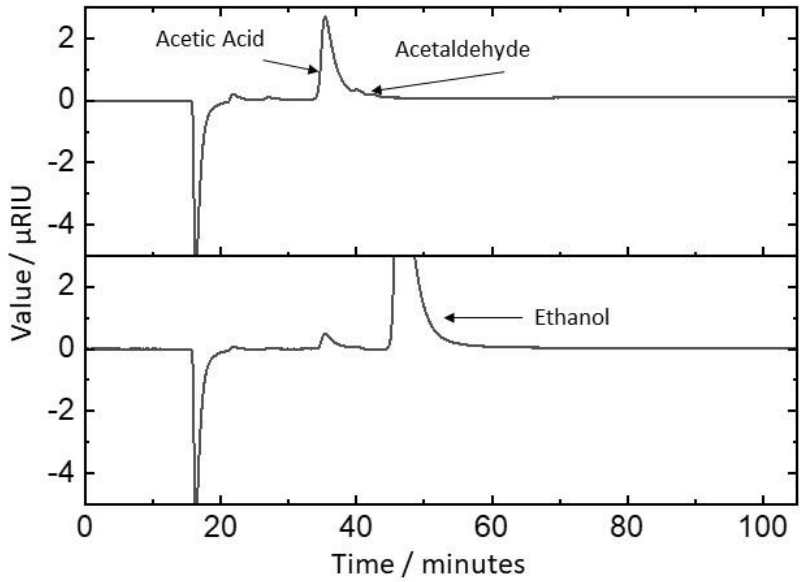

Figure A.32 Example Chromatograms of a calibration standard (upper) and a post electrolysis reaction mixture (lower) for the oxidation of ethanol, with both the possibly products labeled in the calibration standard, and the starting alcohol labeled in the electrolysis reaction mixture.

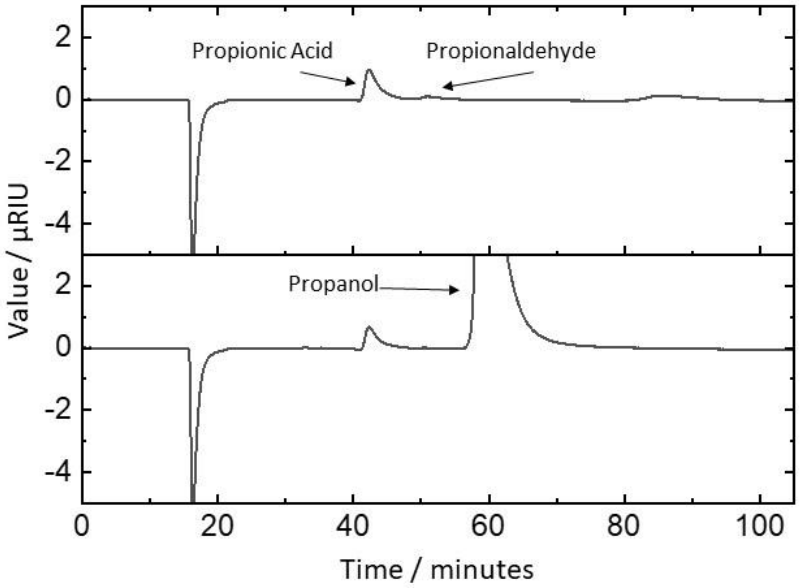

Figure A.33 Example Chromatograms of a calibration standard (upper) and a post electrolysis reaction mixture (lower) for the oxidation of propanol, with both the possibly products labeled in the calibration standard, and the starting alcohol labeled in the electrolysis reaction mixture.

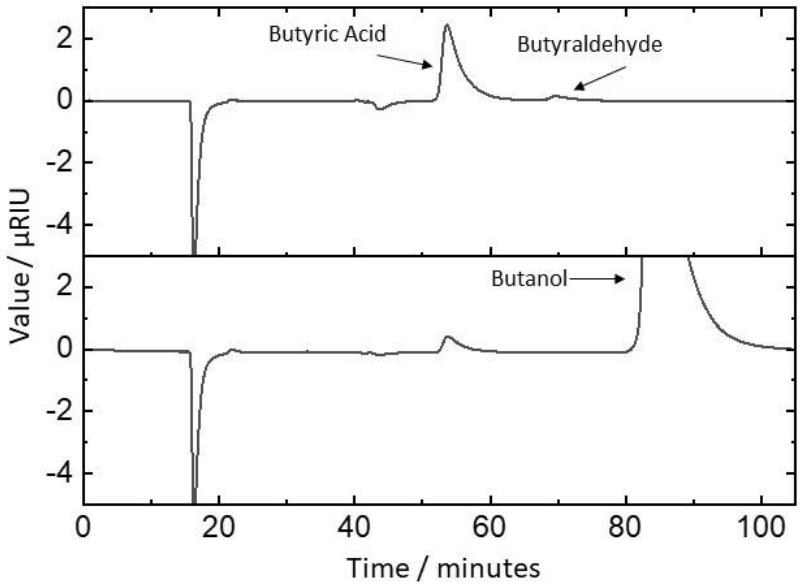

Figure A.34 Example Chromatograms of a calibration standard (upper) and a post electrolysis reaction mixture (lower) for the oxidation of butanol, with both the possibly products labeled in the calibration standard, and the starting alcohol labeled in the electrolysis reaction mixture.

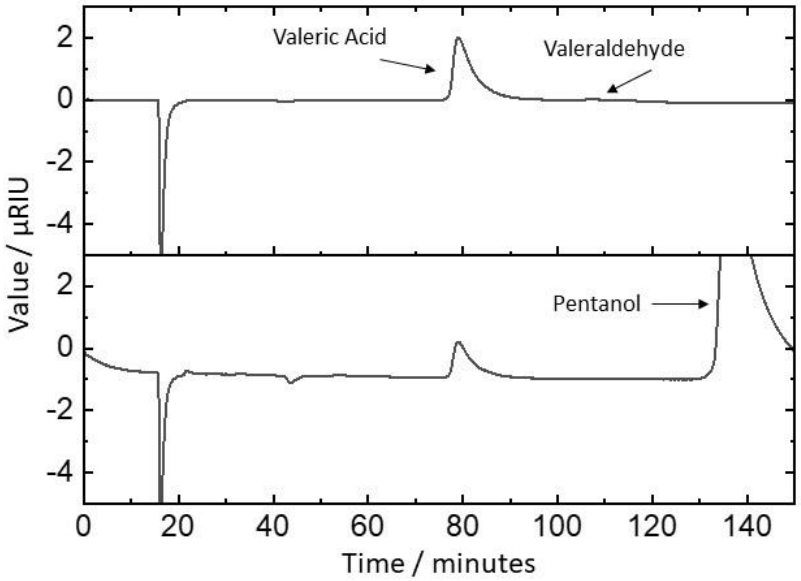

Figure A.35 Example Chromatograms of a calibration standard (upper) and a post electrolysis reaction mixture (lower) for the oxidation of pentanol, with both the possibly products labeled in the calibration standard, and the starting alcohol labeled in the electrolysis reaction mixture

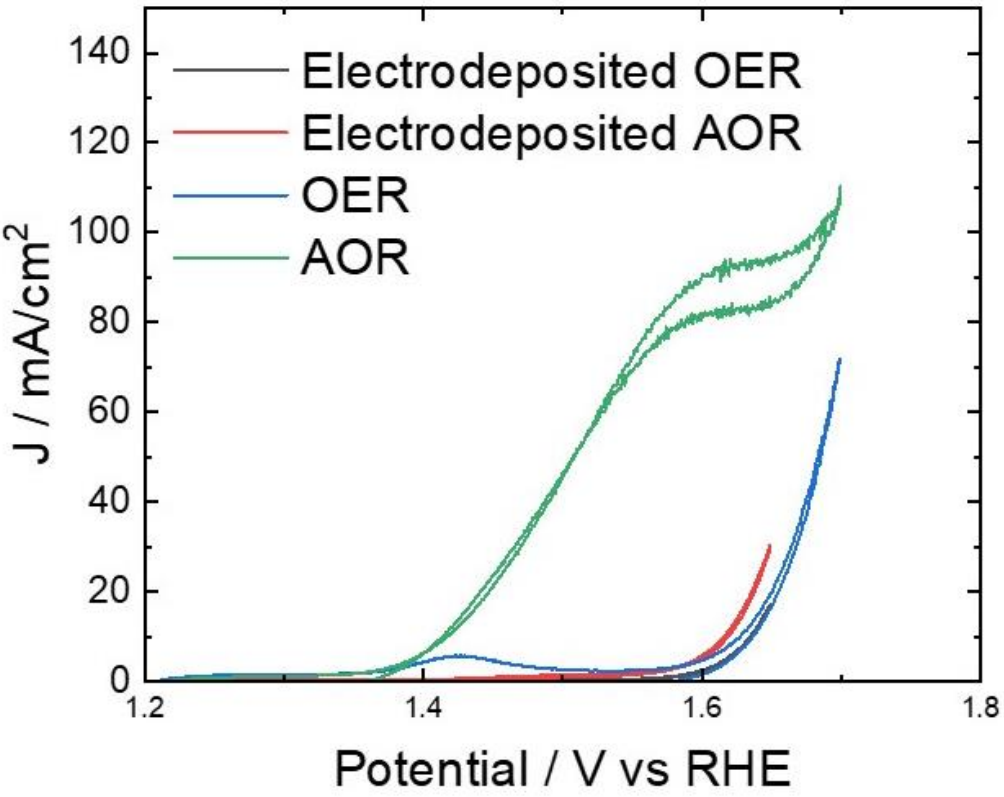

Figure A.36 Cyclic voltammograms of the as synthesized and electrodeposited CoNiOx samples both with and without alcohol added showing no increased activity with alcohol added for the electrodeposited system.

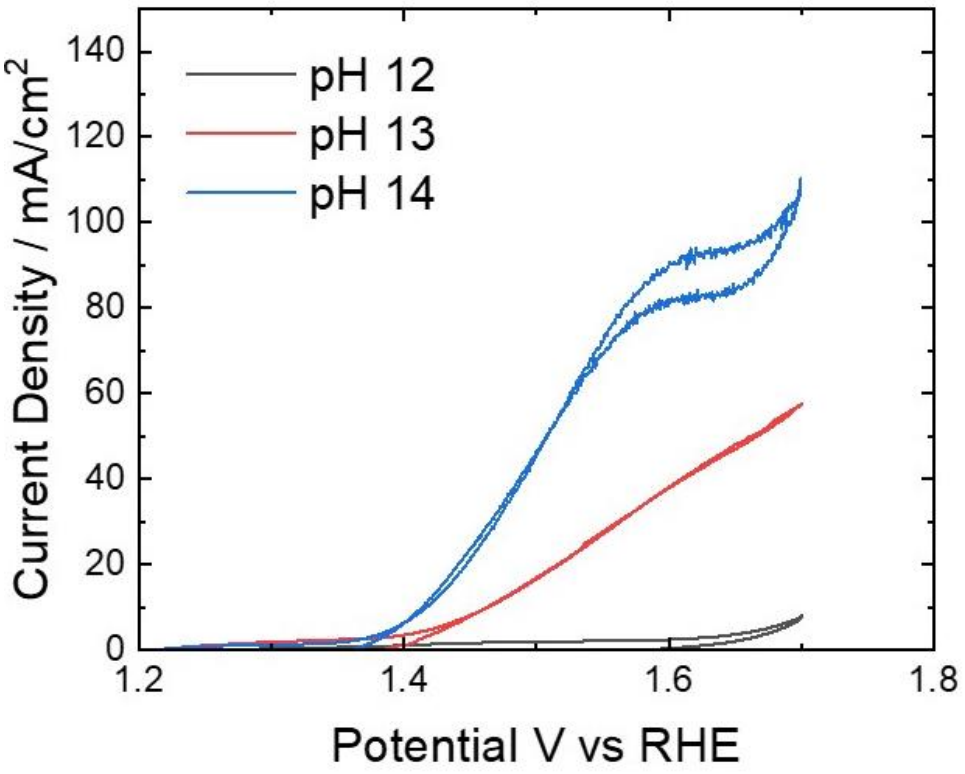

Figure A.37 Cyclic voltammograms using a Co_2NiO_4 catalyst in 1M NaOH (pH 14), 0.1M NaOH (pH 13), and a 0.1M phosphate buffer at pH 12, all with 100mM n-butanol added. X-axis is on the RHE scale, showing a strong correlation between pH and AOR activity as evident by the decrease in activity with decreasing pH.

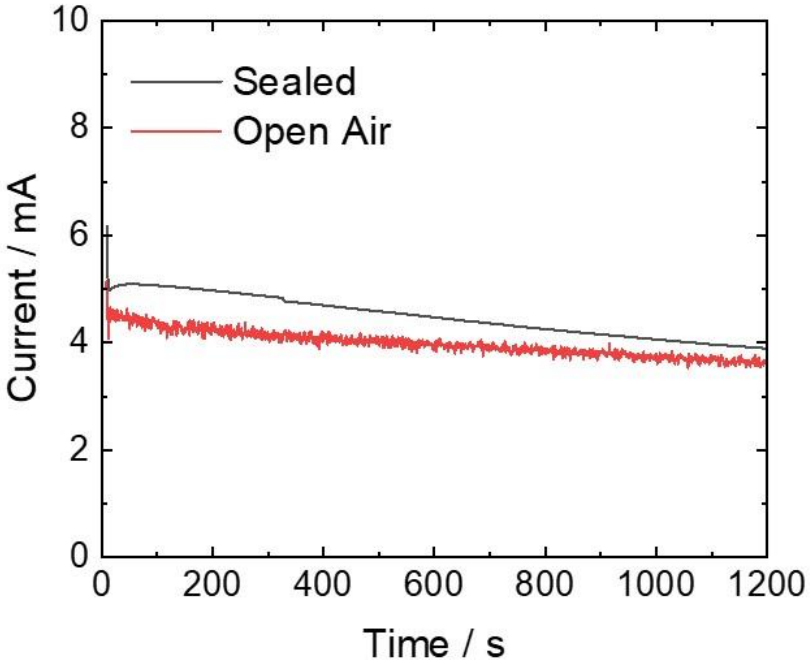

Figure A.38 Representative current traces for methanol oxidation in both sealed and open air electrolysis cells

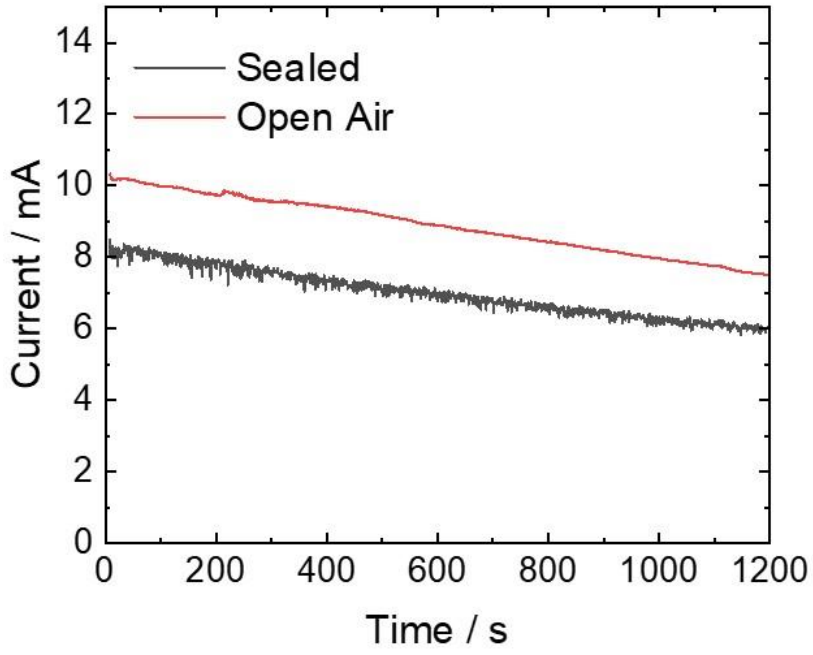

Figure A.39 Representative current traces for ethanol oxidation in both sealed and open air electrolysis cells

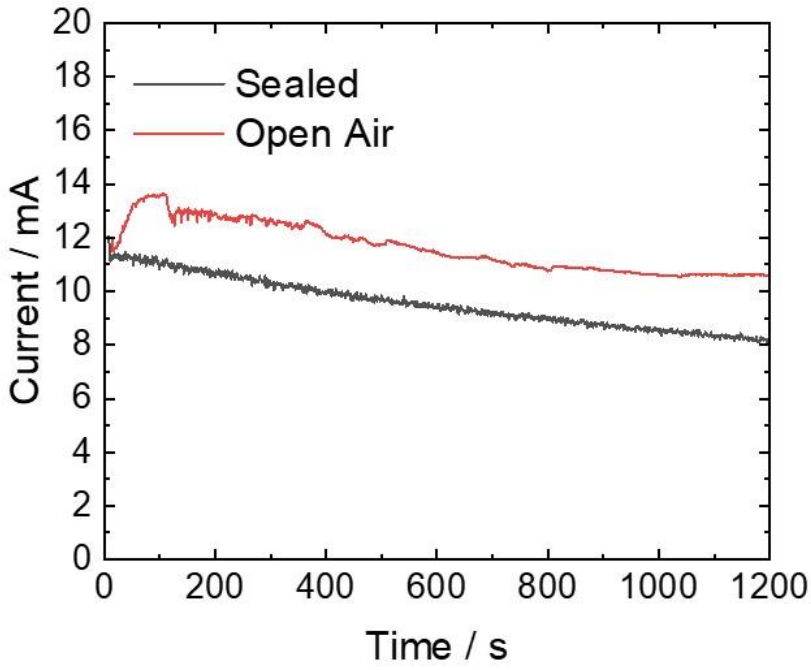

Figure A.40 Representative current traces for propanol oxidation in both sealed and open air electrolysis cells

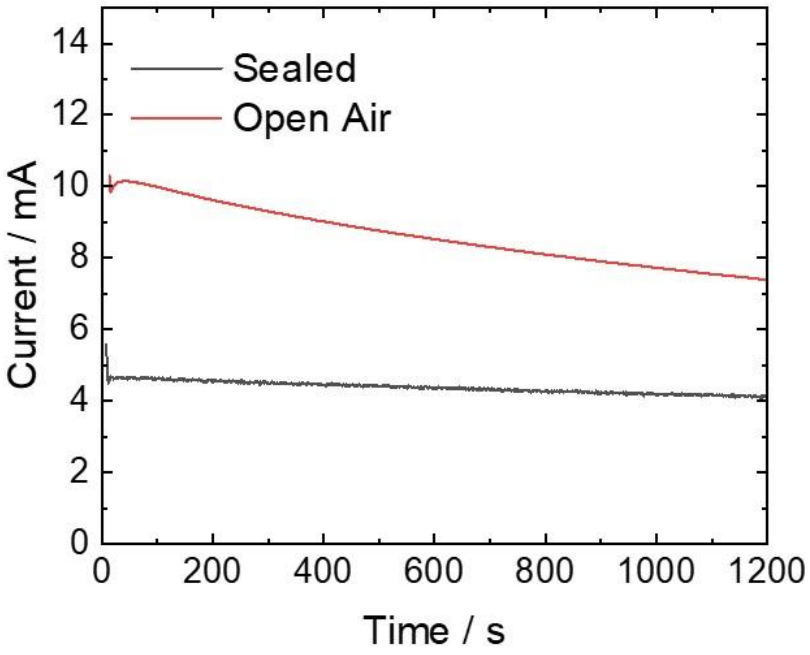

Figure A.41 Representative current traces for butanol oxidation in both sealed and open air electrolysis cells

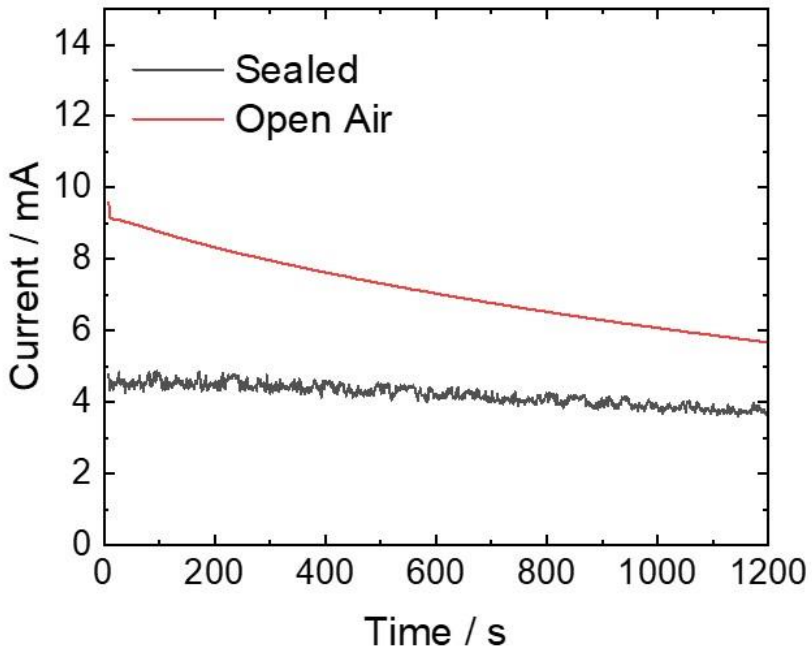

Figure A.42 Representative current traces for pentanol oxidation in both sealed and open air electrolysis cells

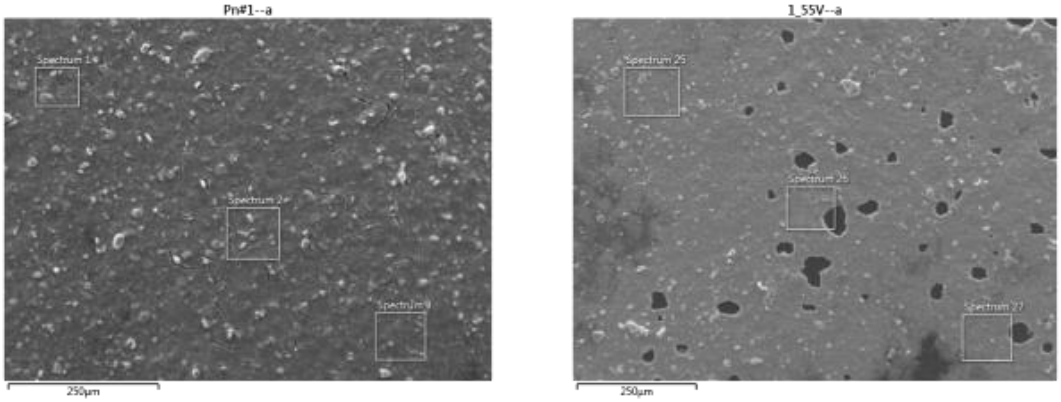

Figure A.43 Representative SEM images of the surface both before (left) and after (right) electrolysis at 1.55V vs RHE. The images show the continued integrity of the catalyst, binder composition for the duration of the electrolysis experiments. Spectrums are EDS spectrums collecting the relative weight percent of atoms. These data are included as SEM Co:Ni ratio in table A.8

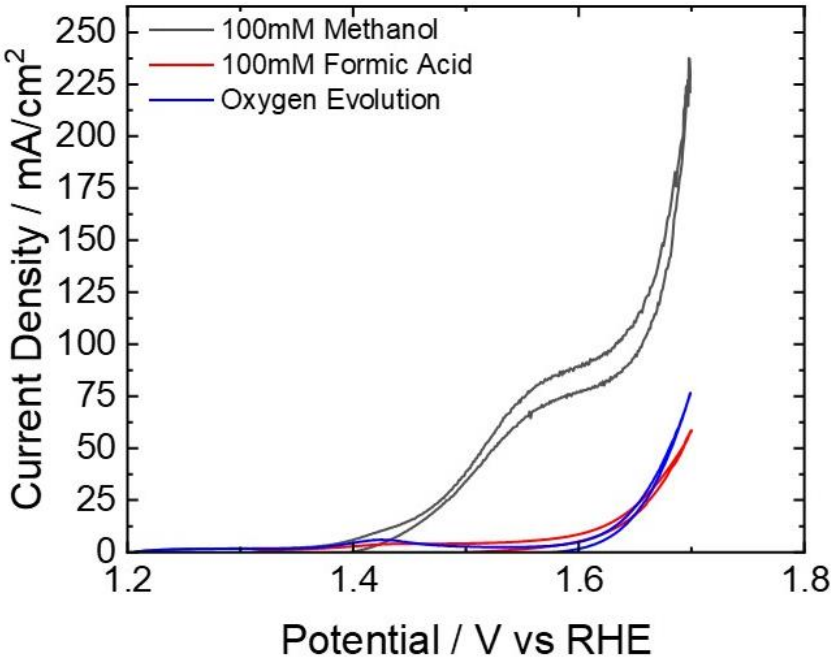

Figure A.44: Cyclic voltammograms for the oxidation of 100mM formic acid in 1M NaOH (red) showing little activity change upon addition to the electrolyte vs oxygen evolution in 1M NaOH (black) and a drastic decrease in the observed current compared to 100mM MeOH in 1M NaOH(black).

A.3.2 Supporting Tables

Table A.8 Synthetic parameters for Co_2NiO_4 Particles used in this manuscript

Catalyst	nominal Co/Ni	Co/M[a]	Co/M[b]	Lattice parameter (Å)[c]	S_{BET} (m^2/g)
Co_2NiO_4	2	2.07	2.07 ± 0.02	8.087[c]	80.93 ± 3.09

[a] Determined from ICP-MS

[b] Determined from SEM-EDX elemental ratios, value is the average of 9 total measurements on 3 independent electrodes

[c] Calculated from PXRD (311) peak

Table A.9 Elemental composition analysis of electrodes taken prior to electrochemical measurements, after a 2hr electrolysis at 1.55v Vs RHE applied voltage, and after a 2hr electrolysis at 1.65V vs RHE. Errors are the standard deviations of three sets of independent measurements.

	ICP-MS	SEM-EDS	XPS
Pre electrolysis	2.07 ± 0.05	2.07 ± 0.02	1.96 ± 0.02
After 1.55V vs RHE	2.18 ± 0.09	2.05± 0.01	1.91 ± 0.07
After 1.65V vs RHE	2.07 ± 0.08	2.07 ± 0.01	1.96 ± 0.13

Table A.10 Experimental results for sealed cell electrolysis experiments

Alcohol	Charge	Acid conc.	Acid Charge	Acid FE	Aldehyde conc.	Aldehyde Charge	Aldehyde FE	AOR Charge	AOR FE
MeOH	21.75 ± 5.76	1.03 ± 0.26	7.94 ± 2	37.1 ± 1.1	0.02 ± 0.01	0.06 ± 0.06	0.17 ± 2.8	8 ± 1.97	36.4 ± 2.9
EtOH	37.77 ± 11.88	2.24 ± 0.73	17.34 ± 6.37	45.9 ± 2.5	7.05 ± 2.55	22.65 ± 6.44	60.0 ± 10.1	39.99 ± 12.27	105.9 ± 12.7
n-PrOH	41.6 ± 7.6	4.04 ± 0.36	31.15 ± 6.21	74.9 ± 4.5	3.32 ± 1.32	10.73 ± 3.91	25.8 ± 8.1	41.88 ± 8.33	100.7 ± 12.5
n-BuOH	31.15 ± 7.85	3.31 ± 1.11	24.69 ± 6.78	79.0 ± 3.3	1.72 ± 0.62	6.89 ± 2.27	22.0 ± 3.0	31.58 ± 8.56	101.0 ± 6.6
Pentanol	22.48 ± 3.38	2.28 ± 0.38	17.59 ± 2.94	78.9 ± 1.9	1.31 ± 0.13	5.05 ± 0.52	22.5 ± 1.6	22.65 ± 3.45	100.7 ± 3.6

Table A.11 Experimental results for unsealed electrolysis experiments

Alcohol	Charge	Acid conc.	Acid Charge	Acid FE	Aldehyde conc.	Aldehyde Charge	Aldehyde FE	AOR Charge	AOR FE
MeOH	15.77 ± 5.97	1.46 ± 0.60	5.64 ± 2.33	35.8 ± 1.4	0.03 ± 0.02	0.04 ± 0.03	0 ± 0	5.67 ± 2.36	35.8 ± 1.4
EtOH	46.71 ± 4.11	5.13 ± 0.52	20.56 ± 2.22	44.0 ± 1.8	2.24 ± 0.45	4.5 ± 0.79	9.6± 2.4	25.06 ± 2.15	53.7 ± 4.1
n-PrOH	55.37 ± 2.89	9.17 ± 0.3	34.7 ± 1.67	62.7 ± 1.6	1.06 ± 0.79	2.15 ± 1.26	3.9 ± 2.3	36.86 ± 1.91	66.6 ± 3.9
n-BuOH	40.99 ± 6.54	7.66 ± 1.2	29.55 ± 4.61	70.4 ± 1.2	7.49 ± 0.97	14.45 ± 1.88	34.7 ± 1.5	43.99 ± 6.47	105.1 ± 2.7
Pentanol	27.18 ± 1.83	5.29 ± 0.12	20.43 ± 0.76	75.2 ± 2.7	3.29 ± 0.57	6.34 ± 1.11	23.3 ± 2.6	26.77 ± 1.86	98.5 ± 5.3

Table A.12 Experimental results for electrolysis of 100 mM n-butanol in 1M NaOH solutions. Potentials are V vs RHE and errors are reported as the standard deviation of three independent electrolysis experiments. Aldehyde concentration was undefined at 1.4V vs RHE as the amount of aldehyde fell blow out limit of quantification (0.5 mM).

Potential	Charge	Acid conc.	Acid Charge	Acid FE	Aldehyde Conc.	Aldehyde Charge	Aldehyde FE	AOR Charge	AOR FE
1.40	1.69 ± 0.38	0.34 ± 0.14	1.32 ± 0.54	75.8 ± 12.9	Und.	Und.	Und.	0.42 ± 0.33	75.8 ± 12.9
1.45	13.47 ± 0.58	2.74 ± 0.08	10.57 ± 0.31	79.0 ± 0.8	1.83 ± 0.05	3.53 ± 0.1	26.5 ± 3.1	14.1 ± 0.41	105.1 ± 3.8
1.50	20.36 ± 5.9	4.16 ± 1.47	16.04 ± 5.66	77.7 ± 5.4	3.04 ± 0.69	5.87 ± 1.33	29.5 ± 5.7	21.91 ± 6.58	107.3 ± 11.1
1.55	40.99 ± 6.54	7.66 ± 1.2	29.55 ± 4.61	70.4 ± 1.2	7.49 ± 0.97	14.45 ± 1.88	34.7 ± 1.5	43.99 ± 6.47	105.1 ± 2.7
1.60	43.9 ± 8.2	6.41 ± 1.24	24.76 ± 4.8	56.3 ± 0.8	5.18 ± 0.59	9.99 ± 1.14	23.0 ± 1.7	34.75 ± 5.91	79.3 ± 2.5
1.65	69.78 ± 2.33	6.16 ± 1.01	23.76 ± 3.88	34.0 ± 4.4	9.6 ± 1.56	18.53 ± 3.02	26.6 ± 5.2	42.3 ± 0.86	60.6 ± 9.6
1.70	112.48 ± 19.48	4.39 ± 0.67	16.96 ± 2.6	15.6± 4.9	11.58 ± 2.24	22.35 ± 4.33	20.6 ± 6.5	39.31 ± 6.27	36.2 ± 11.3

Table A.13 Experimental results for electrolysis of 100 mM n-butanol in 1M NaOH solutions (without chloride) and in 1M NaOH with 1M NaCl added (with chloride). Potential was held at 1.55V vs RHE and errors are reported as the standard deviation of three independent electrolysis experiments.

Sample	Charge	Acid conc.	Acid Charge	Acid FE	Aldehyde Conc.	Aldehyde Charge	Aldehyde FE	AOR Charge	AOR FE
Without Chloride	40.99 ± 6.54	7.66 ± 1.2	29.55 ± 4.61	70.4 ± 1.2	7.49 ± 0.97	14.45 ± 1.88	34.7 ± 1.5	43.99 ± 6.47	105.1 ± 2.7
With Chloride	42.28 ± 5.00	7.78 ± 0.83	30.02 ± 3.20	70.9 ± 7.2	4.78 ± 0.76	9.23± 1.47	21.8± 4.2	39.25 ± 4.68	92.7± 7.3

Table A.14 Comparison to other catalysts in the literature. Where applicable potentials closest to 1.55V vs RHE were used for comparison. Product and selectivity data which was not reported in the manuscripts are reported as n.a.

Catalyst	Substrate	Potential / V vs RHE	Current Density /mA/cm$^2_{geo}$	Major Product	Selectivity / %	Source
Co_2NiO_4	n-butanol	1.55	22.2	Butyric Acid	101	This work
Ni-Co/RGO/CPE	Ethanol	1.8	~24	n.a.	n.a.	[1]
Co_2NiO_4	Ethanol	1.55	26.9	Acetic Acid	106	This Work
$NiCo_2O_4$ - NF	HMF	1.55	~15[a]	FDCA	90	[2]
Co_3O_4	Glycerol	1.524	70	n.a.	n.a.	[3]
Fe/Co200	Benzyl Alcohol	1.42V	10	n.a.	n.a.	
$NiCo_2O_4$	Methanol	1.52	74	n.a.	n.a.	[4]
Co_3O_4	HMF	1.55	6.69[b]	n.a.	n.a.	[5]
$NiCo_2O_4$	HMF	1.51	7.02[b]	FDCA	90	[5]
Co_3O_4 - NF	Benzyl Alcohol	1.50	86	Benzoic Acid	99	[6]
CoOOH	HMF	1.4	29	FDCA	60	[7]
CoOOH – Cu Foam	HMF	1.503	20	FDCA	53	[8]
Co_3O_4/NiO	Methanol	1.376	51	n.a.	n.a.	[9]
Co_2NiO_4	Methanol	1.55V	15.5	Formic Acid[c]	37	This work
EA-AuPd	Methanol	0.834	23 (mass Pd not ever given in manuscript???????????)	n.a.	n.a.	[10]

[a] Reported at 1.45V vs RHE
[b] Estimated from CV measurements reported
[c] Formic Acid FE below 50%, however no other products were detected

A.3.3 Supporting methods

All electrolysis samples were analyzed via HPLC to detect product distributions for alcohol oxidation using a Thermo Scientific Ultimax 3000 HPLC system with a UV detector and a Refractomax, refractive index detector and a HyperREZ^{TM} XP Carbohydrate H^+ 7.7mm x 30cm (8µm particle size) column. The column over was set to 50°C. Flow rate was isocratic at 0.300mL min^{-1} with 0.005M H_2SO_4 (Thermo scientific, Trace Metal Grade) as the elution solvent. 30µL of sample was injected into the HPLC. Calibration standards were prepared with

both the carboxylic acid and aldehyde products in the same sample vial to ensure good separation, and to remove matrix effects. Curves were prepared in the range of 10-0.1mM for each the aldehyde and the acid products. Calibration standards were prepared through serial dilutions of 10mM stock solutions. Three different curves were averaged to create the final calibration curve for each alcohol oxidation system.

Integration was performed in the Chromelion software and areas were recorded for each electrode tested. A linear baseline was used where appropriate. In some analytes, such as formaldehyde and formic acid, there was some overlap with the peaks in the high concentration standards (see Figure A.31). In these analytes, a split peak was used to quantify each component. This split was added for all samples with these analytes included at a constant time point to account for the overlap of areas in the chromatographs. This strategy was used for methanol, and ethanol, however the overlap with methanol oxidation products was considerably more noticeable than ethanol products. Aldehyde peaks in the refractive index detector were lower in intensity than acid products and as such the chromatographs were enlarged to ensure proper integration of the peak. Sample chromatograms are included in figure A.35 for both calibration standards and an example electrolysis.

Specific charge and faradaic efficiencies were calculated using the area of the product peak and the calibration curve to generate a concentration of analyte in the solution. This concentration was then converted to a specific charge through the following equations. The $2e^-$ and $4e^-$ are the number of moles of electrons required for the formation of each product, and 96485 is faradays constant in units of $C * mol_{electron}^{-1}$

$$C_{aldehyde} = \text{molarity} * \text{solution volume} * 2e^- * 96485 \quad \text{A.1}$$

$$C_{acid} = \text{molarity} * \text{solution volume} * 4e^{-} * 96485 \quad \text{A.2}$$

Theis specific charge value was then converted into a faradaic efficiency through the following equation. Where $C_{specific}$ is the charge for a specific product, and $C_{expiremental}$ is the total charge passed during the duration of the electrolysis.

$$FE_{specific} = \frac{C_{specific}}{C_{expiremental}} \quad \text{A.3}$$

A.3.4 References

1. V. Hassanzadeh, M. A. Sheikh-Mohseni and B. Habibi, *Journal of Electroanalytical Chemistry*, 2019, **847**, 113200.
2. L. Gao, Y. Bao, S. Gan, Z. Sun, Z. Song, D. Han, F. Li and L. Niu, *ChemSusChem*, 2018, **11**, 2547-2553.
3. S. Sun, L. Sun, S. Xi, Y. Du, M. U. Anu Prathap, Z. Wang, Q. Zhang, A. Fisher and Z. J. Xu, *Electrochimica Acta*, 2017, **228**, 183-194.
4. R. Ding, L. Qi, M. Jia and H. Wang, *Catalysis Science & Technology*, 2013, **3**, 3207-3215.
5. M. J. Kang, H. Park, J. Jegal, S. Y. Hwang, Y. S. Kang and H. G. Cha, *Applied Catalysis B: Environmental*, 2019, **242**, 85-91.
6. Y. Cao, D. Zhang, X. Kong, F. Zhang and X. Lei, *Journal of Materials Science*, 2021, **56**, 6689-6703.
7. X. Deng, G.-Y. Xu, Y.-J. Zhang, L. Wang, J. Zhang, J.-F. Li, X.-Z. Fu and J.-L. Luo, *Angewandte Chemie International Edition*, 2021, **n/a**.
8. R. Zhang, S. Jiang, Y. Rao, S. Chen, Q. Yue and Y. Kang, *Green Chemistry*, 2021, **23**, 2525-2530.
9. J. B. Wu, Z. G. Li, X. H. Huang and Y. Lin, *Journal of Power Sources*, 2013, **224**, 1-5.
10. A. Kardan, N. Ashraf, Z. Dabirifar and S. Khadempir, *RSC Advances*, 2021, **11**, 10615-10624.